# Spin-Orbit Coupling Effects From Graphene To Graphite


**Dissertation**

zur Erlangung des Doktorgrades

der Naturwissenschaften (Dr. rer. nat.)

der Fakultät für Physik

der Universität Regensburg

vorgelegt von

**Sergej Konschuh**

2011

Die Arbeit wurde von Prof. Dr. Jaroslav Fabian angeleitet.
Das Promotionsgesuch wurde am 6. 7. 2011 eingereicht.
Das Promotionskolloquium fand am 26. 9. 2011 statt.

Prüfungsausschuss:

| | |
|---|---|
| Vorsitzender: | Prof. Dr. S. Ganichev |
| 1. Gutachter: | Prof. Dr. J. Fabian |
| 2. Gutachter: | Prof. Dr. M. Grifoni |
| Weiterer Prüfer: | Prof. Dr. T. Wettig |

# Contents

# List of Tables

# List of Figures

# 1 Introduction

Graphene is a two-dimensional allotrope of carbon [8] that has attracted enormous interest due to both its truly two-dimensional nature as well as its unique electronic properties originating in a linear energy dispersion at the Fermi level. The spectrum at the K points is akin to the Dirac cones of massless relativistic particles, causing excitement about the opportunities to test relativistic quantum mechanics in a solid state material. This ideal picture changes qualitatively when spin-orbit coupling is taken into account. Namely, the coupling introduces a gap in the spectrum, giving a mass to the particles, and the spectrum is no longer linear. The emergence of the gap moves graphene from the family of semimetals to the one of quantum Spin Hall insulators [9]. It is ironic that the relativistic (spin-orbit) effects destroy the relativistic nature of the graphene spectrum.

While spin-orbit coupling in graphene is relatively small compared to the usual semiconductors, it is nevertheless important for the understanding of many physical phenomena. These include spin relaxation of electrons, the electronic $g$-factor, the magnetocrystalline and otherwise magnetic transport anisotropies, spin transport, or the quantum Spin Hall effects in graphene ribbons.

The absence of hyperfine coupling and small intra-atomic spin-orbit coupling in carbon atoms should provide long spin relaxation times in graphene and also in graphene related structures: stacks of several graphene layers. This makes single layer graphene and the so called few layer graphenes promising candidates for spin-based devices, where the coupling of spin and orbital degrees of freedom plays a major role in investigations of the building blocks of spintronics such as spin injection [10, 11], spin transport [12, 13, 14, 15, 16, 17], and spin relaxation [18, 19, 20]. However, the first spin injection measurements based on a nonlocal spin valve geometry [18] revealed surprisingly short spin relaxation times of about 100 - 200 ps, being only weakly dependent on the charge density and temperature. This contradiction raises questions about the role of the intra-atomic spin-orbit interaction in the electronic properties of single and few layer graphenes. In this context one faces the questions: How does spin-orbit interaction change the band structures of single and few layer graphenes, and how big are these effects? A further question is how the raising spin-orbit coupling effects change under the influence of an applied electric field, which exists in the experimental environment: In experimental realizations graphene is gated and/or is placed on a substrate which usually includes charged impuri-

ties. Free-standing ideal graphene has a center of inversion symmetry, making its states doubly (spin) degenerate at a given momentum, even in the presence of spin-orbit coupling. Graphene on a substrate, or under a gate bias voltage, loses this property and the bands are further split. This splitting is akin to the one encountered in semiconductor physics under the name of Bychkov-Rashba splitting or structure inversion asymmetry induced splitting [21, 22]. Only Kramers degeneracy is left, meaning that the energies of the states of opposite spins and momenta are equal. In this work we define the Therefore spin-orbit coupling effect which is due to the intra-atomic spin-orbit interaction and the extrinsic spin-orbit coupling effect, Bychov-Rashba spin-orbit coupling, which arises due to an external electric field normal to the graphene layer.

The question about the size of the spin-orbit induced Therefore band gap in single layer graphene at the $K$ points has been given conflicting answers. The earliest estimates of 200 $\mu$eV [9] were replaced by tight-binding studies and supporting first-principles results [23, 24], predicting the gap as small as 1 $\mu$eV. These tight-binding studies considered $s$ and $p$ orbitals only. An all-electron first-principles calculations gave a much higher value of 50 $\mu$eV [25], posing an interesting puzzle of what is the actual physics behind the gap. It has recently been proved, again from first-principles calculations, that the gap originates from the spin-orbit coupling of (nominally unoccupied) $d$ and higher orbitals [26]. The predicted gap in that calculation is 24 $\mu$eV. A reasonable estimate, considering the idiosyncrasies of the *ab initio* codes, is a value of the gap in the range between 25 and 50 $\mu$eV.

The fact that one has to consider $d$ and higher orbitals to get a sizable spin-orbit gap in graphene turns out to have already been known to Slonczewski [27, 28], who devised a group theoretical argument showing in effect that the spin-orbit coupling of the $p$ orbitals contributes in the second order, while that of the $d$ orbitals in the first order. Illustrative symmetry arguments can be found in Ref. [29]. The main point is that without spin-orbit coupling the $p_z$ orbitals, which form the relevant states at $K$ and the Fermi energy, do not hybridize with $p_x$ and $p_y$. Their hybridization is solely via the spin-orbit interaction. On the other hand, $p_z$ orbitals together with $d_{xz}$ and $d_{yz}$ orbitals and other anti-symmetric orbitals of higher angular momentum[1] form the $\pi$ band. This statement has also been proven by first-principles work [26]. Since the $d_{xz}$ and $d_{yz}$ orbitals are affected by spin-orbit coupling, forming the spin-split "rotating" orbitals $d_{xz} \pm i d_{yz}$, the gap of the $\pi$ bands is linearly proportional to the strength of this intra-atomic $d$-orbital splitting.

The origin of the extrinsic splitting of the graphene bands in the picture of atomic orbitals is the Stark effect, allowing for hybridization of $p_z$ and $s$ orbitals,

[1] The $f$ and higher orbitals are not considered in this Thesis due to their negligible contributions.

combined with the intra atomic splitting of the $p$ orbital due to spin-orbit coupling. The corresponding tight-binding theory has already been developed by H. Min *et al.* [23]. The $d$ orbitals give negligible contribution (of the order of 1%), as calculated by first-principles method [26] or from our tight-binding theory presented in this Thesis. The extrinsic gap is about 10 $\mu$eV for an electric field of 1 V/nm. This energy scales linearly with the field. A significant enhancement of the extrinsic spin splitting has been reported for graphene placed on a substrate [30, 31, 32, 33]. Giant values of the splitting (anything more than 1 meV should be considered as giant here) are likely to be due to charge transfer between substrate and graphene. If an impurity or an ad-atom is placed on graphene, the $sp^3$ hybridization may distort graphene locally and induce splittings comparable to the values found in zinc-blende semiconductors [34].

In this Thesis we explain the relatively large splitting in intrinsic graphene by using tight-binding method. We include the relevant $s$, $p$, and $d$ orbitals and obtain the orbital couplings necessary to account for the splitting by fitting the tight-binding model to first-principles calculations. Our formula for the intrinsic splitting shows that while the contribution from the spin-orbit coupling of the $p$ orbitals increases with increasing lattice constant (decreasing hopping energy), the contribution from the $d$ orbitals decreases. This predicted trend is well confirmed by first-principles calculations. By increasing artificially the lattice constant increases the splitting decreases first, demonstrating the dominance of the $d$ orbitals. After reaching a minimum the splitting increases, being dominated by the spin-orbit coupling of the $p$ orbitals. We also present explicit formulas for the extrinsic splitting, showing here that the contributions from the $d$ orbitals are negligible.

For many purposes, such as investigating spin-polarized transport, magnetoelectric effects, or disorder effects, it is useful to have a simple single-orbital hopping scheme. The functional form of such a hopping Hamiltonian is given by the system symmetries for the specific band region [9]. We derive such an effective model here by folding down our multi-orbital tight-binding scheme to the $\pi$ level, revealing the most relevant hopping paths (which comprise virtual hoppings to other orbitals) and justifying the hopping Hamiltonian from the conventional tight-binding perspective. The resulting spin-dependent next-nearest-neighbor hopping model reproduces well the spin-resolved spectrum of graphene.

We have found that the physical mechanism for intrinsic spin-orbit coupling in bilayer graphene and other few-layer graphenes is alike in single graphene sheet and in addition manifesting in the band splitting of the same order. Consequently, our findings do not support the descriptions of the spin-orbit coupling effects based on the effective spin-dependent inter-layer hopping through $s$ and $p$ orbitals [35, 36, 37].

The symmetry of the few-layer graphenes structures is reflected in the inter-

layer hopping, which consequently influences the shape of the $\pi$ bands around the K points. The neighboring inter-layer hopping repels corresponding $\pi$ bands away the Fermi-energy leading to so-called high-energy bands. The low-energy bands at the Fermi energy involve intrinsic spin-orbit coupling splitting as in graphene that are of the same order of $24\,\mu$eV. The splitting is significantly suppressed if the $d$ orbitals are excluded from the calculations. This coincidence with the spin-orbit coupling induced band gap in the single-layer graphene implies that the spin-orbit coupling effects in few-layer graphenes and graphite have the same physical origin.

The extrinsic spin-orbit effects lead to a spin-splitting of the $\pi$ bands in the vicinity of the K points due to transitions between spin-up and spin-down states. These additional effects appear due to the breaking of spacial inversion symmetry, for instance when applying an external electric field transverse to the layers. As an intra-layer effect, the Bychkov-Rashba spin-orbit coupling is also present in bilayer and trilayer graphene. Due to its $k$ dependence, it has a minor influence on the electronic structure in the very vicinity of the K point, since it becomes insubstantial in comparison to the effect due to inter-layer hopping and the electrostatic potential arising between the layers. At larger distances from the K points and large electric fields ($> 5$ V/nm) Bychkov-Rashba spin-orbit coupling dominates spin-splitting of the bands. Besides the intra-layer extrinsic spin-orbit coupling effects there are inter-layer effects which have to be considered to reproduce the exact shape of spin splitting of the bands as a function of the wave vector. Thereby we point out, that the dominant part of the splitting arises from the discussed intra-layer effects. Such inter-layer spin-orbit coupling effects are of paramount importance for splittings of high-energy bands, which energies lie beyond the interest of experiments and spintronic applications.

The goal of the Thesis is to present and analyze tight-binding models for single, bilayer, trilayer ABA and ABC graphene, and graphite, that explain quantitatively the results of first principles calculations, obtained independently by Dr. Martin Gmitra. Our tight-binding models take $s$, $p$ and usually ignored $d$ orbitals into account. The tight-binding parameters are obtained by fitting the relevant band structure to the model. The electronic properties are obtained by means of the linearized augmented plane wave technique with generalized gradient approximation [38].

This Thesis is organized as follows: In the first chapter we introduce the multi-orbital tight-binding Hamiltonian and include the effects of the spin-orbit interaction by tight-binding concepts. In the second chapter we derive the effective Hamiltonian, which describes the spin-orbit coupling effects of the Dirac cones. In the third and last chapters we apply the derived single-layer spin-orbit coupling effective Hamiltonian to multi-layer structures: bilayer, ABA and ABC trilayer graphenes, and graphite, and show that the single-layer spin-orbit coupling effects determine the spin-orbit coupling effect in few layer graphenes and

graphite.

# 2 Tight binding description of graphene

Since the experimental realization of graphene, a single stable two-dimensional monolayer of carbon atoms arranged in a honeycomb lattice, considerable research has been done to enlighten its peculiar electronic transport properties originating from the Dirac-like band structure in the vicinity the K and K' points the corners of the first Brillouin zone (BZ) in the momentum space. The cone-like energy dispersion of the electron and the hole bands touching each other at the K points is well reproduced by the tight binding approximation. The point-like Fermi surface makes idealistic non-gated and non-doped graphene gapless semiconductor. Carbon atoms have the four valence electrons. The graphene crystal is hold together by the covalent chemical bonding of the valence electrons, that localizes the electrons to the atomic positions. Due to the localization the electrons are considered as tight-bonded to the atoms. In this chapter we will present the tight-binding (TB) description of the graphene band structure including spin-orbit coupling effects. The TB model describes the band structures by only a few parameters, whose values must be chosen to reproduce the experimental results or outcome of the first-principles (FP) calculations. In contrast to FP, the TB model bears simple effective Hamiltonians, which are used to calculate the relevant of physical properties of the graphene system.

## 2.1 Introduction to the tight binding approximation

The goal of this section is introduce the basic concepts of the tight-binding approximation (TBA) and the terminology and definitions used in this work.

The electrons that localize to the atomic positions have a vanishing probability to be found at the positions of other atoms. Therefore it is reasonable to construct the Bloch wave function of the crystal by a linear combination of the local Wannier functions $\Phi(\vec{r}-\vec{R})$,

$$\Psi_{\vec{k}}(\vec{r}) = \frac{1}{\sqrt{N}} \sum_{\vec{R}} \mathrm{e}^{\mathrm{i}\vec{k}\vec{R}}\ \Phi(\vec{r}-\vec{R}). \tag{2.1}$$

The Wannier functions are centered at the lattice vector $\vec{R}$. $N$ is the number of unit cells in the crystal. To develop a useful model several approximation must be made. The first approximation is the so-called two-center approximation, in which the Hamiltonian is approximated by the atomic Hamiltonian centered on the atomic positions in the unit cell $\vec{R}$. The Wannier functions are approximated by the eigenfunctions of the atomic Hamiltonian, the atomic orbitals $\phi_{\mu,s}(\vec{r} - \vec{t}_l - \vec{R})$, where $\vec{t}_l$ is the position vector of the atom $l$ inside the primitive unit cell at $\vec{R}$ and $s$ is the spin state of the $\mu$th orbital. The resulting on-site orbital- and spin-resolved (Bloch) wave functions

$$\Psi_{\vec{k}l\mu s}(\vec{r}) = \frac{1}{\sqrt{N}} \sum_{\vec{R}} \mathrm{e}^{\mathrm{i}\vec{k}\vec{R}} \ \phi_{\mu,s}(\vec{r} - \vec{t}_l - \vec{R}) \tag{2.2}$$

have to obey the Bloch theorem due to the translation symmetry of the the periodic structure of the crystal. The Bloch theorem can be verified by shifting the wave function by the translation vector $\vec{R}'$,

$$\begin{aligned} \Psi_{\vec{k},j}(\vec{r} + \vec{R}') &= \frac{1}{\sqrt{N}} \sum_{\vec{R}} \mathrm{e}^{\mathrm{i}\vec{k}\vec{R}'} \mathrm{e}^{\mathrm{i}\vec{k}(\vec{R}-\vec{R}')} \ \phi_j(\vec{r} - (\vec{R} - \vec{R}')) \\ &= e^{\mathrm{i}\vec{k}\vec{R}'} \frac{1}{\sqrt{N}} \sum_{\vec{R}''} \mathrm{e}^{\mathrm{i}\vec{k}\vec{R}''} \ \phi_j(\vec{r} - \vec{R}'') \ = \ \mathrm{e}^{\mathrm{i}\vec{k}\vec{R}'} \Psi_{\vec{k},j}(\vec{r}) \end{aligned} \tag{2.3}$$

where $\vec{R}'' = \vec{R}' - \vec{R}$ is another translation vector and the common index $j = l\mu s$ simplifies the notation. The corresponding atomic orbitals $\phi_j(\vec{r}) = \phi_{\mu,s}(\vec{r} - \vec{t}_l)$ can be further distinguished by the angular momentum $\ell$ and the magnetic quantum number $m$ or by the angular momentum and the spatial symmetry with respect to a chosen set of Cartesian axes. In the following sections both notations will be discussed. The derivation of the Hamilton matrix and the corresponding secular equation is based on the variational principle starting with the Schrödinger equation,

$$\hat{H}\Psi_{\vec{k}}(\vec{r}) = \varepsilon_{\vec{k}}\Psi_{\vec{k}}(\vec{r}). \tag{2.4}$$

The crystal wave function $\Psi_{\vec{k}}(\vec{r})$ can be expanded in the basis of the on-site (Bloch) wave functions,

$$\Psi_{\vec{k}}(\vec{r}) = \sum_j c_{\vec{k},j}\Psi_{\vec{k},j}(\vec{r}), \tag{2.5}$$

The coefficients $c_{\vec{k},j}$ can be determined by acting with the complex conjugated on-site wave function from the left, where due to the orthogonality relation of the Bloch functions there is the same wave-vector $\vec{k}$,

$$\sum_{i,j} c^*_{\vec{k}i} c_{\vec{k}j} \left[ \int d\vec{r} \Psi^*_{\vec{k},j}(\vec{r}) \hat{H} \Psi_{\vec{k},i}(\vec{r}) - \varepsilon_{\vec{k}} \int d\vec{r} \Psi^*_{\vec{k},j}(\vec{r}) \hat{H} \Psi_{\vec{k},i}(\vec{r}) \right] = 0. \tag{2.6}$$

With the definition of the on-site wave functions Eq. (2.2) the two-center Hamilton and the overlap matrix elements are defined by the transfer integrals

$$H_{i,j}(\vec{k}) = \frac{1}{N}\sum_{\vec{R},\vec{R}'} e^{\mathrm{i}\vec{k}(\vec{R}-\vec{R}')} \int d\vec{r}\phi_i^*(\vec{r}-\vec{R}')\hat{H}(\vec{r}-\vec{R})\phi_j(\vec{r}-\vec{R}), \tag{2.7}$$

and

$$S_{i,j}(\vec{k}) = \frac{1}{N}\sum_{\vec{R},\vec{R}'} e^{\mathrm{i}\vec{k}(\vec{R}-\vec{R}')} \int d\vec{r}\phi_i^*(\vec{r}-\vec{R}')\phi_j(\vec{r}-\vec{R}), \tag{2.8}$$

respectively. The evaluation of the integrals in Eqs. (2.7) and (2.8) requires the knowledge of the atomic functions $\phi_i(\vec{r}-\vec{R}) := \phi_{\mu,s}(\vec{r}-\vec{t}_l-\vec{R})$. It is more convenient to handle the integration results as parameters, which have to be fitted to reproduce the certain properties of the solid or the band structure obtained by different approaches (FP calculations). These matrix elements in Eqs. (2.7) and (2.8) where $\vec{R}=\vec{R}'$ are called on-site, otherwise for $\vec{R}\neq\vec{R}'$ the transfer integrals result in hopping and overlap parameters, respectively. The orthogonality relations and the symmetries of the atomic orbitals reduces the number of non-zero matrix elements. In general, the atomic orbitals centered at the different sites are not orthogonal and the corresponding overlap parameters have small but finite values. Such non-orthogonal basis is usually needed to reproduce the electronic spectrum over a wide range of wave-vector space.

In the case of non-zero overlap parameters the energy spectrum for a fixed wave vector $\vec{k}$ is given by

$$\varepsilon_{\vec{k}} = \frac{\sum_{i,j} H_{i,j}(\vec{k})c^*_{\vec{k},i}c_{\vec{k},j}}{\sum_{i,j} S_{i,j}(\vec{k})c^*_{\vec{k},i}c_{\vec{k},j}}. \tag{2.9}$$

The secular equation results from minimizing the energy $\varepsilon_{\vec{k}}$, where the coefficients $c^*_{\vec{k},i}$ are chosen such that

$$\frac{\partial\varepsilon_{\vec{k}}}{\partial c^*_{\vec{k},i}} = \frac{\sum_j H_{i,j}(\vec{k})c_{\vec{k},j}}{\sum_{i,j} S_{i,j}(\vec{k})c^*_{\vec{k},i}c_{\vec{k},j}} - \frac{\sum_{i,j} H_{i,j}(\vec{k})c^*_{\vec{k},i}c_{\vec{k},j}}{\left(\sum_{i,j} S_{i,j}(\vec{k})c^*_{\vec{k},i}c_{\vec{k},j}\right)^2}\sum_j S_{i,j}(\vec{k})c_{\vec{k},j} = 0. \tag{2.10}$$

We multiply both sides by $\sum_{i,j} S_{i,j}(\vec{k})c^*_{\vec{k},i}c_{\vec{k},j}$,

$$\frac{\partial\varepsilon_{\vec{k}}}{\partial c^*_{\vec{k},i}} = \sum_j H_{i,j}(\vec{k})c_{\vec{k},j} - \frac{\sum_{i,j} H_{i,j}(\vec{k})c^*_{\vec{k},i}c_{\vec{k},j}}{\sum_j S_{i,j}(\vec{k})c_{\vec{k},j}}\sum_j S_{i,j}(\vec{k})c_{\vec{k},j} = 0\,, \tag{2.11}$$

substitute the expression for the energy spectrum of Eq. (2.9) into the second term, and obtain directly the secular equation,

$$\sum_j \left[ H_{i,j}(\vec{k}) - \varepsilon_{\vec{k}} S_{i,j}(\vec{k}) \right] c_{\vec{k},j} = 0. \tag{2.12}$$

The energy spectrum is given by the solution of the linear secular equations and differs from the eigenvalues of the Hamilton matrix due to non-zero overlap. Hence, usually it is more convenient to use an orthogonal basis, in which the overlap matrix elements are assumed to be zero except for the on-site matrix elements. The next approximation is to take only a finite and but as small as necessary number of orbitals into account. The number of solutions of the secular equation in Eq. (2.12) and within the number of described bands corresponds to the dimension of the Hamilton matrix,

$$\dim = 2 \times O \times A \tag{2.13}$$

Here $O$ is the number of the included orbitals, $A$ is the number of atoms in the primitive unit cell, and the factor 2 is due to spin. In the final nearest-neighbor approximation (NNA) only the nearest neighbors of a chosen atom are taken into account in the Hamilton and the overlap matrix elements Eqs. (2.7) and (2.8). The NNA requires that the localized atomic orbitals decay exponentially at distances exceeding the inter-atomic distance. In the following sections we will apply the presented model and approximations to graphene and discuss first a simple two-band model by considering only the $p_z$ orbitals. Later we will introduce a multi-orbital model considering all $s$, $p$, and $d$ orbitals. In order to describe the band structure along all high-symmetry lines the non-orthogonal basis is needed. Fortunately, the restriction of the wave vectors $k$ to the vicinity of the high-symmetry K points allows to neglect the overlap parameters.

## 2.2 Lattice structure of graphene

Graphene is the only of known quasi two-dimensional crystal with the atomic thickness. The carbon atoms are ordered in a honeycomb structure (see Fig. 2.1), which corresponds to a triangular lattice with two atom in the unit cell. One identifies two triangular sublattices denoted by A and B. Every sublattice is spanned by the lattice vectors

$$\vec{a}_1 = \frac{a}{2} \begin{pmatrix} 1 \\ \sqrt{3} \end{pmatrix} \qquad \vec{a}_2 = \frac{a}{2} \begin{pmatrix} -1 \\ \sqrt{3} \end{pmatrix}. \tag{2.14}$$

where $a = 0.246$ nm is the lattice constant. The Cartesian coordinate system is chosen in the way that the y-axes is parallel to the connection line of two neighboring atoms. The inter-atomic distance is smaller then the lattice constant

and corresponds to $a_0 = a/\sqrt{3}$. Due to the triangular symmetry each atom has three nearest neighbors and their positions with respect to the chosen atom are

$$\vec{R}_1 = \frac{a}{\sqrt{3}} \begin{pmatrix} 0 \\ 1 \end{pmatrix} \quad \vec{R}_2 = \frac{a}{2\sqrt{3}} \begin{pmatrix} -\sqrt{3} \\ -1 \end{pmatrix} \quad \vec{R}_3 = \frac{a}{2\sqrt{3}} \begin{pmatrix} \sqrt{3} \\ -1 \end{pmatrix}. \tag{2.15}$$

All the nearest neighbors are at the opposite sublattice of the chose atom. There are six atoms, which can be reached by the lattice vector with the norm $a$

$$\vec{R} = \{\vec{a}_1,\, \vec{a}_2,\, \vec{a}_2 - \vec{a}_1,\, -\vec{a}_1,\, -\vec{a}_2,\, \vec{a}_1 - \vec{a}_2\}\,, \tag{2.16}$$

which are consequently the second nearest neighbors of the chosen atom.

The reciprocal lattice of graphene is also a two-dimensional triangular lattice with the reciprocal lattice vectors defined by

$$\vec{b}_1 = \frac{2\pi}{\Omega}(\vec{a}_2 \times \vec{a}_3), \qquad \vec{b}_2 = \frac{2\pi}{\Omega}(\vec{a}_3 \times \vec{a}_1), \tag{2.17}$$

where $\vec{a}_3 = (0, 0, c)$ is the additional needed lattice vector, which originates from graphite structure and, consequently, $\Omega = |\vec{a}_1(\vec{a}_2 \times \vec{a}_3)| = \frac{\sqrt{3}}{2}a^2 c$ is the volume of the primitive unit cell of graphite. Hence, the two two-dimensional reciprocal lattice vectors of graphene results in

$$\vec{b}_1 = \frac{2\pi}{a}\frac{1}{\sqrt{3}} \begin{pmatrix} \sqrt{3} \\ 1 \end{pmatrix}, \qquad \vec{b}_2 = \frac{2\pi}{a}\frac{1}{\sqrt{3}} \begin{pmatrix} \sqrt{3} \\ -1 \end{pmatrix}. \tag{2.18}$$

The reciprocal lattice vectors define the hexagonal 1st BZ of graphene, which is shown in Fig. 2.1 in relation to the real lattice. The two opposite corners of the 1st BZ are defined by the wave vectors

$$\vec{K} = \frac{1}{3}(\vec{b}_1 + \vec{b}_2) = \frac{4\pi}{3a} \begin{pmatrix} 1 \\ 0 \end{pmatrix},$$
$$\vec{K}' = -\frac{1}{3}(\vec{b}_1 + \vec{b}_2) = \frac{4\pi}{3a} \begin{pmatrix} -1 \\ 0 \end{pmatrix},$$

which are physically inequivalent points, since they cannot be connected by the reciprocal lattice vectors Eq. (2.18). The degeneracy of the high-symmetry K and K′ points is given by the time inversion symmetry and is often called the valley degeneracy in the literature. The coordinates of the remaining equivalent high-symmetry K(K′) points can be obtain by a rotation of the corresponding wave vectors in Eq. (2.19) by the angle of $\pm 2\pi/3$ or by adding the reciprocal lattice vectors of Eq. (2.18). The importance of the K and K′ points in the electronic structure of single and few-layer graphene is due to the energy of the corresponding states that are close to the Fermi energy level. In graphene the so

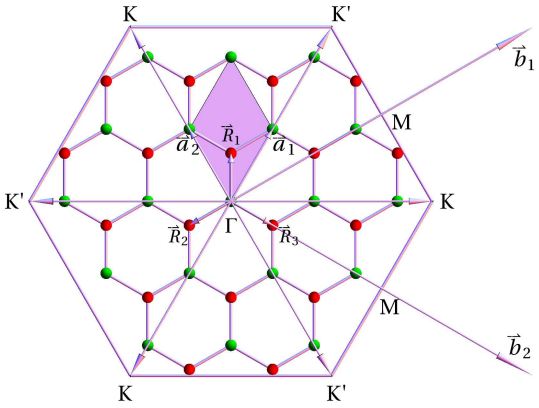


**Figure 2.1:** Real and reciprocal lattice of graphene.

called $\pi$ bands form the Dirac cones. The degeneracy points of the conduction and valence bands, the Dirac points, sit at the corners of the 1st BZ (the K and K′ points). In the following section we use the TB model to describe the $\pi$ bands of graphene and derive a two-band Hamiltonian, which models the Dirac cones.

## 2.3 Two-band Tight-binding model

In the discussion of the graphene structure we pointed out that there are two atoms in the primitive unit cell, which form two triangular sublattices A and B. Hence the Bloch wave function can be constructed by two sublattice resolved Bloch wave functions[1]

$$\Psi_{\vec{k}}(\vec{r}) = \sum_{\mu} \left( a_{\vec{k},\mu} \Psi^{A}_{\vec{k},\mu}(\vec{r}) + b_{\vec{k},\mu} \Psi^{B}_{\vec{k},\mu}(\vec{r}) \right), \tag{2.19}$$

where the coefficients $a_{\vec{k}}$ and $b_{\vec{k}}$ can be interpreted as the amplitudes of the sublattice pseudospin. The pseudospin 'up' state corresponds to the electron density localized at sublattice A and the 'down' state at sublattice B. As we will show below the concept of the pseudospin occurs from the special form of the resulting Hamiltonian, which has the same form as the famous Dirac Hamiltonian for relativistic particles.

For the description of the electronic structure of graphene we use the NNA. One of the special properties of graphene lattice is that all the three nearest neighbors of a chosen atom belong to the opposite sublattice. Thus the Hamilton

[1] The spin is omitted and the notation of the on-site Bloch function in Eq. (2.2) is changed by $\Psi_{\vec{k},1,\mu} = \Psi^{A}_{\vec{k},\mu}$ and $\Psi_{\vec{k},2,\mu} = \Psi^{B}_{\vec{k},\mu}$.

matrix elements in Eq. (2.7), which are diagonal in the pseudospin, have only on-site TB parameters,

$$\begin{aligned} H^{\mathrm{AA}}_{\nu,\mu}(\vec{k}) = H^{\mathrm{BB}}_{\nu,\mu}(\vec{k}) &= \frac{1}{N}\sum_{\vec{R},\vec{R}'} e^{i\vec{k}(\vec{R}-\vec{R}')} \int d\vec{r}\phi^*_{\mathrm{A}\nu}(\vec{r}-\vec{R}')H\phi_{\mathrm{A}\mu}(\vec{r}-\vec{R}) \\ &= \sum_{\vec{R}''} e^{i\vec{k}\vec{R}''} \int d\vec{r}\phi^*_{\nu}(\vec{r})H\phi_{\mu}(\vec{r}-\vec{R}'') \\ &\approx \int d\vec{r}\phi^*_{\nu}(\vec{r})H\phi_{\mu}(\vec{r}) = \varepsilon_\ell \delta_{\nu,\mu}, \end{aligned} \tag{2.20}$$

which correspond to the energies $\varepsilon_\ell$ of the atomic orbitals, where $\ell = \{s, p, d, ..\}$ is the angular momentum of the orbitals $\mu$. The hopping parameters and the wave-vector dependence of the Hamiltonian are given in the off-diagonal elements of the pseudo-spin basis. The Hamilton matrix elements of Eq. (2.7) are given by

$$\begin{aligned} H^{\mathrm{AB}}_{\nu,\mu}(\vec{k}) = \left(H^{\mathrm{BA}}_{\nu,\mu}(\vec{k})\right)^\dagger &= \frac{1}{N}\sum_{\vec{R},\vec{R}'} e^{\mathrm{i}\vec{k}(\vec{R}-\vec{R}')} \int d\vec{r}\phi^*_{\mathrm{A}\nu}(\vec{r}-\vec{R}')H\phi_{\mathrm{B}\mu}(\vec{r}-\vec{R}) \\ &= \sum_{\vec{R}''} e^{\mathrm{i}\vec{k}\vec{R}''} \int d\vec{r}\phi^*_{\nu}(\vec{r})H\phi_{\mu}(\vec{r}-\vec{R}''-\vec{R}_1) \\ &\approx e^{-\mathrm{i}\vec{k}\vec{R}_1}\sum_{m=1}^{3} e^{\mathrm{i}\vec{k}\vec{R}_m} \int d\vec{r}\phi^*_{\nu}(\vec{r})\hat{H}\phi_{\mu}(\vec{r}-\vec{R}_m), \end{aligned} \tag{2.21}$$

where the index $m$ denotes the nearest neighbors atoms of Eq. (2.15). The integration variable was shifted by $\vec{r} \to \vec{r} + \vec{R}'$ and $\vec{R}'' = \vec{R} - \vec{R}'$. The positions vectors of the neighboring atoms $\vec{R}_m = \vec{R}'' + \vec{R}_1$ are consistent with Eq. (2.15) using in the summation the lattice vectors $\vec{R}'' = \{\vec{0},\, -\vec{a}_1,\, -\vec{a}_2\}$ only. [2]

In the same fashion the overlap matrix elements in the NNA read

$$S^{\mathrm{AA}}_{\nu,\mu}(\vec{k}) = S^{\mathrm{BB}}_{\nu,\mu}(\vec{k}) \approx \int d\vec{r}\phi^*_{\nu}(\vec{r})\phi_{\mu}(\vec{r}) = \delta_{i,j}, \tag{2.22}$$

$$S^{\mathrm{AB}}_{\nu,\mu}(\vec{k}) = \left(S^{\mathrm{BA}}_{\nu,\mu}(\vec{k})\right)^\dagger \approx e^{-\mathrm{i}\vec{k}\vec{R}_1}\sum_{m=1}^{3} e^{\mathrm{i}\vec{k}\vec{R}_m} \int d\vec{r}\phi^*_{\nu}(\vec{r})\phi_{\mu}(\vec{r}-\vec{R}_m). \tag{2.23}$$

The electronic properties in graphene are given by the $\pi$ bondings created by the transverse the $p_z$ orbitals of the $sp^2$ hybridized carbon atoms. Hence

[2] The phase factor $e^{-\mathrm{i}\vec{k}\vec{R}_1}$ in front of the nearest neighbor summations of Eqs. (2.21) and (2.22) is due to the fact that we use the same lattice vectors to expand both sublattice resolved wave-functions defined in Eq. (2.19). In the usual TB models of graphene [1] one defines the sublattice dependent lattice vectors $R_{\mathrm{A}} = R$ and $R_{\mathrm{B}} = R + R_1$ such that the phase factor vanishes. In this work we get rid of it by redefining the coefficient $b_{\vec{l},\mu}$ in Eq. (2.19).

to describe the transport properties of graphene it is enough to include only $p_z$ orbitals in the TB model. Due to the cylindrical symmetry of the $p_z$ orbitals the hopping and overlap parameters in Eqs. (2.21) and (2.22) are equivalent for all neighboring atom. In this chapter we call the resulting hopping parameter $t$ and the overlap parameter by $s$, and Eqs. (2.21) and (2.22) take the simple form

$$\begin{aligned} H^{\mathrm{AA}}_{p_z,p_z}(\vec{k}) &= H^{\mathrm{BB}}_{p_z,p_z}(\vec{k})^* = \varepsilon_p \,, \\ H^{\mathrm{AB}}_{p_z,p_z}(\vec{k}) &= H^{\mathrm{BA}}_{p_z,p_z}(\vec{k})^* = t f(\vec{k}) \,, \end{aligned} \tag{2.24}$$

$$\begin{aligned} S^{\mathrm{AA}}_{p_z,p_z}(\vec{k}) &= S^{\mathrm{BB}}_{p_z,p_z}(\vec{k})^* = 1 \,, \\ S^{\mathrm{AB}}_{p_z,p_z}(\vec{k}) &= S^{\mathrm{BA}}_{p_z,p_z}(\vec{k})^* = s f(\vec{k}) \,, \end{aligned} \tag{2.25}$$

with the wave-vector dependent phase function

$$f(\vec{k}) = \sum_m e^{\mathrm{i}\vec{k}\vec{R}_m}. \tag{2.26}$$

The resulting two-band secular equation,

$$\left[ \begin{pmatrix} 1 & s f(\vec{k}) \\ s f(\vec{k})^* & 1 \end{pmatrix}^{-1} \cdot \begin{pmatrix} \varepsilon_p & t f(\vec{k}) \\ t f(\vec{k})^* & \varepsilon_p \end{pmatrix} - \varepsilon_{\vec{k}} I \right] \cdot \begin{pmatrix} a_{\vec{k}} \\ b_{\vec{k}} \end{pmatrix} = 0 \tag{2.27}$$

leads to the energy dispersion of the $\pi$ bands

$$\varepsilon_{\pm,\vec{k}} = \frac{\varepsilon_p \pm t|f(\vec{k})|}{1 \pm s|f(\vec{k})|} \tag{2.28}$$

where the $(+)$ denotes the valence and the $(-)$ the conduction band, because $t < 0$ and $s > 0$ for the $p_z$ orbitals if the hopping direction is normal to the $p_z$ orbital. The valence and conduction bands touch each other at the K(K′) points (see Fig. 2.2), such that $\varepsilon_{\pm,\vec{K}} = \varepsilon_p \equiv \varepsilon_F = 0$ and the eigenvectors

$$\begin{pmatrix} a^+_{\vec{k}} \\ b^+_{\vec{k}} \end{pmatrix} = \begin{pmatrix} f(\vec{k})/|f(\vec{k})| \\ 1 \end{pmatrix}, \qquad \begin{pmatrix} a^-_{\vec{k}} \\ b^-_{\vec{k}} \end{pmatrix} = \begin{pmatrix} 1 \\ -f^*(\vec{k})/|f(\vec{k})| \end{pmatrix}, \tag{2.29}$$

are degenerate at the Fermi energy $\varepsilon_F$ since $f(\vec{K}) = f(\vec{K}') = 0$, and are usually seem to be localized either at the sublattice A $(+)$ or B $(-)$. For $\vec{k} \neq K$ the conduction- and valence-band wave function are equally distributed on the both sublattices.

The energy range of interest for the experiments is roughly up to 100 meV with respect to the Dirac-point energy ($\varepsilon_p = 0$). For reasonable values of the parameters, $t \approx 3\,\mathrm{eV}$ and $s \approx 0.13$ [1] the energy dispersion in Eq. (2.28) becomes trapped in the vicinity to the K points. In this region the phase function

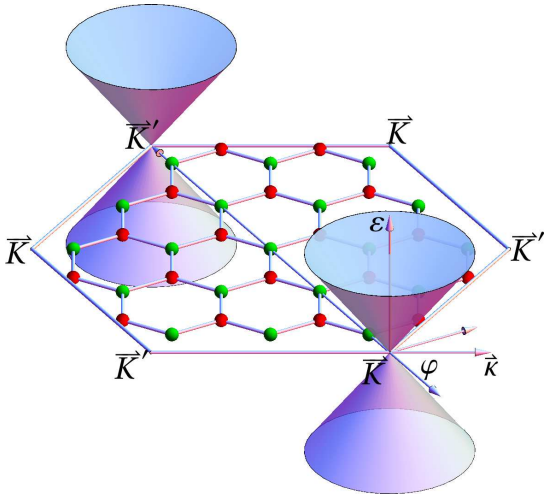


**Figure 2.2:** The cone-like band-structure of graphene at the K and K′ points, corners of the shown 1st BZ.

$f(\vec{k})$ can be expand up to the first order in $|\vec{\kappa}|$ where $\vec{k} = \vec{K} + \vec{\kappa}$ with $|\vec{\kappa}| \ll |\vec{K}|$. The overlap parameter $s$ gives only small correction to the group velocity, hence it can be set to zero. The resulting secular equation is then given by the famous Dirac Hamiltonian

$$H_0 = -v_F^0 \hbar(\tau\sigma_x\kappa_x + \sigma_y\kappa_y) \tag{2.30}$$

with the Fermi velocity $v_F^0 = \sqrt{3}ta/(2\hbar)$ being roughly $10^6$ m/s. The Pauli matrices $\sigma_i$ with $i = \{x, y, z\}$ represent the sublattice pseudospin in analogy to the real spin with a quantization axis in the $\hat{z}$ direction. The parameter $\tau = \pm 1$ denotes the K and K′ valleys, respectively. The eigenvalues of the Dirac Hamiltonian in Eq. (2.28) yields an energy dispersion that is linear in the absolute value of the wave vector $\vec{\kappa}$,

$$\varepsilon_{\pm,\vec{\kappa}} = \varepsilon_p \pm \hbar v_F^0 |\vec{\kappa}| a, \tag{2.31}$$

whose cone-like form is shown in Fig. 2.2. The electrons described by the Dirac Hamiltonian appear to be massless particles in terms of the Dirac notation [3]. Such analogy to the relativistic physics gives the opportunity to study the relativistic effect in the solid state material. It is a paradox that the relativistic effect of spin-orbit coupling (SOC) destroys this picture giving the electrons a small but finite mass. The study of the effects of coupling of spin and angular momentum requires an extension of the TB model by taking more orbitals into account.

[3] The effective mass of electrons in graphene defined by the inverse of the second derivative of Eq. (2.31) is infinite.

## 2.4 The Slater Koster two-center approximation

In the previous section we have considered only $p_z$ orbitals for the description of the two $\pi$ bands in graphene. The $\pi$ bands are related to the chemical $\pi$ bondings built by the non-hybridized out-of-plane $p_z$ orbitals of the $sp^2$ hybridized carbon atoms. The remaining valence electrons create the $\sigma$ bonding states with the electrons of neighboring atoms. These are very strong bonds and the energies of the corresponding valence band lies deep (up to 20 eV) below the Fermi energy. To describe the full band structure of graphene all relevant atomic orbitals have to be taken into account. To reduce the number of the corresponding hopping and overlap parameters one can exploit the symmetries of the atomic orbitals. The so-called rotating atomic orbitals $\phi_{\ell,m}$ are identified by the angular momentum $\ell = \{s, p, d, ...\}$ and the magnetic quantum number $m$. Due to spherical symmetry of the atomic potential the orbital function

$$\phi_{\ell m}(\vec{r}) = R_l(r) Y_{\ell m}(\theta, \varphi) \tag{2.32}$$

can be separated in the radial part $R_\ell(r)$ and the angular part $Y_{lm}(\theta, \varphi)$. The angular part is described by the spherical harmonics

$$Y_{lm}(\theta, \varphi) = (-1)^m \sqrt{\frac{(2l+1)(l-m)!}{4\pi(l+m)!}} P_l^m(\cos\theta) e^{\mathrm{i}m\varphi}\,, \tag{2.33}$$

which are presented here in the Condon-Shortlay notation. The hopping and overlap integrals between those atomic orbitals, which are localized on the atoms at the positions $\vec{R}$ and $\vec{R}'$,

$$\begin{aligned} V_{\ell\ell'|m|}\delta_{mm'} &= \left\langle \ell', m', \vec{R}' \right| \hat{H} \left| \ell, m, \vec{R} \right\rangle, \\ S_{\ell\ell'|m|}\delta_{mm'} &= \left\langle \ell', m', \vec{R}' | \ell, m, \vec{R} \right\rangle, \end{aligned} \tag{2.34}$$

are called Slater-Koster (SK) parameters [39] if the relative vector $\vec{R} - \vec{R}'$ is parallel to the quantization axes of the orbitals $\phi_{\ell m}(\vec{r} - \vec{R}) = \left\langle \vec{r} | \ell, m, \vec{R} \right\rangle$. The SK parameters are diagonal in the magnetic number $m$. Each value of $m$ is related to the different kind of bonding given by the superpositions the atomic-orbital wave functions. The different bonding types are denoted by the Greek letters $\sigma$, $\pi$, $\delta$ which correspond to the magnetic numbers $m = \{0, 1, 2\}$, respectively, and are related to the homonymous molecular orbitals, which are shown schematically in Fig. 2.4. The number of parameters is given by the number of possible combination of two orbitals and by the bonding type. The number of bonding types is given by $\min(\ell, \ell')$. Hence by taking only $s$, $p$, and

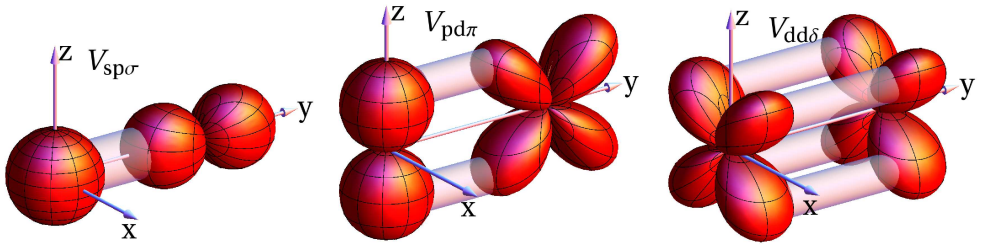


**Figure 2.3:** Sketch of SK hopping parameters $V_{sp\sigma}$, $V_{pd\pi}$ and $V_{dd\delta}$ that represent different kinds of bonding $\sigma$, $\pi$ and $\delta$, respectively, shown by the tunnels between the two orbital states.

$d$ orbitals into account there are 10 hopping and 10 overlap SK parameters

$$\begin{array}{llllll} V_{ss\sigma}, & V_{sp\sigma}, & V_{pp\sigma}, & V_{sd\sigma}, & V_{pd\sigma}, & V_{dd\sigma}, \\ V_{pp\pi}, & V_{pd\pi}, & V_{dd\pi}, & & V_{dd\delta}, & \\ S_{ss\sigma}, & S_{sp\sigma}, & S_{pp\sigma}, & S_{sd\sigma}, & S_{pd\sigma}, & S_{dd\sigma}, \\ S_{pp\pi}, & S_{pd\pi}, & S_{dd\pi}, & & S_{dd\delta}. & \end{array} \tag{2.35}$$

For arbitrary relative vector $\vec{R} - \vec{R}'$ the hopping and overlap integrals,

$$\left\langle \ell', m', \vec{R}' \middle| \hat{H} \middle| \ell, m, \vec{R} \right\rangle, \quad \text{and} \quad \left\langle \ell', m', \vec{R}' | \ell, m, \vec{R} \right\rangle, \tag{2.36}$$

are given by a linear combination of the SK parameters. The coefficients are given by the projection of the $z$ component of the participating orbital wave functions to the vector $\vec{R} - \vec{R}'$. The projection is similar to a rotation of the wave-function coordinates into a new coordinate system $\vec{r}'$. Thus the initial atomic orbitals are expressed by a linear combination of the wave functions in the rotated basis with the equivalent angular momentum $\ell$ and different magnetic number $m_1$

$$\phi_{\ell m}(\vec{r} - \vec{R}) = \sum_{m_1=-\ell}^{\ell} F^{(\ell)}_{m m_1}(\alpha, \beta) \phi_{\ell m_1}(\vec{r}' - \vec{R}). \tag{2.37}$$

The corresponding rotation matrices $F^{(\ell)}_{m m_1}(\alpha, \beta)$ are given by the Wigner for-

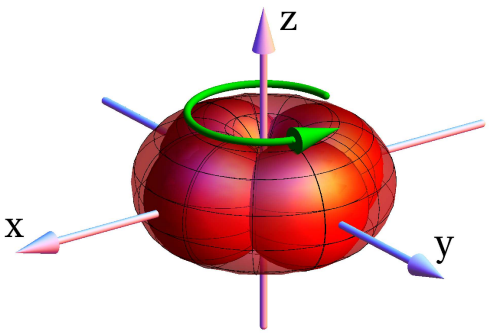


**Figure 2.4:** The shapes of the rotating and directed orbitals obtained by plotting the absolute values of spherical and cubic harmonics $|Y_{1,1}|$, and $|C_x|$ and $|C_y|$, respectively.

mula,[4]

$$
\begin{aligned}
F^{(\ell)}_{mm_1}(\alpha,\beta) &= e^{\mathrm{i}\alpha m} f^{(\ell)}_{mm_1}(\beta), \\
f^{(\ell)}_{mm_1}(\beta) &= \sum_t (-1)^t Q_t^{\ell m m_1} \cos\left(\frac{\beta}{2}\right)^{2\ell+m-m_1-2t} \sin\left(\frac{\beta}{2}\right)^{2t-m+m_1}, \\
Q_t^{\ell m m_1} &= \frac{\sqrt{(\ell+m)!(\ell-m)!(\ell+m_1)!(\ell-m_1)!}}{(\ell+m-t)!(\ell-m_1-t)!t!(t-m+m_1)!},
\end{aligned}
\tag{2.38}
$$

where only such values of $t$ contribute to the sum, which imply nonzero factorial arguments, and $\alpha, \beta$ are the Euler angles. The third Euler angle $\gamma$ is redundant due to the cylindrical symmetry of the atomic-orbital wave functions. The coefficients in the SK expansion of the Hamiltonian and overlap matrix elements are given by the product of the Wigner rotation matrices,

$$
\left\langle \ell', m', \vec{R}' \right| \hat{H} \left| \ell, m, \vec{R} \right\rangle = \sum_{m_1=-min(\ell,\ell')}^{min(\ell,\ell')} \left( F^{(\ell')}_{m'm_1}(\alpha,\beta) \right)^* F^{(\ell)}_{mm_1}(\alpha,\beta) V_{\ell\ell' m_1} \,. \tag{2.39}
$$

Instead of the rotating orbitals given by the spherical harmonics it is more usual to describe the atomic wave functions in terms of the directed orbitals. The directed orbitals are aligned along the axes of a chosen coordinate system. Figure 2.4 shows the rotating orbital $\phi_{1,1}(\vec{r})$, whose shape results from rotation of the also shown directed orbitals, $p_x$ and $p_y$, around the z-axes. Hence the

[4] A nice derivation of the Wigner formula by the means of harmonic oscillators can be found in the book of J. J. Sakurai in Ref [40]

| | Cubic | | | Spherical |
|---|---|---|---|---|
| s orbital: | $\|s\rangle$ | $=$ | $\frac{1}{\sqrt{4\pi}}\cdot \quad 1$ | $= \|0,0\rangle$ |
| p orbitals: | $\|p_z\rangle$ | $=$ | $\sqrt{\frac{3}{4\pi}\frac{1}{r}}\cdot \quad z$ | $= \|1,0\rangle$ |
| | $\|p_x\rangle$ | $=$ | $\sqrt{\frac{3}{4\pi}\frac{1}{r}}\cdot \quad x$ | $= \frac{1}{\sqrt{2}}\left(-\|1,1\rangle + \|1,-1\rangle\right)$ |
| | $\|p_y\rangle$ | $=$ | $\sqrt{\frac{3}{4\pi}\frac{1}{r}}\cdot \quad y$ | $= \frac{i}{\sqrt{2}}\left(\|1,1\rangle + \|1,-1\rangle\right)$ |
| d orbitals: | $\|d_{z^2}\rangle$ | $=$ | $\sqrt{\frac{5}{16\pi}\frac{1}{r^2}}\cdot \quad (3z^2-r^2)$ | $= \|2,0\rangle$ |
| | $\|d_{xz}\rangle$ | $=$ | $\sqrt{\frac{5}{16\pi}\frac{1}{r^2}}\cdot \quad 2\sqrt{3}\,xz$ | $= \frac{1}{\sqrt{2}}\left(-\|2,1\rangle + \|2,-1\rangle\right)$ |
| | $\|d_{yz}\rangle$ | $=$ | $\sqrt{\frac{5}{16\pi}\frac{1}{r^2}}\cdot \quad 2\sqrt{3}\,yz$ | $= \frac{i}{\sqrt{2}}\left(\|2,1\rangle + \|2,-1\rangle\right)$ |
| | $\|d_{xy}\rangle$ | $=$ | $\sqrt{\frac{5}{16\pi}\frac{1}{r^2}}\cdot \quad 2\sqrt{3}\,xy$ | $= \frac{i}{\sqrt{2}}\left(-\|2,2\rangle + \|2,-2\rangle\right)$ |
| | $\|d_{x^2-y^2}\rangle$ | $=$ | $\sqrt{\frac{5}{16\pi}\frac{1}{r^2}}\cdot \quad (x^2-y^2)$ | $= \frac{1}{\sqrt{2}}\left(\|2,2\rangle + \|2,-2\rangle\right)$ |

**Table 2.1:** Cubic harmonics represented in the Cartesian coordinates and as linear combination of the spherical harmonics with the coefficient $D^{(\nu)}_{\ell m}$.

angular part of the directed-orbital wave functions is given by the so-called cubic harmonics $C_\mu(\theta,\varphi)$, where

$$\phi_\mu(\vec{r}) = R_\ell(r) C_\mu(\theta,\varphi), \tag{2.40}$$

and the index $\mu = \{s, p_x, p_y, p_z, d_{xy}, \dots\}$ count all possible orbitals. It is more convenient to use Cartesian and not the polar coordinates to express the cubic harmonics. We show the cubic harmonics and their relation to the spherical harmonics with the coefficients $D^{(\nu)}_{\ell m}$ in Tab. 2.1. Finally the hopping parameters $t_{\mu,\nu}(\vec{n})$ are defined by the expectation values of the Hamiltonian in the basis of the directed orbitals

$$\begin{aligned} t_{\mu,\nu}(\vec{n}) &= \left\langle \mu, \vec{R}' \right| \hat{H} \left| \nu, \vec{R} \right\rangle \\ &= \sum_{m=-\ell}^{\ell} \sum_{m'=-\ell'}^{\ell'} D^{(\mu)*}_{\ell' m'} D^{(\nu)}_{\ell m} \sum_{m_1=-\min(\ell,\ell')}^{\min(\ell,\ell')} \left( F^{(\ell')}_{m' m_1}(\alpha,\beta) \right)^* F^{(\ell)}_{m m_1}(\alpha,\beta) V_{\ell\ell' m_1}, \end{aligned} \tag{2.41}$$

and are given by linear combinations of the SK parameters. The corresponding coefficients depend on the direction of the unit vector $\vec{n} = \left(\vec{R} - \vec{R}'\right)/|\vec{R} - \vec{R}'|$. The results of the evaluation of the Wigner rotation matrices in Eq. (2.41) are taken from [39] and shown in more applicable notation in Tab. 2.2, where the Euler angles are substituted by the Cartesian coordinates of the unit vector $\vec{n}$

| | |
|---|---|
| $\langle s\vert\,\hat{H}\,\vert s\rangle$ | $V_{ss\sigma}$ |
| $\langle s\vert\,\hat{H}\,\vert p_i\rangle$ | $n_i V_{sp\sigma}$ |
| $\langle s\vert\,\hat{H}\,\vert d_{ij}\rangle$ | $\sqrt{3}n_i n_j V_{sd\sigma}$ |
| $\langle s\vert\,\hat{H}\,\vert d_{x^2-y^2}\rangle$ | $\frac{\sqrt{3}}{2}\left(n_x^2-n_y^2\right)V_{sd\sigma}$ |
| $\langle s\vert\,\hat{H}\,\vert d_{z^2}\rangle$ | $-\frac{1}{2}\left(n_x^2+n_y^2-2n_z^2\right)V_{sd\sigma}$ |
| $\langle p_i\vert\,\hat{H}\,\vert p_i\rangle$ | $n_i^2 V_{pp\sigma}+\left(1-n_i^2\right)V_{pp\pi}$ |
| $\langle p_i\vert\,\hat{H}\,\vert p_j\rangle$ | $-n_i n_j(V_{pp\pi}-V_{pp\sigma})$ |
| $\langle p_i\vert\,\hat{H}\,\vert d_{ij}\rangle$ | $\sqrt{3}n_i^2 n_j V_{pd\sigma}+\left(1-2n_i^2\right)n_j V_{pd\pi}$ |
| $\langle p_i\vert\,\hat{H}\,\vert d_{jk}\rangle$ | $n_x n_y n_z\left(\sqrt{3}V_{pd\sigma}-2V_{pd\pi}\right)$ |
| $\langle p_x\vert\,\hat{H}\,\vert d_{x^2-y^2}\rangle$ | $\frac{\sqrt{3}}{2}n_x\left(n_x^2-n_y^2\right)V_{pd\sigma}+n_x\left(1-n_x^2+n_y^2\right)V_{pd\pi}$ |
| $\langle p_y\vert\,\hat{H}\,\vert d_{x^2-y^2}\rangle$ | $\frac{\sqrt{3}}{2}n_y\left(n_x^2-n_y^2\right)V_{pd\sigma}-n_y\left(1-n_y^2+n_x^2\right)V_{pd\pi}$ |
| $\langle p_z\vert\,\hat{H}\,\vert d_{x^2-y^2}\rangle$ | $\frac{\sqrt{3}}{2}n_z\left(n_x^2-n_y^2\right)V_{pd\sigma}-n_z\left(n_x^2-n_y^2\right)V_{pd\pi}$ |
| $\langle p_i\vert\,\hat{H}\,\vert d_{z^2}\rangle$ | $-\sqrt{3}n_i n_z^2 V_{pd\pi}-\frac{1}{2}n_i\left(n_x^2+n_y^2-2n_z^2\right)V_{pd\sigma}$ |
| $\langle p_z\vert\,\hat{H}\,\vert d_{z^2}\rangle$ | $\sqrt{3}n_z(n_x^2+n_y^2)V_{pd\pi}-\frac{1}{2}n_z\left(n_x^2+n_y^2-2n_z^2\right)V_{pd\sigma}$ |
| $\langle d_{ij}\vert\,\hat{H}\,\vert d_{ij}\rangle$ | $n_i^2 n_j^2\left(3V_{dd\sigma}-4V_{dd\pi}+V_{dd\delta}\right)+(n_i^2+n_j^2)V_{dd\pi}+n_k^2 V_{dd\delta}$ |
| $\langle d_{ij}\vert\,\hat{H}\,\vert d_{ik}\rangle$ | $n_i^2 n_j n_k(3V_{dd\sigma}-4V_{dd\pi}+V_{dd\delta})+n_j n_k(V_{dd\pi}-V_{dd\delta})$ |
| $\langle d_{xz}\vert\,\hat{H}\,\vert d_{x^2-y^2}\rangle$ | $\frac{1}{2}n_x n_z\left((n_x^2-n_y^2)(3V_{dd\sigma}-4V_{dd\pi}+V_{dd\delta})+2(V_{dd\pi}-V_{dd\delta})\right)$ |
| $\langle d_{yz}\vert\,\hat{H}\,\vert d_{x^2-y^2}\rangle$ | $\frac{1}{2}n_y n_z\left((n_x^2-n_y^2)(3V_{dd\sigma}-4V_{dd\pi}+V_{dd\delta})-2(V_{dd\pi}-V_{dd\delta})\right)$ |
| $\langle d_{xy}\vert\,\hat{H}\,\vert d_{x^2-y^2}\rangle$ | $\frac{1}{2}n_x n_y(n_x^2-n_y^2)(3V_{dd\sigma}-4V_{dd\pi}+V_{dd\delta})$ |
| $\langle d_{xz}\vert\,\hat{H}\,\vert d_{z^2}\rangle$ | $-\frac{1}{2}\sqrt{3}n_x n_z\left((n_x^2+n_y^2)\left(V_{dd\delta}-2V_{dd\pi}+V_{dd\sigma}\right)+2n_z^2(V_{dd\pi}-V_{dd\sigma})\right)$ |
| $\langle d_{yz}\vert\,\hat{H}\,\vert d_{z^2}\rangle$ | $-\frac{1}{2}\sqrt{3}n_y n_z\left((n_x^2+n_y^2)\left(V_{dd\delta}-2V_{dd\pi}+V_{dd\sigma}\right)+2n_z^2(V_{dd\pi}-V_{dd\sigma})\right)$ |
| $\langle d_{xy}\vert\,\hat{H}\,\vert d_{z^2}\rangle$ | $\frac{1}{2}\sqrt{3}n_x n_y\left(n_z^2(3V_{dd\sigma}-4V_{dd\pi}+V_{dd\delta})+V_{dd\delta}-V_{dd\sigma}\right)$ |
| $\langle d_{x^2-y^2}\vert\,\hat{H}\,\vert d_{z^2}\rangle$ | $\frac{1}{4}(n_x^2-n_y^2)\left(n_z^2(3V_{dd\sigma}-4V_{dd\pi}+V_{dd\delta})+V_{dd\delta}-V_{dd\sigma}\right)$ |
| $\langle d_{x^2-y^2}\vert\,\hat{H}\,\vert d_{x^2-y^2}\rangle$ | $\frac{1}{4}(n_x^2-n_y^2)^2(3V_{dd\sigma}-4V_{dd\pi}+V_{dd\delta})+(n_x^2+n_y^2)V_{dd\pi}+n_z^2 V_{dd\delta}$ |
| $\langle d_{z^2}\vert\,\hat{H}\,\vert d_{z^2}\rangle$ | $\frac{3}{4}(n_x^2+n_y^2)^2 V_{dd\delta}+3(n_x^2+n_y^2)n_z^2 V_{dd\pi}+\frac{1}{4}(n_x^2+n_y^2-2n_z^2)^2 V_{dd\sigma}$ |

**Table 2.2:** The hopping integral within the directed orbitals with the maximum angular momentum $\ell = 2$. We use the indices $i = \{x, y, z\}$, $j = \{x, y, z\}$, $k = \{x, y, z\}$ with the rule $i \neq j \neq k$. The complex conjugated hopping integrals are given by $\langle \ell\vert\,\hat{H}\,\vert \ell'\rangle = (-1)^{\ell+\ell'}\langle \ell'\vert\,\hat{H}\,\vert \ell\rangle$.

| $\mu \setminus \nu$ | $z$ | $xz$ | $yz$ |
|---|---|---|---|
| $z$ | $V_{pp\pi}$ | $n_x V_{pd\pi}$ | $n_y V_{pd\pi}$ |
| $xz$ | $-n_x V_{pd\pi}$ | $n_x^2 V_{dd\pi} + n_y^2 V_{dd\delta}$ | $n_x n_y (V_{dd\pi} - V_{dd\delta})$ |
| $yz$ | $-n_y V_{pd\pi}$ | $n_x n_y (V_{dd\pi} - V_{dd\delta})$ | $n_y^2 V_{dd\pi} + n_x^2 V_{dd\delta}$ |

**Table 2.3:** The hopping parameters $t^{\pi}_{\mu,\nu}(\vec{n})$ of the antisymmetric directed orbitals.

using the relation

$$n_x = \cos\alpha \sin\beta, \quad n_y = \sin\alpha \sin\beta, \quad n_z = \cos\beta. \tag{2.42}$$

The overlap of two displaced directed orbitals have exactly the same structure, where the SK hopping parameters $V_{\ell\ell'|m|}$ have to be replaced by the overlap parameters $S_{\ell\ell'|m|}$. Using the hopping parameters in Tab. 2.2 we now able to construct the multi-orbital TB Hamiltonian to model the band structure of graphene.

## 2.5 Multi-orbital tight-binding Hamiltonian

### 2.5.1 General structure with the nearest neighbor approximation

In the case of flat graphene the connecting vector $\vec{n}$ of two carbon atoms lies always in the plane ($n_z = 0$). Consequently, there is no hopping between symmetric and antisymmetric orbitals with respect to the graphene plane. This fact makes the TB Hamilton matrix block-diagonal. The two block matrices describe two different kinds of bands, the $\sigma$ and $\pi$ bands, respectively. Each of the two matrices can be diagonalized separately, what allows to study the structures of the $\pi$ and $\sigma$ bands independently of each other. The $\pi$ bands are built by the antisymmetric $(p_z, d_{xz}, d_{yz})$ orbitals and the corresponding hopping parameters $t^{\pi}_{\mu,\nu}(\vec{n})$ are shown in Tab. 2.3. The $\sigma$ bands evolve from the symmetric $(s, p_x, p_y, d_{xy}, d_{x^2-y^2}, d_{z^2})$ orbitals. The corresponding hopping parameter are not shown explicit here. But the important subset for further discussion, the hopping parameters of the $s$, $p_x$, and $p_y$ orbitals, have exactly the same structure as shown in Tab. 2.3 beside the SK hopping parameters must be replaced: $V_{pp\pi}$ by $V_{ss\sigma}$, $V_{pd\pi}$ by $V_{sp\sigma}$, $V_{dd\pi}$ by $V_{pp\sigma}$, and $V_{dd\delta}$ by $V_{pp\pi}$.

In the NNA the Hamilton matrices $H^{\pi}_{\vec{k}}$ and $H^{\sigma}_{\vec{k}}$,

$$H_{\pi}(\vec{k}) = \begin{pmatrix} H_{\pi}^{\mathrm{AA}} & H_{\pi}^{\mathrm{AB}} \\ H_{\pi}^{\mathrm{BA}} & H_{\pi}^{\mathrm{BB}} \end{pmatrix} = \begin{pmatrix} \mathrm{diag}\{\varepsilon_{\mathrm{p}}, \varepsilon_{\mathrm{d}}, \varepsilon_{\mathrm{d}}\} & \sum_{i=1}^{3} t^{\pi}(\vec{n}_i) e^{\mathrm{i}\vec{k}\cdot\vec{R}_i} \\ \sum_{i=1}^{3} t^{\pi}(-\vec{n}_i) e^{-\mathrm{i}\vec{k}\cdot\vec{R}_i} & \mathrm{diag}\{\varepsilon_{\mathrm{p}}, \varepsilon_{\mathrm{d}}, \varepsilon_{\mathrm{d}}\} \end{pmatrix} \quad (2.43)$$

$$H_{\sigma}(\vec{k}) = \begin{pmatrix} H_{\sigma}^{\mathrm{AA}} & H_{\sigma}^{\mathrm{AB}} \\ H_{\sigma}^{\mathrm{BA}} & H_{\sigma}^{\mathrm{BB}} \end{pmatrix} = \begin{pmatrix} \mathrm{diag}\{\varepsilon_{\mathrm{s}}, \varepsilon_{\mathrm{p}}, \varepsilon_{\mathrm{p}}, \varepsilon_{\mathrm{d}}, \varepsilon_{\mathrm{d}}\} & \sum_{i=1}^{3} t^{\sigma}(\vec{n}_i) e^{\mathrm{i}\vec{k}\cdot\vec{R}_i} \\ \sum_{i=1}^{3} t^{\sigma}(-\vec{n}_i) e^{-\mathrm{i}\vec{k}\cdot\vec{R}_i} & \mathrm{diag}\{\varepsilon_{\mathrm{s}}, \varepsilon_{\mathrm{p}}, \varepsilon_{\mathrm{p}}, \varepsilon_{\mathrm{d}}, \varepsilon_{\mathrm{d}}\} \end{pmatrix}, \quad (2.44)$$

of the $\pi$ and $\sigma$ bands, respectively, are given in the basis of the sublattice pseudospin. The diagonal block matrices $H^{\pi\backslash\sigma}_{\mathrm{AA}\backslash\mathrm{BB}}$ are diagonal in the basis of directed atomic orbitals. The diagonal elements correspond to the energies of the atomic orbitals $\varepsilon_{\ell}$, where $\ell = \{s, p, d\}$. The hopping parameters appear only in the off-diagonal block matrices $H^{\pi\backslash\sigma}_{\mathrm{AB}\backslash\mathrm{BA}}$, whose elements are tabulated in Tables 2.4 and 2.5, where the phase functions $f$, $g$ and $h$ are defined by

$$\begin{aligned} f = f(\vec{k}) &= e^{\mathrm{i}\vec{k}\vec{R}_1} + e^{\mathrm{i}\vec{k}\vec{R}_2} + e^{i\vec{k}\vec{R}_3} && \approx -\tau\frac{\sqrt{3}}{2}\kappa a e^{-\mathrm{i}\tau\varphi}, \\ g = g(\vec{k}) &= e^{\mathrm{i}\vec{k}\vec{R}_2} - e^{\mathrm{i}\vec{k}\vec{R}_3} && \approx -\mathrm{i}\tau\sqrt{3} + \frac{\mathrm{i}\kappa a}{2} e^{\mathrm{i}\tau\varphi}, \\ g = h(\vec{k}) &= 2e^{\mathrm{i}\vec{k}\vec{R}_1} - e^{\mathrm{i}\vec{k}\vec{R}_2} - e^{\mathrm{i}\vec{k}\vec{R}_3} && \approx 3 + \tau\frac{\sqrt{3}}{2}\kappa a e^{\mathrm{i}\tau\varphi}. \end{aligned} \quad (2.45)$$

The phase functions are expanded up to first order in the wave vector $\vec{\kappa}$ around the K ($\tau = +1$) and K′ ($\tau = -1$) points with $\vec{\kappa} = \vec{k} - \vec{K}(\vec{K}')$, $\kappa = |\vec{\kappa}| \ll |\vec{K}|$ and $\varphi = \arctan(\kappa_y/\kappa_x)$. This approximation makes the bands in the vicinity of the K points isotropic. The isotropy is proved by FP calculations, where the energies dispersions along the KΓ and KM line differs less than 5% at about 200 meV from the Fermi energy, setting the scale for the anisotropy.

| $\mu \setminus \nu$ | $z$ | $xz$ | $yz$ |
|---|---|---|---|
| $z$ | $4fV_{pp\pi}$ | $-2\sqrt{3}gV_{pd\pi}$ | $2hV_{pd\pi}$ |
| $xz$ | $2\sqrt{3}gV_{pd\pi}$ | $2f\tilde{V}^{+}_{dd} + h\tilde{V}^{-}_{dd}$ | $-\sqrt{3}g\tilde{V}^{-}_{dd}$ |
| $yz$ | $-2hV_{pd\pi}$ | $-\sqrt{3}g\tilde{V}^{-}_{dd}$ | $2f\tilde{V}^{+}_{dd} - h\tilde{V}^{-}_{dd}$ |

**Table 2.4:** Hopping part of the TB Hamiltonian $4H^{\pi}_{\mathrm{AB}}$ of the $\pi$ bands, where $\tilde{V}^{\pm}_{dd} = V_{dd\delta} \pm V_{dd\pi}$.

| $\mu \setminus \nu$ | $s$ | $x$ | $y$ | $xy$ | $x^2-y^2$ | $z^2$ |
|---|---|---|---|---|---|---|
| $s$ | $4fV_{ss\sigma}$ | $-2\sqrt{3}gV_{sp\sigma}$ | $2hV_{sp\sigma}$ | $3gV_{sd\sigma}$ | $-\sqrt{3}hV_{sd\sigma}$ | $-2fV_{sd\sigma}$ |
| $x$ | $2\sqrt{3}gV_{sp\sigma}$ | $2fV^{+}_{pp} + hV^{-}_{pp}$ | $-\sqrt{3}gV^{-}_{pp}$ | $2fV^{-}_{pd} + hV^{+}_{pd}$ | $-\sqrt{3}gV^{+}_{pd}$ | $\sqrt{3}gV_{pd\sigma}$ |
| $y$ | $-2hV_{sp\sigma}$ | $-\sqrt{3}gV^{-}_{pp}$ | $2fV^{+}_{pp} - hV^{-}_{pp}$ | $-\sqrt{3}gV^{+}_{pd}$ | $2fV^{-}_{pd} - hV^{+}_{pd}$ | $-hV_{pd\sigma}$ |
| $xy$ | $3gV_{sd\sigma}$ | $-2fV^{-}_{pp} - hV^{+}_{pp}$ | $4\sqrt{3}gV^{+}_{pd}$ | $\frac{1}{4}\left(2fV^{+}_{dd} - hV^{-}_{dd}\right)$ | $\frac{1}{4}\sqrt{3}gV^{-}_{dd}$ | $\frac{3}{2}g(V_{dd\delta} - V_{dd\sigma})$ |
| $x^2-y^2$ | $-\sqrt{3}hV_{sd\sigma}$ | $\sqrt{3}gV^{+}_{pd}$ | $-2fV^{-}_{pp} + hV^{+}_{pp}$ | $\frac{1}{4}\sqrt{3}gV^{-}_{dd}$ | $\frac{1}{4}\left(2fV^{+}_{dd} + hV^{-}_{dd}\right)$ | $\frac{\sqrt{3}}{2}h(V_{dd\sigma} - V_{dd\delta})$ |
| $z^2$ | $-2fV_{sd\sigma}$ | $-\sqrt{3}gV_{pd\sigma}$ | $hV_{pd\sigma}$ | $\frac{3}{2}g(V_{dd\delta} - V_{dd\sigma})$ | $\frac{\sqrt{3}}{2}h(V_{dd\sigma} - V_{dd\delta})$ | $f\left(3V_{dd\delta} + V_{dd\sigma}\right)$ |

**Table 2.5:** Hopping part of the TB Hamiltonian $4H^{\pi}_{\mathrm{AB}}$ of the $\sigma$ bands, where $V^{\pm}_{pp} = V_{pp\pi} \pm V_{pp\sigma}$ $V^{\pm}_{pd} = V_{pd\pi} \pm \frac{\sqrt{3}}{2}V_{pd\sigma}$ $V^{\pm}_{dd} = V_{dd\delta} \pm 4V_{dd\pi} + 3V_{dd\sigma}$.

### 2.5.2 Band structure of the multi-orbital TB Hamiltonian including $s$ and $p$ orbitals

The band structure along the high-symmetry lines is shown in Fig. 2.5(a) with the Fermi energy at the Dirac points. The top picture shows a relative agreement between the band structures obtained by FP calculations and the multi-orbital the TB Hamiltonian in the NNA, considering $s$ and $p$ orbitals only. The NNA is too crude to reproduce the exact shape of the bands given by the FP calculations. The significant deviation between the TB and FP calculations can be found in the $\sigma$-valence bands (red circles and green squares), specially in the energy spectra of the wave vectors around the M point of first and second lowest bands, and around the K points of the third lowest band. The shapes of the $\sigma$-conduction bands (red circle and green squares) bands differ strongly due to the interaction with higher orbitals, which are not included in the TB model. The $\pi$ bands spectra (blue diamonds) are well reproduced by the TB model but there are significant differences for the wave vector in the vicinity of the M points. We believe that including the second and third nearest neighbors into TB model would result in a better agreement between the TB the FP band structures. But every additional neighbor complicates the TB model by doubling the number of hopping and overlap parameters, which have to be fitted to reproduce the full band structure. In this thesis we are interested mostly in the energy spectrum given in the vicinity of the K points at the Fermi energy. In this region the error of the TB spectrum due to the NNA is insignificant. The values of the SK parameters Eq. (2.35) are derived by fitting the TB energy spectra at the high-symmetry points ($\Gamma$, K) to the results of the FP calculations. The problem is overdetermined, the number of solutions of the secular equation Eq. (2.12) is larger than the number of used SK parameters. Hence we chose such solutions for the fitting procedure, which give the best agreement with the band structure results of the FP calculation. In order to find the best description of the two $\pi$ bands and the $\sigma$-valence bands at the same time following solution provide the best results

$$\varepsilon^{p_z}_{\Gamma,\pm} = \frac{\varepsilon_p \pm 3V_{pp\pi}}{1 \pm 3S_{pp\pi}}, \quad \varepsilon^{s}_{\Gamma,\pm} = \frac{\varepsilon_s \pm 3V_{ss\sigma}}{1 \pm 3S_{ss\sigma}}, \quad \varepsilon^{p_{x,y}}_{\Gamma,\pm} = \frac{\varepsilon_p \pm 3/2(V_{pp\pi} + V_{pp\sigma})}{1 \pm 3/2(S_{pp\pi} + S_{pp\sigma})}, \tag{2.46}$$

$$\varepsilon^{p_{x,y}}_{\mathrm{K},\pm} = \frac{\varepsilon_p + \varepsilon_s - 9S_{sp\sigma}V_{sp\sigma} \pm \sqrt{(\varepsilon_p - \varepsilon_s)^2 + 18(V^2_{sp\sigma} + S^2_{sp\sigma}\varepsilon_p\varepsilon_s - S_{sp\sigma}V_{sp\sigma}(\varepsilon_p + \varepsilon_s))}}{2 - 9S^2_{sp\sigma}}, \tag{2.47}$$

where ($\pm$) assigns bonding and anti-bonding states[5]. The absolute value of the energy of the bonding and anti-bonding states with respect to the Fermi energy

[5]The bonding states has lower energy.

| Parameter | $\varepsilon_p$ | $\varepsilon_s$ | $V_{ss\sigma}$ | $V_{sp\sigma}$ | $V_{pp\sigma}$ | $V_{pp\pi}$ |
|---|---|---|---|---|---|---|
| Value [eV] | 0 | 8.370 | -5.729 | 5.618 | 6.050 | -3.070 |
| Value [eV] | 0 | 8.868 | -6.769 | 5.580 | 5.037 | -3.033 |

| Parameter | $S_{ss\sigma}$ | $S_{sp\sigma}$ | $S_{pp\sigma}$ | $S_{pp\pi}$ |
|---|---|---|---|---|
| Value | 0.102 | -0.171 | -0.377 | 0.070 |
| Value | 0.212 | -0.102 | -0.146 | 0.129 |

**Table 2.6:** SK hopping and overlap parameters. The values are obtained by fitting the band structure to the results of the FP calculation at the Γ and K points (top row) compared with results given in Ref. [1] (bottom row).

is related to the hopping parameter and the relative energy difference is modeled by the non-zero overlap parameter. The challenge of this fitting method is to identify the states with the energies given in Eqs. (2.46) and (2.47) in the FP spectra. The correspondence between the TB and FP eigenstates is given the the degree of degeneracy and the orbital character. In both methods the eigenstates can be projected to the wave function with a certain angular momentum[6]. The larges coefficients in the corresponding expansion of a certain eigenstate determines the orbital character of the eigenstate. The successful identification of the energy levels in Eqs. (2.46) and (2.47) yields at set of non-linear equation for the SK parameters. The resulting values of the SK parameters are tabulated in Tab. 2.6.

The SK parameters depend on the inter-atomic distance [41]. Variation of the lattice constant in the FP calculation and the fitting method discussed above provide the shape of SK parameters as a function of the lattice constant ratio $\tilde{a}/a$. The resulting values of the SK parameters are shown by dots in Fig. 2.6 given in the interval of 80% to 220% of the original lattice constant $a$. The lines in Fig. 2.6 represent the fit to exponential functions of the type

$$(a + bx + cx^2 + dx^3)e^{-j^2 x}, \tag{2.48}$$

where $x = \tilde{a}/a$. The resulting functions allow to study the trends in the shape of the parameters beyond the presented interval of $x$. For large values of the artificial lattice constant ($x \gg 1$) the parameters decay exponentially to zero, where the further increase of $S_{pp\sigma}$ in Fig. 2.6 is an error of the NNA, which is due to the change in the ordering of the $\pi$ and $\sigma$ bands in the spectrum

[6] In the case of TB such wave functions correspond to atomic orbitals.

(a)

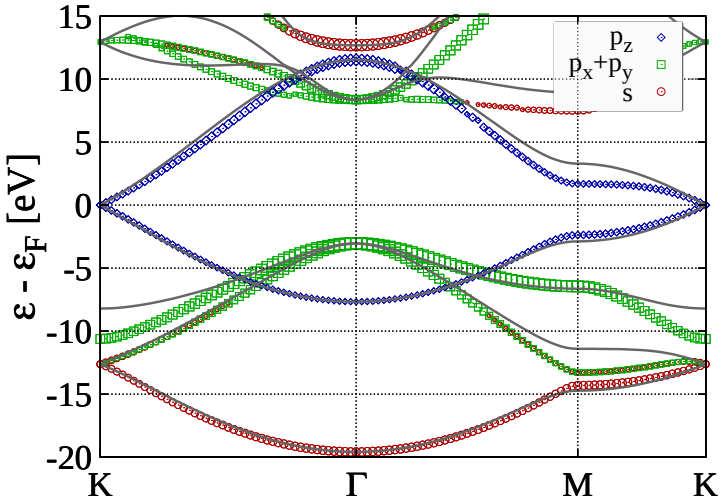


(b)

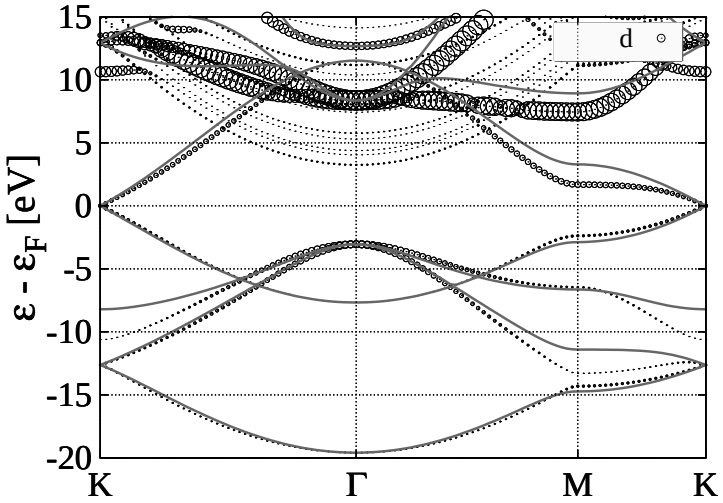


**Figure 2.5:** Calculated band structure of graphene obtained from FP calculations (symbols) and TB model (solid lines) using the parameters presented in Table 2.6. The size of the symbols reflects the contribution of the function with certain angular momentum to the corresponding eigenstates (a) $s$ and $p$ (b) $d$, where the symbols in (b) are increased by hand.

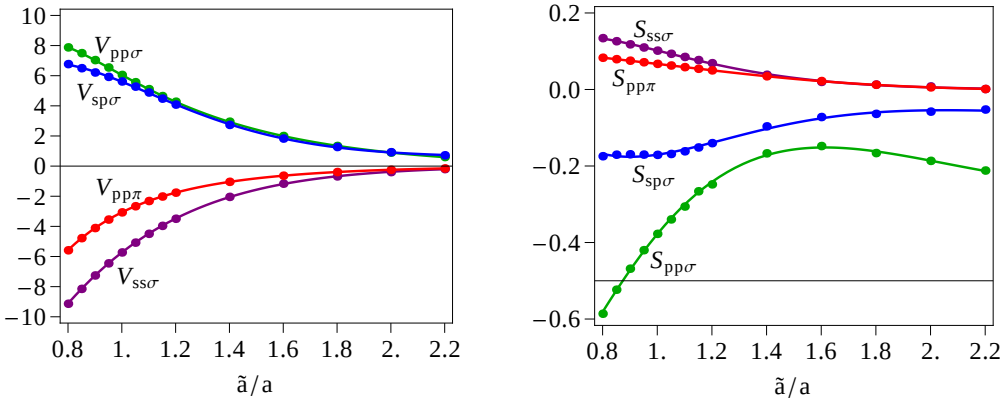


**Figure 2.6:** SK hopping $V_{\ell\ell'|m|}$ (left) (in eV) and overlap $S_{\ell\ell'|m|}$ (right) parameters as functions of the artificial lattice constant ratio.

at the Γ point. For small lattice constants the hopping (overlap) parameters should approach the atomic energies (one) if $\ell = \ell'$ and zero if $\ell \neq \ell'$ due to the orthogonality of the atomic orbitals. The functions, shown in Fig. 2.6, are used to test the formulas in the spectra of the effective Hamiltonians, given by SK parameters, with respect to the spectra obtained by multi-orbital TB Hamiltonian and FP calculations.

Figure 2.5 (b) shows the contribution of the $d$ orbitals to the states, which are primarily described by $s$ and $p$ orbitals [see Fig. 2.5(a)], as well as the additional bands with $d$ symmetry. The $d$ bands are split due to the interaction of the conduction bands states with the vacuum states, artifacts in the FP code. The splitting of the $d$ bands and their tiny contributions to the eigenstates make the identification of the correct states, built by the $d$-orbital in the TB model, very difficult. Hence, we had to find another way to obtain the values of the SK parameters related to the $d$ orbitals.

### 2.5.3 The $\pi$ band Hamiltonian

Figure 2.5(a) shows that the $\pi$ bands (blue diamonds) are mostly given by the $p_z$ orbitals. At the K points the two $\pi$ bands touch each the Fermi energy, which corresponds to $\varepsilon_p$, the energy of the $p$ orbitals, in the simple two-band model. In general $\pi$ bands are built from all the antisymmetric orbitals with respect to the graphene plane. In this section we will discuss the structure of the $\pi$ bands in the vicinity of the touching points, the Dirac points, including the $p$ and $d$ orbitals in the TB model. The TB Hamiltonian $H_\pi(\vec{k})$, which describes the $\pi$ bands, was already introduced in Eq. (2.43). By solving the secular equation $\det(H_\pi(\vec{k}) - \varepsilon I) = 0$ at the K(K′) point, where $I$ is the identity matrix (overlap

is neglected), the following two degenerate eigenstates can be identified at the Dirac points:

$$\begin{aligned} |1\rangle &= \frac{1}{\sqrt{N}}\left[\left|p_z^A\right\rangle + i\tilde{\gamma}(\tau\left|d_{xz}^B\right\rangle + i\left|d_{yz}^B\right\rangle)\right], \\ |2\rangle &= \frac{1}{\sqrt{N}}\left[\left|p_z^B\right\rangle + i\tilde{\gamma}(\tau\left|d_{xz}^A\right\rangle - i\left|d_{yz}^A\right\rangle)\right], \end{aligned} \tag{2.49}$$

with the corresponding normalization $N = 1 + 2\tilde{\gamma}^2$. The contribution of the $d$ orbitals to the eigenstates is given by $\tilde{\gamma} = 2\gamma/(1+\sqrt{1+8\gamma^2})$, where $\gamma = \frac{3}{2}V_{pd\pi}/(\varepsilon_d - \varepsilon_p)$ and the (Fermi) energy of the Dirac points is renormalized according to $\gamma$,

$$\varepsilon_F = \frac{1}{2}\left[(\varepsilon_d + \varepsilon_p) - (\varepsilon_d - \varepsilon_p)\sqrt{1+8\gamma^2}\right]. \tag{2.50}$$

The contribution of the $d$ orbitals to the $\pi$-band eigenstates at the K point in Eq. (2.49) is small according to our FP calculation. Hence, it is reasonable to assume $\gamma \ll 1$. Consequently, one obtains $\tilde{\gamma}/N \approx \gamma$ and the Fermi energy in Eq. (2.50) is shifted with respect to $\varepsilon_p$, such that $\varepsilon_F \approx \varepsilon_p - 2\gamma^2(\varepsilon_d - \varepsilon_p)$. It is evident that $\gamma$ and consequently $V_{pd\pi}$ controls the contribution from the $d$ orbital to the $\pi$ bands. The energy dispersion very close to the Dirac point remains linear. Here the $p$-$d$ coupling renormalizes the Fermi velocity according to $v_F = v_F^0(1-2\gamma^2)$. To obtain a quantitative estimate for $\gamma$, we calculate the density of states (DOS) close to the Fermi level using the definition

$$\mathcal{D}(\varepsilon) = \frac{2\Omega}{4\pi^2}\int_0^\infty kdk\int_0^{2\pi} d\varphi\ \delta(\varepsilon - \varepsilon_k) = \frac{\sqrt{3}a^2}{2\pi}k(\varepsilon)k'(\varepsilon), \tag{2.51}$$

where $\Omega = a^2\sqrt{3}/2$ is the surface of the unit cell in graphene. The inverse energy dispersion $k(\varepsilon)$ is obtained from the roots of the secular equation, where

$$\begin{aligned} &\det(H_\pi(\vec{k}) - \varepsilon\mathrm{I}) = (\varepsilon - \varepsilon_d)^2\times \\ &\times\left(\left[(\varepsilon-\varepsilon_p)(\varepsilon-\varepsilon_d) - \frac{1}{4}V_{pd\pi}^2(3|g|^2+|h|^2)\right]^2 - V_{pp\pi}^2(\varepsilon-\varepsilon_d)^2|f|^2\right). \end{aligned} \tag{2.52}$$

Here the hopping between the $d$ orbitals is neglected, because the corresponding hopping parameters $V_{dd\pi}$ and $V_{dd\delta}$ contribute primarily to the $d$-orbital states, whose energies are much larger than the Fermi energy and are at the order of $\varepsilon_d - \varepsilon_p$. This approximation is only valid for the wave vectors in the vicinity of the K points. Such restriction to the wave vectors $\vec{k}$ allows to expand the phase functions $|f|$ and $3|g|^2 + |h|^2$, given in Eq. (2.45), up to the first order in $\vec{\kappa} = \vec{k} - \vec{K}$. The resulting inverse energy dispersion,

$$\kappa(\varepsilon) = \pm\frac{1}{\sqrt{3}aV_{pp\pi}}\frac{2(\varepsilon-\varepsilon_p)(\varepsilon-\varepsilon_d) - 9V_{pd\pi}^2}{\varepsilon-\varepsilon_d}, \tag{2.53}$$

vanishes at the Dirac point with $\kappa(\varepsilon_F) = 0$. If the energies $\varepsilon(\vec{\kappa})$ of the two $\pi$ bands are close to the Fermi energy $\varepsilon_F$ the DOS in Eq. (2.51) can be approximated to

$$\mathcal{D}(\varepsilon) \approx \frac{\sqrt{3}a^2}{2\pi}\kappa'(\varepsilon_F)^2(\varepsilon - \varepsilon_F), \tag{2.54}$$

and becomes proportional to the first derivative of the inverse energy dispersion at the Dirac point,

$$\kappa'(\varepsilon_F) = \pm\frac{2}{\sqrt{3}aV_{pp\pi}}\left[1 + \frac{8\gamma^2}{1+\sqrt{1+8\gamma^2}}\right], \tag{2.55}$$

which is controlled by the ratio $\gamma$. As mentioned above it is reasonable assume $\gamma \ll 1$. Therefore the DOS can be expanded in powers of $\gamma$. Up to the second order the DOS is given by

$$\mathcal{D}(\varepsilon) \approx \mathcal{D}_0(\varepsilon)\left(1 + 2\gamma^2\right), \tag{2.56}$$

where $\mathcal{D}_0(\varepsilon) = 2(\varepsilon - \varepsilon_F)/\sqrt{3}\pi V_{pp\pi}^2$ is the linear DOS obtained neglecting the $d$ orbitals and the energy $\varepsilon$ is measured with respect to the Dirac point. The parameter $\gamma$ can be obtained by FP calculation of the DOS slopes close to the Fermi level including and excluding the $d$ orbitals. The ratio is 1.0306 and the slope $\mathcal{D}'_0(\varepsilon) = 0.0392\ (\mathrm{eV})^{-2}$. The extracted parameter $\gamma \approx 0.0871$ justifies the assumption $V_{pd\pi} \ll (\varepsilon_d - \varepsilon_p)$. The change of the Fermi velocity of only about 1.5 % is neglected in further calculations.

## 2.6 Tight-binding model of the spin-orbit coupling effect

### 2.6.1 Introduction to orbital effects

Relativistic effects, like spin itself and its coupling to the orbital motion of the electrons can be derived from the Dirac equation. In the non-relativistic limit the SOC appears as an additional term in the Schroedinger equation given by

$$\hat{H}_{\mathrm{SO}} = \frac{1}{2m^2c^2}(\vec{\nabla}V \times \vec{p}) \cdot \vec{S}, \tag{2.57}$$

where $m$ is a free electron mass, $c$ the speed of light, $\vec{p}$ canonical momentum and $\vec{S} = \frac{\hbar}{2}\vec{s}$ the spin vector operator, whose components are the Pauli matrices[7] $s_i$ with $i = \{x, y, z\}$. The SOC term in Eq. (2.57) can be interpreted as an effective

[7] In the literature the real spin Pauli matrices are denoted by the Greek letter $\sigma$. In this work it already used for the sublattice pseudospin.

Zeeman term in the rest frame of a moving electron, where the electric field, given by $\vec{\nabla}V$, acts as an effective magnetic field $\vec{B}_{\text{eff}} = (\vec{\nabla}V \times \vec{p})/mc^2$. In the two center approximation the potential $V(\vec{r})$ is approximated by the spherically symmetric atomic potential, where $V(r) := V(|\vec{r}|)$ and $\vec{\nabla}V = \frac{\vec{r}}{r}\frac{dV}{dr}$. In this approximation the SOC operator can be rewritten as a term which couples the spin and angular momentum operators

$$\hat{H}_{\text{SO}} = \xi(r)\vec{L}\cdot\vec{S}\,, \tag{2.58}$$

where the function $\xi(r)$ contains the entire radial dependence of the SOC Hamilton operator. The scalar product of the momentum and spin operators can be rewritten using the identity

$$\vec{L}\cdot\vec{S} = \frac{1}{2}\left(\hat{L}_+\hat{S}_- + \hat{L}_-\hat{S}_+\right) + \hat{L}_z\hat{S}_z, \tag{2.59}$$

in terms of ladder operators for spin and angular momentum,

$$\hat{L}_\pm = \hat{L}_x \pm i\hat{L}_y, \qquad \hat{S}_\pm = \hat{S}_x \pm i\hat{S}_y. \tag{2.60}$$

The ladder operators satisfy the commutation relations

$$\left[\hat{L}_+, \hat{L}_-\right] = 2\hbar\hat{L}_z, \quad \left[\hat{L}_z, \hat{L}_\pm\right] = \pm\hbar\hat{L}_\pm, \quad \text{and} \quad \left[\hat{L}_i, \hat{S}_j\right] = 0. \tag{2.61}$$

The atomic orbital wave functions, given by spherical harmonics $Y_{\ell,m}(\hat{r}) = \langle\hat{r}|\ell,m\rangle$, are eigenfunctions of the angular momentum. Such a successful choice of the basis for the kinetic part of the TB Hamiltonian allows us to apply the properties of the angular momentum algebra,

$$\hat{L}_z|\ell,m\rangle = \hbar m|\ell,m\rangle, \quad \hat{L}_\pm|\ell,m\rangle = \hbar\sqrt{\ell(\ell+1) - m(m\pm1)}|\ell,m\pm1\rangle, \tag{2.62}$$

to the atomic orbital. Using the orthogonality of the atomic orbitals we obtain a set of non-zero on-site expectations values of the SOC Hamiltonian

$$\left\langle \ell, m, \vec{R}\right| \hat{H}_{\text{SO}} \left|\ell', m', \vec{R}\right\rangle = \xi_\ell\,\delta_{\ell,\ell'}\,\langle\ell,m|\,\vec{L}\cdot\vec{S}\,|\ell',m'\rangle\,, \tag{2.63}$$

where the strength of the atomic SOC is defined by the TB parameter

$$\xi_\ell = \int_0^\infty dr R_\ell^2(r)\xi(r), \tag{2.64}$$

with the angular momentum quantum number $\ell$. Neither the radial part of the orbital wave functions $R_\ell(r)$ nor $\xi(r)$ are known explicitly for carbon atoms in graphene. Therefore the SOC parameters $\xi_\ell$ are arbitrary and must be fitted to reproduce the SOC effects in the band structure obtained by the FP calculations. The on-site matrix elements of the dimensionless angular part of the SOC Hamiltonian $\vec{L}\cdot\vec{s}/\hbar$ are tabulated in the Tabs. 2.7 and 2.8 (presented in the basis of rotating and directed orbitals, respectively). The hopping matrix elements of the SOC Hamiltonian between different atoms are assumed to be zero, because the spin-orbit interaction has its largest effect on electrons at the nucleus [42].

| orbital | $\|0,0\rangle$ | $\|1,-1\rangle$ | $\|1,0\rangle$ | $\|1,1\rangle$ |
|---|---|---|---|---|
| $\langle 0,0\|$ | 0 | 0 | 0 | 0 |
| $\langle 1,-1\|$ | 0 | $-s_z$ | $\frac{1}{\sqrt{2}}s_+$ | 0 |
| $\langle 1,0\|$ | 0 | $\frac{1}{\sqrt{2}}s_-$ | 0 | $\frac{1}{\sqrt{2}}s_+$ |
| $\langle 1,1\|$ | 0 | 0 | $\frac{1}{\sqrt{2}}s_-$ | $s_z$ |

| orbital | $\|2,-2\rangle$ | $\|2,-1\rangle$ | $\|2,0\rangle$ | $\|2,1\rangle$ | $\|2,2\rangle$ |
|---|---|---|---|---|---|
| $\langle 2,-2\|$ | $-2s_z$ | $s_+$ | 0 | 0 | 0 |
| $\langle 2,-1\|$ | $s_-$ | $-s_z$ | $\sqrt{\frac{3}{2}}s_+$ | 0 | 0 |
| $\langle 2,0\|$ | 0 | $\sqrt{\frac{3}{2}}s_-$ | 0 | $\sqrt{\frac{3}{2}}s_+$ | 0 |
| $\langle 2,1\|$ | 0 | 0 | $\sqrt{\frac{3}{2}}s_-$ | $s_z$ | $s_+$ |
| $\langle 2,2\|$ | 0 | 0 | 0 | $s_-$ | $2s_z$ |

**Table 2.7:** Matrix elements of the SOC operator $\vec{L}\cdot\vec{s}$ in the basis of $s$, $p$ and $d$ rotating orbitals.

| orbital | $\|s\rangle$ | $\|p_x\rangle$ | $\|p_y\rangle$ | $\|p_z\rangle$ |
|---|---|---|---|---|
| $\langle s\|$ | 0 | 0 | 0 | 0 |
| $\langle p_x\|$ | 0 | 0 | $-\mathrm{i}s_z$ | $\mathrm{i}s_y$ |
| $\langle p_y\|$ | 0 | $\mathrm{i}s_z$ | 0 | $-\mathrm{i}s_x$ |
| $\langle p_z\|$ | 0 | $-\mathrm{i}s_y$ | $\mathrm{i}s_x$ | 0 |

| orbital | $\|d_{xy}\rangle$ | $\|d_{x^2-y^2}\rangle$ | $\|d_{xz}\rangle$ | $\|d_{yz}\rangle$ | $\|d_{z^2}\rangle$ |
|---|---|---|---|---|---|
| $\langle d_{xy}\|$ | 0 | $2\mathrm{i}s_z$ | $-\mathrm{i}s_x$ | $\mathrm{i}s_y$ | 0 |
| $\langle d_{x^2-y^2}\|$ | $-2\mathrm{i}s_z$ | 0 | $\mathrm{i}s_y$ | $\mathrm{i}s_x$ | 0 |
| $\langle d_{xz}\|$ | $\mathrm{i}s_x$ | $-\mathrm{i}s_y$ | 0 | $-\mathrm{i}s_z$ | $\mathrm{i}\sqrt{3}s_y$ |
| $\langle d_{yz}\|$ | $-\mathrm{i}s_y$ | $-\mathrm{i}s_x$ | $\mathrm{i}s_z$ | 0 | $-\mathrm{i}\sqrt{3}s_x$ |
| $\langle d_{z^2}\|$ | 0 | 0 | $-\mathrm{i}\sqrt{3}s_y$ | $\mathrm{i}\sqrt{3}s_x$ | 0 |

**Table 2.8:** Matrix elements of the SOC operator $\vec{L}\cdot\vec{s}$ in the basis of $s$, $p$ and $d$ directed orbitals.

### 2.6.2 Stark effect

An external uniform electric field perpendicular to the graphene plane breaks spatial inversion symmetry [26, 9]. External electric fields can originate from a gate voltage or charged impurities in the substrate. We investigate the extrinsic SOC effects by including the additional term in the Hamiltonian,

$$\hat{H}_{\mathrm{SE}} = -eE\hat{z}, \tag{2.65}$$

where $e$ is the electron charge, $E$ is the strength of the electric field, and $\hat{z}$ is unit vector along $z$. In hydrogen atoms the external electric field leads to a splitting of the four degenerate states with principle quantum number $n = 2$. The splitting is linear in the field strength $E$ and therefore called linear Stark effect. Due to symmetry of the atomic orbitals, the Stark effect operator in Eq. (2.65) leads to the on-site coupling of orbitals with opposite parity: namely $s$ and $p_z$, and $p_z$ and $d_{z^2}$ orbitals. The corresponding matrix elements $eEz_{sp}$ and $eEz_{pd}$ are given by the expectation values of the dipole operator $\hat{z}$,

$$z_{sp} = \langle s|\, \hat{z}\, |p_z\rangle\,, \quad z_{pd} = \langle p_z|\, \hat{z}\, |d_{z^2}\rangle\,. \tag{2.66}$$

In analogy to the hydrogen atom we call such on-site coupling of orbitals the atomic single-particle Stark-effect. The electric field leads to a shift of the electron charge density inducing a dipole moment of 0.00134 C nm in the unit cell for a typical field of 1 V/nm [26]. Therefore, we assume that the matrix elements $eEz_{sp}$ and $eEz_{pd}$ are small as compared to $\varepsilon_p - \varepsilon_s$ and $\varepsilon_d - \varepsilon_p$. Hence, we expect no significant influence of the Stark effect on the shape of the bands in graphene. On the other hand the Stark effect term can play a important role in the SOC phenomena. We will show in the next chapter that the coupling of the $s$ and $p_z$ orbital due to external electric field will lead to the spin splitting of the $\pi$ bands.

### 2.6.3 Spin-orbit coupling Hamiltonian

Table 2.8 and Eq. (2.66) show that SOC and the Stark effect lead to additional non-vanishing on-site matrix elements in the TB Hamiltonian, such that the $\sigma$ and $\pi$ bands become coupled destroying the block-diagonal form of the TB Hamiltonian,

$$H = \begin{pmatrix} H_\pi & H_s \\ H_s^\dagger & H_\sigma \end{pmatrix} = \begin{pmatrix} H_\pi^{\mathrm{AA}} & H_\pi^{\mathrm{AB}} & H_s^{\mathrm{AA}} & 0 \\ H_\pi^{\mathrm{BA}} & H_\pi^{\mathrm{BB}} & 0 & H_s^{\mathrm{BB}} \\ H_s^{\mathrm{AA}} & 0 & H_\sigma^{\mathrm{AA}} & H_\sigma^{\mathrm{AB}} \\ 0 & H_s^{\mathrm{BB}} & H_\sigma^{\mathrm{BA}} & H_\sigma^{\mathrm{BB}} \end{pmatrix}. \tag{2.67}$$

| $\mu \setminus \nu$ | $\lvert s\rangle$ | $\lvert p_x\rangle$ | $\lvert p_y\rangle$ | $\lvert d_{xy}\rangle$ | $\lvert d_{x^2-y^2}\rangle$ | $\lvert d_{z^2}\rangle$ |
|---|---|---|---|---|---|---|
| $\langle z\rvert$ | $eEz_{sp}$ | $-\mathrm{i}s_y\xi_p$ | $\mathrm{i}s_x\xi_p$ | 0 | 0 | $eEz_{pd}$ |
| $\langle d_{xz}\rvert$ | 0 | 0 | 0 | $\mathrm{i}s_x\xi_d$ | $-\mathrm{i}s_y\xi_d$ | $\mathrm{i}\sqrt{3}s_y\xi_d$ |
| $\langle d_{yz}\rvert$ | 0 | 0 | 0 | $-\mathrm{i}s_y\xi_d$ | $-\mathrm{i}s_x\xi_d$ | $-\mathrm{i}\sqrt{3}s_x\xi_d$ |

**Table 2.9:** Matrix elements of the SOC operator $\vec{L}\cdot\vec{s}$ in the basis of $s$, $p$ and $d$ directed orbitals.

The new block matrices $H_s$ include only on-site elements and are, consequently, diagonal in the basis of pseudospin. The matrix elements of $H_s^{AA/BB}$, given in the basis of directed orbitals, are shown in Tab. 2.9 . In addition to $H_s$ there are non-zero on-site matrix elements due to SOC in the matrices $H_\pi^{AA/BB}$ and $H_\sigma^{AA/BB}$,

$$H_\pi^{AA} = H_\pi^{BB} = \begin{pmatrix} \varepsilon_p & 0 & 0 \\ 0 & \varepsilon_d & -\mathrm{i}s_z\xi_d \\ 0 & \mathrm{i}s_z\xi_d & \varepsilon_d \end{pmatrix}, \tag{2.68}$$

$$H_\sigma^{AA} = H_\sigma^{BB} = \begin{pmatrix} \varepsilon_s & 0 & 0 & 0 & 0 & 0 \\ 0 & \varepsilon_p & -\mathrm{i}s_z\xi_p & 0 & 0 & 0 \\ 0 & \mathrm{i}s_z\xi_p & \varepsilon_p & 0 & 0 & 0 \\ 0 & 0 & 0 & \varepsilon_d & 2\mathrm{i}s_z\xi_d & 0 \\ 0 & 0 & 0 & -2\mathrm{i}s_z & \varepsilon_d & 0 \\ 0 & 0 & 0 & 0 & 0 & \varepsilon_d \end{pmatrix}. \tag{2.69}$$

The non-vanishing matrix elements due to the SOC are linear in $s_z$, therefore $H_\pi^{AA/BB}$ and $H_\sigma^{AA/BB}$ are diagonal in the spin basis, but off-diagonal in the orbital basis, because the directed orbitals are not eigenstates of $L_z$. However in this thesis we restrict ourselves to the basis of directed orbitals to be consistent with previous works [42, 7]. Summarizing the results, the multi-orbital TB Hamiltonian has the form of Eq. (2.67), where the single block matrices are given in Eqs. (2.68) and (2.69) and Tabs. 2.4, 2.5, and 2.9.

## 2.7 Conclusion of the chapter

We have derived the multi-orbital TB Hamiltonian given in the basis of the directed $s$, $p$, and $d$ orbitals, which includes the atomic SOC and the Stark effect

term. The study of the SOC effects in graphene requires the diagonalization of the Hamilton matrix, which cannot be performed analytically. Therefore the SOC effect can be only obtained by effective models. In the next chapter we will present the derivation of the effective Hamiltonian given in the basis of $p_z$ orbitals. The prize to pay is the restriction of the validity of the effective Hamiltonian, it describes the bands with wave vectors in the vicinity of the K point and energies close to the Dirac point. However, this is the region of interest in the most experiment.

# 3 Effective Hamiltonians

## 3.1 Introduction to the derivation methods

In the previous chapter the band structure of graphene was studied by using the multi-orbital TB model and introducing the spin-independent Slater Koster hopping and overlap parameters. A qualitative description of the band structure resulting from our FP calculations was obtained considering only the nearest neighbors in the TB model. The on-site matrix elements in the TB Hamiltonian contain the energies of the orbitals and additional parameters due to the coupling of orbitals by the spin-orbit interaction. In the phenomenological descriptions of graphene [9, 43] the band modulation due to SOC is described by Hamiltonians, where the effect of SOC is described by spin-dependent nearest-neighbor (nn) or next-nearest-neighbor (nnn) hopping. As we pointed out in the previous chapter the SOC has its strongest effect around the atomic core. Hence any matrix elements of the SOC Hamiltonian in the basis of the orbitals localized on different atoms are negligible small, making any direct spin-dependent hopping between the atoms negligible. We present a physical interpretation of spin-dependent hopping, which can be treated as an effective hopping between the atomic $p_z$ orbitals.

In this chapter we derive an effective two-band Hamiltonian which includes SOC effects, intrinsic and extrinsic, using two different approximations: The perturbative transformation of the multi-orbital wave-vector dependent Hamilton matrix into block-diagonal form. The advantage of this method is that the SOC Hamiltonian is obtained instantly, but at the cost of a simple physical interpretation. A more illustrative method is to derive an effective spin-dependent nn and nnn hopping between the $p_z$ orbitals from the multi-orbital TB model, written in the basis of local atomic orbitals, by considering the nn hopping to other orbitals as a detour. Doing so, those empirical spin-dependent hopping parameters are expressed by TB parameters, which were introduced in the previous chapter.

This chapter is organized as follows: First we present a derivation of the Löwdin transformation and the idea behind it. The derivation for both effects, intrinsic and extrinsic, is performed by 'folding down' the multi-orbital Hamiltonian first into the subspace formed by the orbitals which describe the $\pi$ bands, followed by further 'folding down' to the subspace spanned by the $p_z$ orbitals.

The results will have two contributions: one due to the $s$ and $p$ orbitals which has already been obtained by H.Min *et al.* [23] via the degenerate perturbation theory, and another due to the $d$ orbitals. Both contributions are derived separately within the effective hopping method. The terminology and derivation of the effective hopping method are introduced first for a simple system, the linear chain of artificial atoms with two possible states: $p_z$ and $d_{xz}$ orbitals. Then the effective hopping method is applied to graphene and the single contributions to the SOC effects are derived sequentially.

In the last part of the chapter the different contributions will be discussed and shown that the $d$ orbitals dominate the intrinsic SOC but can be neglected in the discussion of the extrinsic BRSOC effect. At the end of the chapter we will discuss the spectrum of the effective Hamiltonian and its role for spin relaxation.

## 3.2 Löwdin method

The Löwdin partitioning is a general and powerful method for the approximate diagonalization of a Hamiltonian H [44]. It is similar to the conventional stationary perturbation theory, but more powerful because it does not distinguish between degenerate and non-degenerate states. The scheme of the Löwdin transformation makes use of a unitary anti-Hermitian operator $S$, such that the transformed Hamiltonian,

$$\tilde{H} = e^{-S} H e^{S} \approx H + [H, S] + \frac{1}{2}[[H, S], S], \tag{3.1}$$

has a block-diagonal form, where

$$S = \begin{pmatrix} 0 & M \\ -M^{\dagger} & 0 \end{pmatrix}, \tag{3.2}$$

and $M$ is an arbitrary matrix. The initial Hamilton matrix is divided into blocks,

$$H = \begin{pmatrix} H_0 & T \\ T^{\dagger} & \Delta \end{pmatrix}, \tag{3.3}$$

where $H_0$ model the bands of interest and $T$ is the interaction matrix of the subspaces of $H_0$ and $\Delta$. The only requirement for the Hamilton matrix $H$ is that the matrix elements in $T$ are small with respect to the eigenvalues of the matrix $\Delta$. We demand that the transformed Hamiltonian in Eq. (3.1) must be block-diagonal. Hence, the matrix $M$ can be obtained iteratively from the equation

$$T + H_0 M - M\Delta + M T^{\dagger} M = 0. \tag{3.4}$$

Keeping only the second order terms in $\Delta^{-1}$, the matrix $M$ reads as

$$M \approx T\Delta^{-1} + H_0 T\Delta^{-2}. \tag{3.5}$$

Inserting this expression into the Eq. (3.1), the first element includes the effective Hamiltonian

$$H_{\text{eff}} \approx H_0 - T\Delta^{-1}T^{\dagger}, \tag{3.6}$$

where the second and higher order terms in $\Delta^{-1}$ are neglected.

To obtain the effective SOC Hamiltonian in graphene we first 'fold down' the $\sigma$ states of the multi-orbital Hamilton matrix to the $\pi$ states, where $H_0$ corresponds to the $\pi$-bands matrix of Eq (2.43), $\Delta$ corresponds to $\sigma$-bands matrix of Eq (2.44), and $T$ includes the SOC matrix elements which couple the $\pi$ and $\sigma$ bands shown in Tab 2.9. These are small with respect to the energy difference of the orbitals $\varepsilon_d - \varepsilon_p$ and $\varepsilon_p - \varepsilon_s$. This fact verifies the requirements of the Löwdin partitioning. In the vicinity of the K point the approximation $\Delta^{-1}(\vec{k}) \approx \Delta^{-1}(\vec{K})$ is used implying that the kinetic part of the effective Hamiltonian is given by the $\pi$-bands Hamiltonian. Due to 'K point approximation' the resulting contributions to $H_0$ are constant in the wave vector $\vec{k}$. The 'K point approximation' sets the interval of validity for the effective Hamiltonian. It describes the band structure only in the vicinity of the K points as long as $|\vec{\kappa}|a \ll 1$, where $\vec{\kappa} = \vec{k} - \vec{K}$. The $\pi$ bands are built by $p$ and $d$ orbitals. Hence, the next step is to 'fold down' the effective Hamiltonian describing all $\pi$ bands to the two-band Hamiltonian given in the basis of two $p_z$ orbitals only.[1] Here the matrix $T$ includes the hopping between the $p$ and $d$ orbitals, which is assumed to be small with respect to the energy difference $\varepsilon_d - \varepsilon_p$. This assumption was verified by the results for the density of states shown in the previous chapter, where the ratio of the corresponding hopping parameter and the energy difference was given by $\gamma \approx\ll 1$. The matrix block $\Delta$ describes the conduction bands in graphene with only $d$ character. Such bands are separated by several electron volts from the Fermi energy in the vicinity of the K points. Therefore the 'K point approximation' is also reasonable in this case and can be applied.

The resulting effective two-band Hamiltonian includes three terms,

$$H_{\text{eff}} = H_0 + H_{\text{I}} + H_{\text{BR}}, \tag{3.7}$$

$H_0$ is the ordinary two-band Dirac Hamiltonian given by the $p_z$ orbitals in Eq. (2.30). The second term $H_{\text{I}}$ represents the intrinsic SOC effect, having the standard functional form [29],

$$H_{\text{I}} = \lambda_{\text{I}} \tau \sigma_z s_z, \tag{3.8}$$

[1] Spin is not considered, otherwise the effective Hamiltonian should be called four-band Hamiltonian.

where $\sigma_z$ and $s_z$ are the pseudospin and the real spin Pauli matrices, respectively, and $\tau \pm 1$ indicates the K and K′ points, respectively. The last term, $H_{\mathrm{BR}}$, is the extrinsic, BRSOC,

$$H_{\mathrm{BR}} = \lambda_{\mathrm{BR}} \left( \tau \sigma_x s_y - \sigma_y s_x \right), \tag{3.9}$$

which is off-diagonal in spin and pseudospin. Consequently, BRSOC couples spin and pseudospin degrees of freedom. The SOC parameters, $\lambda_{\mathrm{I}}$ and $\lambda_{\mathrm{BR}}$ are expressed by the SK and on-site parameters defined in the previous chapter. By keeping only the lowest order terms in $\xi_p$ and $\xi_d$, the intrinsic and extrinsic SOC parameters,

$$\lambda_{\mathrm{I}} \approx \frac{2(\varepsilon_p - \varepsilon_s)}{9V_{sp\sigma}^2} \xi_p^2 + \frac{9V_{pd\pi}^2}{2(\varepsilon_d - \varepsilon_p)^2} \xi_d \tag{3.10}$$

and

$$\lambda_{\mathrm{BR}} \approx \frac{2eEz_{sp}}{3V_{sp\sigma}} \xi_p + \sqrt{3} \frac{eEz_{pd}}{(\varepsilon_d - \varepsilon_p)} \frac{3V_{pd\pi}}{(\varepsilon_d - \varepsilon_p)} \xi_d \tag{3.11}$$

include two contributions coming from the $p$ and $d$ orbitals, respectively. The expression for the intrinsic and extrinsic parameters Eqs. (3.10) ans (3.11) are related to the effective hopping, which are given by sequences of nearest neighbor hopping and on-site 'hopping' between orbitals with the same angular momenta, provided by SOC and single-particle Stark effect. In the next section we present the derivation of effective hopping parameters, which originate from such hopping paths.

## 3.3 The effective hopping approximation

### 3.3.1 Linear chain

As an introduction to the effective hopping approximation we present a simple system, a linear chain of artificial atoms aligned in the $x$ direction. To stay related to graphene we allow only two possible states for the artificial atoms, the $p$ and $d_{xz}$ orbitals. We assume that the $d_{xz}$ orbitals have much higher energy than the $p$ orbitals, such that the two possible resulting bands are assumed to be coupled weakly and to be clearly separated in energy. We are only interested in the band energies with small differences to the energy of the $p_z$ orbitals, assuming $\varepsilon \approx \varepsilon_p$. Hence, the $d$-orbital states can be considered as virtual states with vanishing probability for electrons to stay in. In the following derivation of the effective Hamiltonian for the lower band built by $p$ orbitals we try to get rid of hopping to the $d$-orbital states. It is only possible at the cost of arising effective nnn hopping between the $p_z$ orbitals.

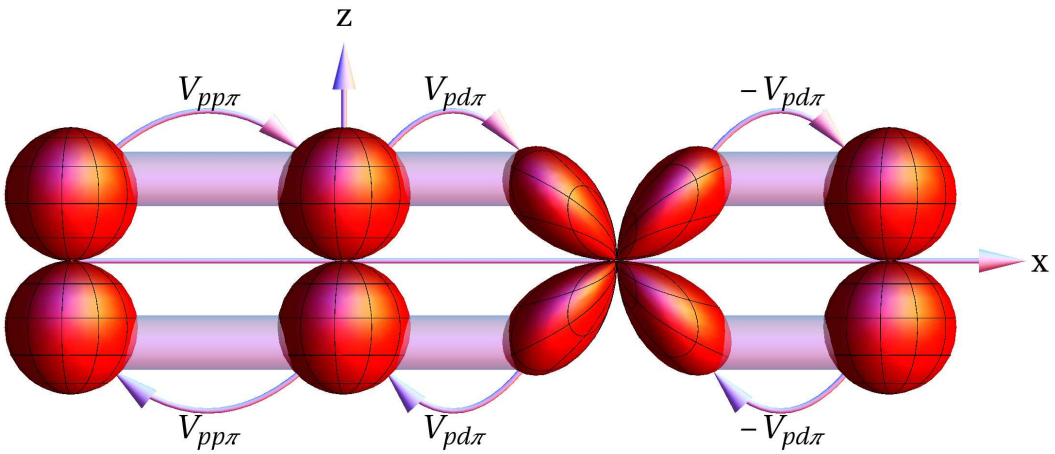


**Figure 3.1:** Sketch of a linear chain of artificial atoms with two possible states: $p_z$ and $d_{xz}$ orbitals. The parameter $V_{pp\pi}$ describes hopping between the neighboring $p$ orbitals and $V_{pd\pi}$ between the $p$ and $d_{xz}$ orbitals, where the $\pi$ bondings are represented by tunnels.

An appropriate model to describe electron moving through the linear chain by discrete steps is second quantization. The hopping can be interpreted as annihilation of the state $\mu$ at the atom $i$ and creation of the state $\nu$ at the atoms $j$. The corresponding tunneling energies are given by the hopping integrals $t_{\mu,i;\nu,j}$ and the Hamiltonian by

$$\hat{H} = \sum_{i,j=1}^{N} \sum_{\mu,\nu} \hat{a}^{\dagger}_{\mu,i} t_{\mu,i;\nu,j}\ \hat{a}_{\nu,j}, \tag{3.12}$$

where $\hat{a}^{\dagger}_{\mu,i}$, $\hat{a}_{\mu,i}$ are the corresponding creation and annihilation operators, respectively. A cut-out of the corresponding infinite hopping matrix $T$ is shown in Tab. 3.1 given in the basis of the $p_z$ and $d_{xz}$ orbitals localized at the $i$th atom, where only nearest-neighbor hopping is included. The diagonal matrix elements of $T$ are the energies of the atomic orbitals $\varepsilon_\ell$ with $\ell = \{p, d\}$ and the hopping integrals are given by the SK parameters

$$t_{z,i;z,i+1} = V_{pp\pi}, \quad t_{xz,i;xz,i+1} = V_{dd\pi}, \quad t_{z,i;xz,i+1} = n_x V_{pd\pi}, \tag{3.13}$$

where $n_x = \pm 1$ for a linear chain. The $d_{xz}$ orbital is odd under reflection with respect to the $yz$ plane, hence $t_{z,i;xz,i+1} = -t_{xz,i;z,i+1}$. Consequently, the sign of the hopping between $p$ and $d$ orbitals depends on the hopping direction and ordering of the orbitals. Figure 3.3.1 shows a draft of the linear chain with possible orbital states. The hopping direction is denoted by arrows and their notation illustrates the correct sign of the hopping integrals of Tab. 3.1.

| | $z,i-1$ | $xz,i-1$ | $z,i$ | $xz,i$ | $z,i+1$ | $xz,i+1$ |
|---|---|---|---|---|---|---|
| $z,i-1$ | $\varepsilon_p$ | $0$ | $V_{pp\pi}$ | $V_{pd\pi}$ | $0$ | $0$ |
| $xz,i-1$ | $0$ | $\varepsilon_d$ | $-V_{pd\pi}$ | $V_{dd\pi}$ | $0$ | $0$ |
| $z,i$ | $V_{pp\pi}$ | $-V_{pd\pi}$ | $\varepsilon_p$ | $0$ | $V_{pp\pi}$ | $V_{pd\pi}$ |
| $xz,i$ | $V_{pd\pi}$ | $V_{dd\pi}$ | $0$ | $\varepsilon_d$ | $-V_{pd\pi}$ | $V_{dd\pi}$ |
| $z,i+1$ | $0$ | $0$ | $V_{pp\pi}$ | $-V_{pd\pi}$ | $\varepsilon_p$ | $0$ |
| $xz,i+1$ | $0$ | $0$ | $V_{pd\pi}$ | $V_{dd\pi}$ | $0$ | $\varepsilon_d$ |

**Table 3.1:** A cut-out of the infinite hopping matrix $T$ of the linear chain of artificial atoms.

With the single particle ansatz $|\psi\rangle = \sum_{l,\rho} a_{\rho,l}\hat{a}^\dagger_{\rho,l}|0\rangle$ the corresponding Schrödinger equation gives the eigenvalue problem of the infinite hopping matrix $T$. The corresponding linear equations for the coefficients $a_{\mu,i}$ and $a_{\mu,i\pm1}$ with $\mu = \{z, xz\}$,

$$(\varepsilon - \varepsilon_p)a_{z,i} = V_{pp\pi}(a_{z,i-1} + a_{z,i+1}) + V_{pd\pi}(-a_{xz,i-1} + a_{xz,i+1}), \quad (3.14)$$

$$(\varepsilon - \varepsilon_d)a_{xz,i+1} = V_{dd\pi}(a_{xz,i} + a_{xz,i+2}) + V_{pd\pi}(a_{z,i} - a_{z,i+2}), \quad (3.15)$$

$$(\varepsilon - \varepsilon_d)a_{xz,i-1} = V_{dd\pi}(a_{xz,i-2} + a_{xz,i}) + V_{pd\pi}(a_{z,i-2} - a_{z,i}), \quad (3.16)$$

are coupled by the parameter $V_{pd\pi}$. Replacing $a_{xz,i\pm1}$ in Eq. (3.14) by their expression from Eqs. (3.15) and (3.16) yields an effective nnn hopping between the $p_z$ orbitals,

$$\begin{aligned}\left[\varepsilon - \varepsilon_p + 2\tilde{t}(\varepsilon)\right] a_{z,i} = {} & V_{pp\pi}(a_{z,i-1} + a_{z,i+1}) + \\ & + \tilde{t}(\varepsilon)(a_{z,i-2} + a_{z,i+2}) + \frac{V_{dd\pi}}{V_{pd\pi}}\tilde{t}(\varepsilon)(a_{xz,i-2} - a_{xz,i+2}),\end{aligned} \quad (3.17)$$

which is given by the parameter $\tilde{t}(\varepsilon) = V^2_{pd\pi}/(\varepsilon_d - \varepsilon)$ and with $\varepsilon \approx \varepsilon_p$ $\tilde{t}(\varepsilon) \approx \tilde{t}(\varepsilon_p) = \tilde{t}$. The parameter $\tilde{t}$ appears also on the left side of Eq. (3.17) since by making two steps along the chain two hopping paths return to the starting atom. The last term in Eq. (3.17) is the nnn hopping to the $d$ orbitals. As mentioned in the introduction to the linear chain, the $d$ orbital states are considered as virtual states. They can be interpreted as states in a potential barrier. In this picture a hopping between two neighboring $d$ states just makes the potential barrier wider. Consequently it is improbable for electrons to stay in the $d$ orbital state by moving through the chain. Hence the hopping within $d$ orbitals can be neglected. The corresponding effective Hamiltonian for the linear chain results from the eigenvalue problem of $p_z$ orbitals only and reads

$$\hat{H}_{\text{eff}} = \sum_{i=1}^{N}\left[\frac{1}{2}(\varepsilon_p - 2\tilde{t})\,\hat{a}^\dagger_{z,i}\hat{a}_{z,i} + V_{pp\pi}\,\hat{a}^\dagger_{z,i}\hat{a}_{z,i-1} + \tilde{t}\,\hat{a}^\dagger_{z,i}\hat{a}_{z,i-2} + \text{h.c.}\right]. \quad (3.18)$$

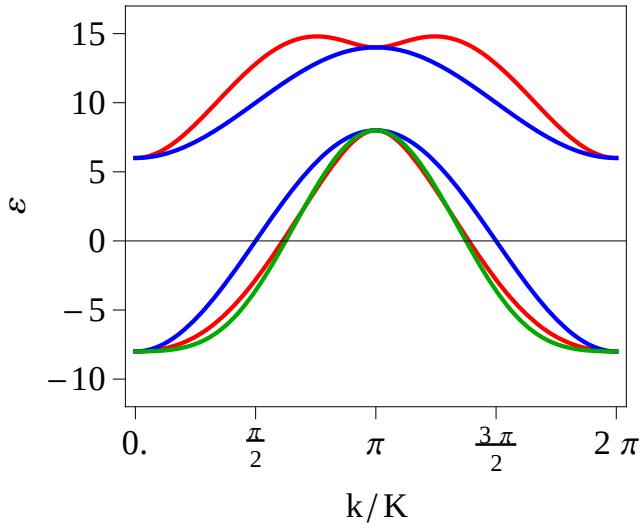


**Figure 3.2:** Band structure of the linear chain with $K = a^{-1}$ and the dimensionless arbitrary values of the parameters $\varepsilon_p = 0$, $\varepsilon_d = 10$, $t_p = -4$, $t_d = -2$. The red curve shows the two band structure with $t' = -3$, the green line the result of the one band approximation. The blue line shows decoupled bands, where $t' = 0$.

Due to translation symmetry the band structure, described by the effective Hamiltonian, can be obtained by the Fourier transformed creation and annihilation operators defined by

$$a^{\dagger}_{\nu,i} = \frac{1}{\sqrt{N}} \sum_{k'} a^{\dagger}_{\nu,k'} e^{-\mathrm{i}k'R_i}, \quad a_{\mu,i} = \frac{1}{\sqrt{N}} \sum_{k} a_{\mu,k} e^{\mathrm{i}kR_i}, \tag{3.19}$$

where $R_i$ is the translation vector. With $R_{i-1} = R_i - a$ and $R_{i-2} = R_i - 2a$, where $a$ is the inter-atomic distance in the chain, the effective Hamiltonian is given by

$$\hat{H} = \sum_{k,k'} a^{\dagger}_{z,k'} a_{z,k} \left[ t(e^{-\mathrm{i}ka} + e^{\mathrm{i}k'a}) + \tilde{t}(e^{-2\mathrm{i}ka} + e^{2\mathrm{i}k'a}) \right] \frac{1}{N} \sum_{i=1}^{N} e^{\mathrm{i}(k'-k)R_i}, \tag{3.20}$$

with the short-hand notation $t := V_{pp\pi}$. In the case of an infinite chain ($N \to \infty$) the summation over $R_i$ is replaced by the Kronecker $\delta_{k,k'}$. Thus, the summation over $k'$ disappears and the effective one-band Hamiltonian,

$$\hat{H} = \sum_{k} a^{\dagger}_{z,k} \left( te^{-\mathrm{i}ka} + \tilde{t}e^{-2\mathrm{i}ka} \right) a_{z,k} + h.c., \tag{3.21}$$

leads to the energy spectrum for a given wave-vector $k$

$$\varepsilon_k = \varepsilon_p - 2\tilde{t} + 2t\cos(ka) + 2\tilde{t}\cos(2ka), \tag{3.22}$$

which is shown in Fig. 3.2 for arbitrary values of the TB parameters with the restriction $t' \ll (\varepsilon_d - \varepsilon_p)$. The shape of the approximated band (green line) shows a good agreement with the results of the original two-band Hamiltonian[2] (red line) in contrast to the cruder and worse approximation, $t' = 0$, (blue line) where the two bands are considered as independent from each other. Thus the effective hopping method is very successful in describing the structure of chosen bands by a simple models.

### 3.3.2 Graphene: $d$ orbitals

In this section the effective hopping model will be applied to the $\pi$ bands of graphene to derive an effective Hamiltonian which describes the SOC effects in the vicinity of the Dirac points. In second quantization the Hamiltonian is given by the hopping integrals $t_{\mu,s,i;\nu,s',j}$,

$$\hat{H} = \sum_{i,j} \sum_{s,s'} \sum_{\mu,\nu} c^{\dagger}_{\mu,s,i}\, t_{\mu,s,i;\nu,s',j}\; c_{\nu,s',j}, \tag{3.23}$$

which describe the hopping between the orbitals $\mu$ and $\nu$ with a spin $s$ and $s'$ localized at the atoms $i$ and $j$ in the honeycomb lattice of graphene, respectively. For $i = j$ the hopping integrals are called on-site. In the basis of directed orbitals the on-site hopping corresponds to the energy of the orbitals if $\nu = \mu$ and $s = s'$ and to the SOC parameters if $\nu \neq \mu$ and allowed by symmetry. In graphene there are two atoms in the unit cell A or B, to identify the sublattices the general creation and annihilation operators $c^{\dagger}_{\mu,s,i}$, $c_{\nu,s',j}$ are replaced by $a^{\dagger}_{\mu,s,i}$, $a_{\nu,s',j}$ or $b^{\dagger}_{\mu,s,i}$, $b_{\nu,s',j}$ , respectively.

The $\pi$ bands of graphene are given in the basis of the antisymmetric orbitals $p_z$, $d_{xz}$, and $d_{yz}$, where the $d$ orbitals are coupled by the atomic spin-orbit interaction. In the previous chapter the coupling was taken into account by the on-site parameter $\xi_d$. The on-site matrix elements of the hopping matrix $T$ are given in Eq. (2.68). The nn hopping matrix elements $t_{\mu,i,s,\nu,j,s} \equiv t_{\mu,\nu}(\vec{n}_m)$ depend on the nearest neighbor position vectors $\vec{n}_m = \vec{R}_m/|\vec{R}_m|$ of Eq. (2.15) and are tabulated in Tab. 2.3. We chose an initial atom, denoted by 0, to be on the sublattice A. The corresponding eigenvalue problem in the NNA is than given by the linear equations of local orbitals denoted by $\mu = \{z, xz, yz\}$.

[2]The full two-band Hamiltonian can be obtained in the NNA by the Fourier transformation of the creation and annihilation operators already in Eq. (3.12).

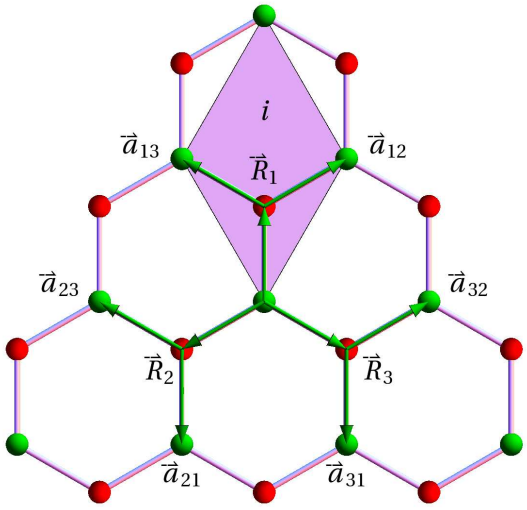


**Figure 3.3:** Honey comb structure of graphene showing the first and second nearest-neighbor vectors defined by $\vec{R}_m$ and $\vec{a}_{mm'} = \vec{R}_m - \vec{R}_{m'}$, respectively.

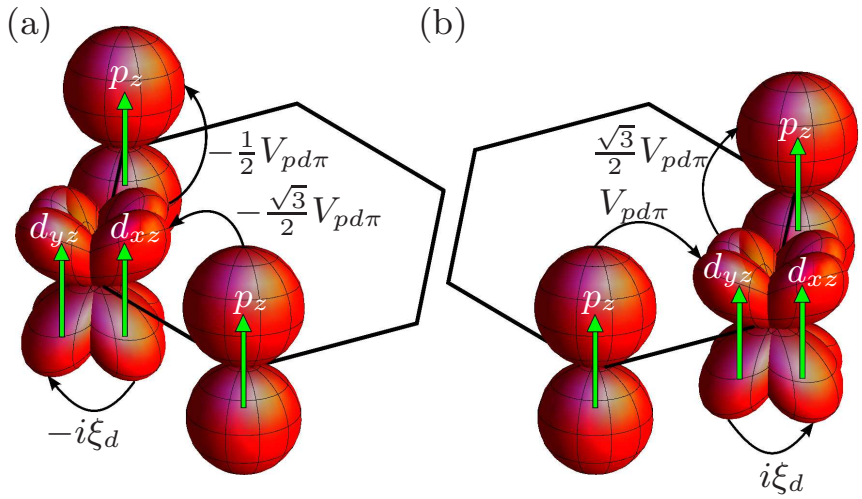


**Figure 3.4:** Two of the possible nnn hopping paths through the $d$ orbitals, (black) arrows. The spin is shown by (yellow) arrows on the orbitals. The opposite sign for clockwise (a) and anticlockwise (b) hopping is given by the opposite sign in the SOC of the $d$ orbitals.

$$
\begin{aligned}
(\varepsilon-\varepsilon_p)a_{z,0} &= \sum_{\mu,m} t_{z,\mu}(\vec{n}_m)b_{\mu,m},\\
(\varepsilon-\varepsilon_d)b_{xz,m} + \mathrm{i}s_z\xi_d b_{yz,m} &= \sum_{\mu,m'} t_{xz,\mu}(-\vec{n}_{m'})a_{\mu,mm'} =: X,\\
(\varepsilon-\varepsilon_d)b_{yz,m} - \mathrm{i}s_z\xi_d b_{xz,m} &= \sum_{\mu,m'} t_{yz,\mu}(-\vec{n}_{m'})a_{\mu,mm'} =: Y,
\end{aligned}
\tag{3.24}
$$

where $\{m, m'\} = \{1, 2, 3\}$ denotes the nearest neighbors of the given atom and spin index is omitted. The index in the equations for the $d$ orbitals is already shifted to the nearest neighbors $m$ of the initial atom. The nearest neighbors of atom $m$ are denoted by the double index $mm'$. The double index records the hopping history with respect to the initial atom. It denotes the second-nearest neighbors of the initial atom, shown in Fig. 3.3, or the initial atom itself if $m = m'$. The linear equations for $b_{xz,m}$ and $b_{yz,m}$ are coupled by non-zero SOC parameter $\xi_d$. The solutions of the two linear equations

$$
\begin{aligned}
b_{xz,m} &= \det{}^{-1}\left[(\varepsilon-\varepsilon_d)X - \mathrm{i}s_z\xi_d Y\right] \approx \frac{X}{\varepsilon_p-\varepsilon_d} - \frac{\mathrm{i}s_z\xi_d Y}{(\varepsilon_d-\varepsilon_p)^2},\\
b_{yz,m} &= \det{}^{-1}\left[(\varepsilon-\varepsilon_d)Y + \mathrm{i}s_z\xi_d X\right] \approx \frac{Y}{\varepsilon_p-\varepsilon_d} + \frac{\mathrm{i}s_z\xi_d X}{(\varepsilon_d-\varepsilon_p)^2},
\end{aligned}
\tag{3.25}
$$

are approximated using $\xi_d \ll |\varepsilon - \varepsilon_d|$ and consequently $\det = (\varepsilon-\varepsilon_d)^2 - \xi_d^2 \approx (\varepsilon_p-\varepsilon_d)^2$ if $\varepsilon \approx \varepsilon_p$. In graphene it is a reasonable assumption because the coupling of the orbitals by spin-orbit interaction in carbon atoms is of the order of several meV and the $\varepsilon_d - \varepsilon_p$ is of the order of 10 eV. In the vicinity of the K point the energy of four of the six $\pi$ bands[3] is at the order of $\varepsilon_d - \varepsilon_p$ with respect to the Dirac point. Therefore the hopping within the $d$ orbitals can be neglected by the arguments used in the discussion of the linear chain. The hopping between the $p_z$ orbitals and the neighboring $d$ orbitals is eliminated by inserting the expression from Eq. (3.25) into the equation for $a_{z,0}$ in Eq. (3.24),

$$
\begin{aligned}
(\varepsilon-\varepsilon_p)a_{z,0} = V_{pp\pi}\sum_m b_{z,m} - \tilde{t}\sum_m\sum_{m\neq m'}\sum_{\mu=x}^{y} n_{\mu,m}n_{\mu,m'}a_{z,mm'} - 3\tilde{t}a_{z,0}\\
- \mathrm{i}s_z t_{\mathrm{SO}}\sum_m\sum_{m\neq m'}(n_{x,m}n_{y,m'} - n_{y,m}n_{x,m'})a_{z,mm'}\,.
\end{aligned}
\tag{3.26}
$$

The first term on the right-hand side of Eq. (3.26) is the ordinary nn hopping. The seconds term is the resulting effective nnn hopping and is given by the

[3] Or eight of the twelve bands if spin is taken into account

parameter $\tilde{t} = V_{pd\pi}^2/(\varepsilon_d - \varepsilon_p)$ in analogy to the linear chain, where

$$\begin{aligned} t_{z,xz}(\vec{n}_m)t_{xz,z}(-\vec{n}_{m'}) &= V_{pd\pi}^2 n_{x,m}n_{x,m'}, \\ t_{z,xz}(\vec{n}_m)t_{yz,z}(-\vec{n}_{m'}) &= V_{pd\pi}^2 n_{x,m}n_{y,m'}, \\ t_{z,yz}(\vec{n}_m)t_{xz,z}(-\vec{n}_{m'}) &= V_{pd\pi}^2 n_{y,m}n_{x,m'}, \\ t_{z,yz}(\vec{n}_m)t_{yz,z}(-\vec{n}_{m'}) &= V_{pd\pi}^2 n_{y,m}n_{y,m'}. \end{aligned} \tag{3.27}$$

In the case of returning hopping path ($m = m'$) the double index $mm$ can be replaced by 0 and the summations of the products of components of the unit vectors $\vec{n}_m$ in the equations above,

$$\begin{aligned} \sum_m t_{z,xz}(\vec{n}_m)t_{xz,z}(-\vec{n}_m)a_{z,mm} &= V_{pd\pi}^2\, a_{z,0} \sum_m n_{x,m}^2 = \frac{3}{2}V_{pd\pi}^2 a_{z,0}, \\ \sum_m t_{z,xz}(\vec{n}_m)t_{yz,z}(-\vec{n}_m)a_{z,mm} &= V_{pd\pi}^2\, a_{z,0} \sum_m n_{x,m}n_{y,m} = 0, \\ \sum_m t_{z,yz}(\vec{n}_m)t_{xz,z}(-\vec{n}_m)a_{z,mm} &= V_{pd\pi}^2\, a_{z,0} \sum_m n_{y,m}n_{x,m} = 0, \\ \sum_m t_{z,yz}(\vec{n}_m)t_{yz,z}(-\vec{n}_m)a_{z,mm} &= V_{pd\pi}^2\, a_{z,0} \sum_m n_{y,m}^2 = \frac{3}{2}V_{pd\pi}^2 a_{z,0}, \end{aligned} \tag{3.28}$$

result in the third term in Eq. (3.26), which is associated with a shift of the energy of the Dirac points with respect to $\varepsilon_p$. The last term in Eq. (3.26) is an additional spin-dependent nnn hopping. The corresponding hopping parameter $t_{\mathrm{SO}} = \xi_d\, V_{pd\pi}^2/(\varepsilon_d - \varepsilon_p)^2$ is due to atomic SOC of the $d$ orbitals.

The evaluation of the remaining sums in Eq. (3.26) yields

$$\begin{aligned} \left[\varepsilon - (\varepsilon_p - 3\tilde{t})\right] a_{z,0} &= V_{pp\pi} \sum_m b_{z,m} - \frac{1}{2}\tilde{t} \sum_{m,m' \neq m} a_{z,mm'} \\ &+ \mathrm{i}s_z t_{\mathrm{SO}} \frac{\sqrt{3}}{2}(-a_{z,12} + a_{z,13} + a_{z,21} - a_{z,23} - a_{z,31} + a_{z,32}), \end{aligned} \tag{3.29}$$

where the spin-dependent nnn hopping has opposite signs for initial spin-up or spin-down states due to Pauli matrix $s_z$. There is a change of sign between clock-wise (-) and counter-clock-wise (+) nnn hopping. Figure 3.4 shows the corresponding clock-wise (a) and counter-clock-wise (b) hopping paths via the directed $d$ orbitals for the spin-up state. The sign of the nnn hopping is determined by the sign of the on-site coupling of the $d_{xz}$ and $d_{yz}$ orbitals. There is again a change of the sign if the initial atom is placed on the B sublattice.

Summarizing, we receive two additional terms to the Hamiltonian of the localized $p_z$ orbitals at the atomic position given by the vector $\vec{R}_i$,

$$\hat{H} = \sum_i (\varepsilon_p - 3\tilde{t})(\hat{a}_i^\dagger \hat{a}_i + \hat{b}_i^\dagger \hat{b}_i) + V_{pp\pi} \sum_{\langle i,j \rangle} (\hat{a}_i^\dagger \hat{b}_j + \mathrm{h.c.}) \tag{3.30}$$

where the energy of the $p_z$ orbitals is shifted by $3\tilde{t}$, and $j$ denotes three nearest neighbors of the atom $i$. The first additional term is the effective spin-conserving nnn hopping due to $d$ orbitals similar to the nnn effective hopping derived in the case of the linear chain,

$$\hat{H}_{\mathrm{D}} = \frac{1}{2}\tilde{t} \sum_{\langle\langle i,j \rangle\rangle} (\hat{a}_i^\dagger \hat{a}_j + \hat{b}_i^\dagger \hat{b}_j). \tag{3.31}$$

The second term is the spin-dependent nnn hopping due to SOC,

$$\hat{H}_{\mathrm{SO}} = \mathrm{i}\frac{\sqrt{3}}{2} t_{\mathrm{SO}} \sum_{\langle\langle i,j \rangle\rangle} \zeta_{i,j} (\hat{a}_i^\dagger s_z \hat{a}_j - \hat{b}_i^\dagger s_z \hat{b}_j), \tag{3.32}$$

where the orbital and spin labels are omitted and $j$ denotes the six second-nearest neighbors of atom $i$. The intrinsic SOC part of the effective Hamiltonian in Eq. (3.7) is obtained using the Fourier transformed creation and annihilation operators defined in Eq. (3.19), where the $d$ orbital contribution to the intrinsic SOC parameter is given at the K point by

$$\lambda_{\mathrm{I}}^{(d)} = \frac{9}{2} t_{\mathrm{SO}}\,, \tag{3.33}$$

and the ordinary nnn hopping results in a shift of the Dirac point by $\frac{9}{2}\tilde{t} = 2\gamma^2(\varepsilon_d - \varepsilon_p)$, which is consistent with the discussion of the $\pi$-band TB Hamiltonian in the previous chapter.

### 3.3.3 Graphene: $s$ and $p$ orbitals

In the preceding section we have shown that effective nnn hopping paths are going through $d$ orbitals, states with large energy differences with respect to the energy of the $p_z$ orbitals. An alternative to the $d$ orbitals are the $s$ orbitals. But in contrast to $d$ orbitals, the $s$ orbitals do not couple to $p_z$ via hopping by reasons of symmetry, but to the (in-plane) $p_x$ and $p_y$ orbitals. The effective nnn hopping between the $p_z$ orbitals is possible because the $p$ orbitals are coupled by the spin-orbit interaction. The eigenvalue problem for a chosen initial atom 0 on the sublattice A is given by the linear equations

$$(\varepsilon - \varepsilon_p) a_{x,0} = -\mathrm{i} s_z \xi_p a_{y,0} + \mathrm{i} s_y \xi_p a_{z,0} + \sum_{m=1}^{3} \sum_{\mu=\{s,x,y\}} t_{x\mu}(\vec{n}_m) b_{\mu,m}\,, \tag{3.34}$$

$$(\varepsilon - \varepsilon_p) a_{y,0} = \mathrm{i} s_z \xi_p a_{x,0} - \mathrm{i} s_x \xi_p a_{z,0} + \sum_{m=1}^{3} \sum_{\mu=\{s,x,y\}} t_{y\mu}(\vec{n}_m) b_{\mu,m}\,, \tag{3.35}$$

$$(\varepsilon - \varepsilon_p) a_{z,0} = -\mathrm{i} s_y \xi_p a_{x,0} + \mathrm{i} s_x \xi_p a_{y,0} + \sum_{m=1}^{3} t_{zz}(\vec{n}_m) b_{z,m}\,, \tag{3.36}$$

where the nearest neighbors of the initial atom are again counted by the index $m$. Here we face the dilemma that the equations diverge in the limit $\varepsilon \to \varepsilon_p$. In Eq. (3.29) we have shown that the nnn hopping results among other thing in the energy shift $3\tilde{t}$. A similar shift results by hopping through the $s$ orbitals which 'removes' the divergence of the equations for the in-plane $p$ orbitals. The hopping through in-plane $p$ orbital does not have such effect. Hence, the nn hopping between $p_x$ or $p_y$ orbitals can be omitted setting $\mu = s$. The equations for $a_{x,0}$ and $a_{y,0}$ are coupled via SOC. In the Löwdin method this coupling leads to terms which are at least third order in the SOC parameter $\xi_p$. Such terms, and therefore the coupling of the in-plane $p$ orbitals, can be neglected. Consequently, the equations Eqs. (3.34) and (3.35) are coupled via hopping only to the neighboring $s$ orbitals on the sublattice B. Furthermore the electron in the neighboring $s$ orbital states can move to their neighboring orbitals on A, denoted by $m'$,

$$(\varepsilon - \varepsilon_s) b_{s,m} = \xi_{sp} a_{z,m} + \sum_{m'} \sum_{\mu=\{s,x,y\}} t_{s\mu}(-\vec{n}_{m'}) a_{\mu,mm'}, \tag{3.37}$$

and to the $p_z$ orbitals on $m$ via the Stark effect parameter $\xi_{sp} = eEz_{sp}$, which was defined in previous chapter. The hopping between the $s$ orbitals can also be neglected here because of the same arguments used in the discussion of the $d$ orbitals. The effective nnn hopping between the $p_x$ and $p_y$ orbitals is obtained by inserting the Eq. (3.37) in the approximated equations for the in-plane $p$ orbitals Eqs. (3.34) and (3.35), where

$$\begin{aligned}
(\varepsilon - \varepsilon_p) a_{x,0} = \quad & \mathrm{i} s_y \xi_p a_{z,0} + t^{sp}(\varepsilon) \sum_m n_{m,x}\, a_{z,m} + \tilde{t}(\varepsilon) \sum_{m,m'} \sum_{\mu=\{x,y\}} n_{m,x} n_{m',\nu} a_{\mu,mm'}, \\
(\varepsilon - \varepsilon_p) a_{y,0} = & -\mathrm{i} s_x \xi_p a_{z,0} + t^{sp}(\varepsilon) \sum_m n_{m,y}\, a_{z,m} + \tilde{t}(\varepsilon) \sum_{m,m'} \sum_{\mu=\{x,y\}} n_{m,x} n_{m',\nu} a_{\mu,mm'},
\end{aligned} \tag{3.38}$$

and the double index in $a_{\mu,mm'}$ denotes again the second nearest neighbors of the initial atom as well as the initial atom itself if $m = m'$. The hopping integrals between the $s$ and $p$ orbitals, $t_{\mu,s}(\vec{n}_m) = t_{s,\mu}(-\vec{n}_m) = n_{m,\mu} V_{sp\sigma}$, are given by the Slater Koster parameter $V_{sp\sigma}$ and $n_{m,\mu}$, the $\mu$th component of the unit hopping vector $n_m$. The non-zero Stark effect parameter leads to the effective nn hopping parameter $t^{sp}(\varepsilon) = \xi_{sp} V_{sp\sigma}/(\varepsilon - \varepsilon_s)$ and the effective nnn hopping parameter is defined by $\tilde{t}(\varepsilon) \equiv V_{sp\sigma}^2/(\varepsilon - \varepsilon_s)$. The iteration of Eq. (3.38) allows us to write

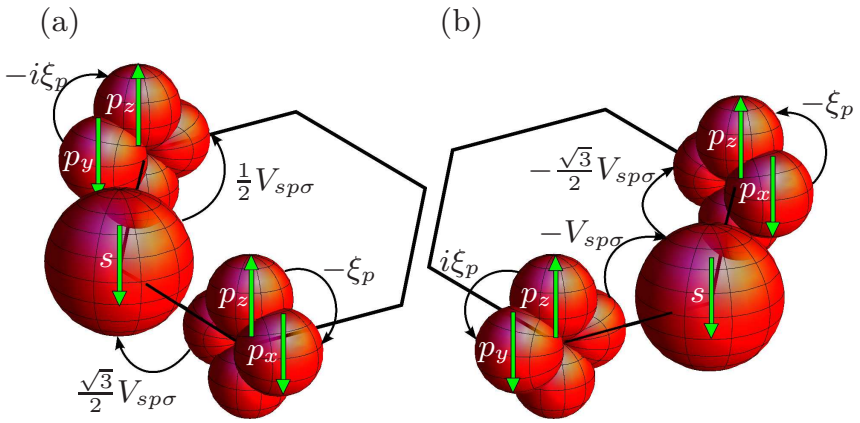


**Figure 3.5:** Two of the possible nnn hopping paths through the $s, p$ orbitals, (black) arrows, with a corresponding spin, shown by (yellow) arrows on the orbitals. The opposite sign for the clockwise (a) and the anticlockwise (b) effective hopping is determined by the signs of the two SOCs of the $p$ orbitals.

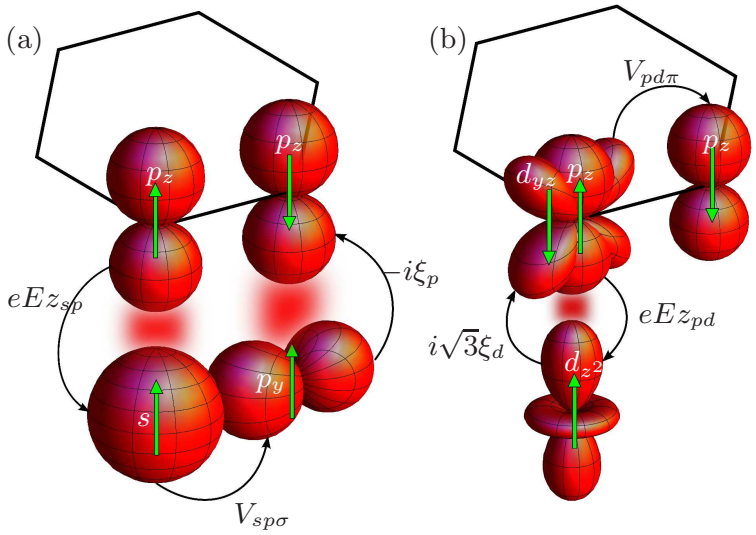


**Figure 3.6:** A representative leading hopping path, (black) arrows, which is responsible for the Bychkov-Rashba SOC effect, by coupling states of different spins, illustrated by (yellow) arrows on the orbitals. The effective hopping is between nearest neighbors. (a) The dominant $p$ orbital contribution. (b) The negligible $d$ orbital contribution. For clarity the orbitals of the same atoms are separated vertically, according to their contribution either to the $\sigma$-bands (bottom) or to the $\pi$ bands (top).

down the equations for $a_{\mu,mm'}$,

$$\begin{aligned}(\varepsilon-\varepsilon_p)\,a_{x,mm'} =\;& \mathrm{i}s_y\xi_p a_{z,mm'} \\ &+ t^{sp}(\varepsilon)\sum_n n_{n,x}\,a_{z,mm'n} + \tilde{t}(\varepsilon)\sum_{n,n'}\sum_{\nu=\{x,y\}} n_{n,x}n_{n,\nu}a_{\nu,mm'nn'}, \\ (\varepsilon-\varepsilon_p)\,a_{y,mm'} =\;& -\mathrm{i}s_x\xi_p a_{z,mm'} \\ &+ t^{sp}(\varepsilon)\sum_n n_{n,y}\,a_{z,mm'n} + \tilde{t}(\varepsilon)\sum_{n,n'}\sum_{\nu=\{x,y\}} n_{n,y}n_{n,\nu}a_{\nu,mm'nn'},\end{aligned} \tag{3.39}$$

where the quadruple index $mm'nn'$ counts all possible hopping paths of four steps along the connection lines of the carbon atoms. With four steps one ends up not only at the fourth-next neighbors but also at the second-nearest neighbors or at the initial atom itself. Taking every path into account by replacing $a_{mm'}$ in Eq. (3.38) and using the approximation $\varepsilon \approx \varepsilon_p$ with $\varepsilon-\varepsilon_p \ll \tilde{t}(\varepsilon_p)$ by defining $\tilde{t} = \tilde{t}(\varepsilon_p)$ and $t^{sp} = t^{sp}(\varepsilon_p)$, we derive the effective nnn hopping equation for $p_z$ orbitals,

$$\begin{aligned}(\varepsilon-\varepsilon_p)a_{z,0} = V_{pp\pi}\sum_m b_{z,m} -\; & t_{\mathrm{SO}}\sum_{m,m\neq m} a_{m,m'} \\ +\; & \mathrm{i}s_z t_{\mathrm{SO}}\frac{\sqrt{3}}{2}(-a_{z,12}+a_{z,13}+a_{z,21}-a_{z,23}-a_{z,31}+a_{z,32}) \\ +\; & it_{\mathrm{BR}}\sum_m \left[s_y n_{m,x} - s_x n_{m,y}\right] a_{z,m},\end{aligned} \tag{3.40}$$

where the corresponding effective clock-wise and anti-clock-wise nnn hopping paths are presented in Fig. 3.5. The sign of the nnn hopping is the same in the case of the $d$-orbital hopping, which is here due to double atomic SOC of the out-of-plane $p_z$ orbitals to the in-plane $p_x$ and $p_y$ orbitals. The corresponding on-site hopping changes the magnetic quantum number and at the same time flips the spin due to the conservation of angular momentum. Hence, there must be always two SOC couplings in the hopping paths such that the effective nnn hopping is of the same form as Eq. (3.29). The coupling of neighboring spin up and down states is represented by the last term on the right-hand side in the above equation. The corresponding effective nn hopping originates from the Stark effect and results in the additional term in the effective Hamiltonian,

$$\hat{H}_{\mathrm{BR}} = \mathrm{i}t_{\mathrm{BR}}\sum_{\langle i,j\rangle}\hat{a}_i(\vec{s}\times\vec{n})\hat{b}_j + \mathrm{h.c.}\,, \tag{3.41}$$

where j denotes the nearest neighbors of atom $i$ and orbital and spin indices are omitted. The corresponding effective hopping path is shown in Fig. 3.6(a),

where the coupling of $s$ and $p_z$ orbitals via the Stark effect interrupts the nnn hopping in Fig. 3.5 such that there is only one spin-flipping process due to on-site hopping on the neighboring atom. The effective hopping guarantees energy transfer from spin up to spin down states, which consequently causes the spin-splitting of the bands.[4] While the Fourier transformation of the creation and annihilation operators leads to the effective Hamiltonian of Eq. (3.7), where the effective spin-conserving nnn and the spin-flipping nn hopping parameters are associated with the intrinsic and the extrinsic, Bychov Rashba, parameters

$$t_{\mathrm{SO}} = \frac{9}{2}\lambda_{\mathrm{I}}^{(p)}, \quad t_{\mathrm{BR}} = \lambda_{\mathrm{R}}^{(p)}\,, \tag{3.42}$$

respectively, obtained at the K points. The shift of the Dirac points in energy corresponds to $\lambda_{\mathrm{I}}^{(p)}$ and is consistent with the results of the energy spectrum obtained in Ref. [23].

The derivation of the effective nn hopping through the $d$ orbitals with the path shown in Fig. 3.6(b) is not presented explicitly in this work. Thus let us present an argument for the shown path by ruling out the alternatives. Here the Stark effect couples the $p_z$ orbital to $d_{z^2}$. This leads to the question how to continue the path in order to generate an effective spin-flipping nn hopping. The $d_{z^2}$ orbitals does not couple to in-plane $p$ orbitals by hopping like $s$ orbitals and the hopping to the neighboring $p_z$ orbitals will not flip the spin. We can continue the path by hopping to the neighboring $d$ orbitals, but these do not couple to $p_z$ via SOC. Hence the only possible way to flip the spin is the on-site coupling to $d_{xz}$ or $d_{yz}$ via SOC, staying at the initial atom, followed by hopping to the neighboring $p_z$ orbitals. The coupling of the $d$ orbitals via SOC can be considered as on-site hopping between two states in a potential barrier. As we have pointed out in the previous section, such processes are unlikely, making the $d$ orbital contribution to the Bychkov Rashba effect negligible.

## 3.4 Effective spin-orbit coupling Hamiltonian

In this section we discuss the effective TB Hamiltonian from Eq. (3.7) in more detail. We have presented two ways to derive the intrinsic and extrinsic SOC terms, folding down the multi-orbitals TB Hamilton matrix given in the basis of on-site Bloch functions and considering effective spin-dependent hopping between the local atomic orbitals. The intrinsic SOC $H_{\mathrm{I}}$, given in Eq. (3.8), destroys the picture of relativistic particles by opening a band gap of $24\,\mu$eV at the Dirac cones and turns single-layer graphene into a quantum spin Hall insulator. The induced gap is twice the intrinsic SOC parameter $\lambda_{\mathrm{I}}$ in Eq. (3.10). The $p$-orbital contributions to $\lambda_{\mathrm{I}}$, derived in the previous sections and in the

[4] The spin-splitting of the bands is called Bychkov Rashba effect.

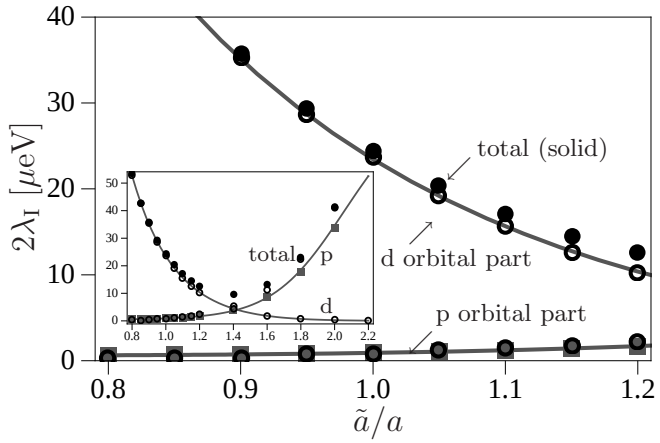


**Figure 3.7:** Results of the FP (circles), analytical (solid lines) and numerical (squares) TB calculations of the SOC intrinsic gap in graphene as a function of the artificial lattice constant ratio. Those dependences originate from the hopping parameters. The inset shows the dominance of the $p$ orbitals for larger values of the lattice constant ratio.

works [23, 45, 24], is negligible, yielding a gap of about 1 $\mu$eV, mainly due to the fact that the SOC of the $p$ orbitals, $\xi_p$, appears in the second order. The second, $d$ orbital, term in Eq. (3.10) gives a gap of 23 $\mu$eV, as obtained from FP [26]. This term dominates, mainly because the SOC of the $d$ orbitals, $\xi_d$, appears in the first order.

The extrinsic BRSOC $H_{\rm BR}$, given in Eq. (3.9), breaks the spin degeneracy of the bands in the vicinity of the K points, where the structure inversion asymmetry is given by the applied electric field. The contribution of the $p$ orbitals to the Bychkov Rashba parameter $\lambda_{\rm BR}$ in Eq. (3.11) has already been obtained in Ref. [23] by the degenerate perturbation theory. The linear dependence of the Bychkov-Rashba parameter on the electric field $E$ is consistent with our FP calculations [26]. But unlike the intrinsic SOC, the extrinsic contribution due to the $d$ orbitals in Eq. (3.11) is rather small because it is proportional to the product of two small quantities, $V_{pd\pi}/(\varepsilon_d - \varepsilon_p)$ and $\xi_d/(\varepsilon_d - \varepsilon_p)$. According to the FP calculations [26] $\lambda_{\rm BR} = 5$ $\mu$eV for a typical field of $E = 1$ V/nm. This is an order of magnitude smaller than the previous predictions by Huertas-Hernando *et al.* [45] of the value of 47 $\mu$eV and Min *et al.* [23] of 67 $\mu$eV. The contribution of $d$ orbitals to $\lambda_{\rm BR}$ is about 1.5%. Comparing the expressions for the Bychkov-Rashba parameter in Eq. (3.11) with FP calculation we obtain $eEz_{sp} \approx 15$ meV and the ratio $eEz_{pd}/(\varepsilon_d - \varepsilon_p) = 0.0003$, which confirms our necessary assumption for the Löwdin transformation and effective hopping approximations used in the derivation of Eqs. (3.11) and (3.41) To analyze the contribution from the

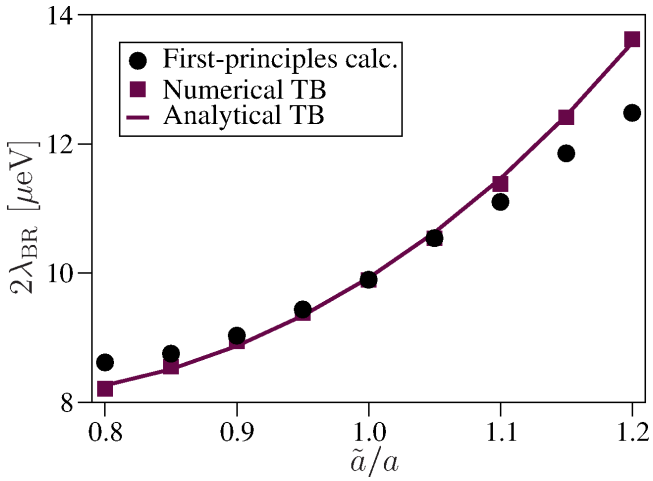


**Figure 3.8:** Calculated Bychkov-Rashba constant as a function of the artificial lattice constant ratio: FP calculations (circles), numerical diagonalization of the $p$ orbital part of TB Hamiltonian including overlap (squares) and the analytical calculations (solid line). Those dependences on the lattice constant arise from the hopping parameter $V_{sp\sigma}$.

$p$ and $d$ orbitals in more detail, let us focus on the dependence of the spin-orbit gap and the band splitting on the hopping parameters. In general the hopping parameters decrease with increasing inter-atomic distance [41]. The contribution to the gap from the $p$ orbitals is inversely proportional to the square of $V_{sp\sigma}$, whose dependence on the lattice constant is shown in Fig. 2.6, and thus should increase with increasing inter-atomic distance. In Fig. 3.7 we show the calculations of the intrinsic gap $2\lambda_{\mathrm{I}}$ and Fig. 3.8 shows the Bychkov Rashba parameter as a function of the relative lattice constant $\tilde{a}/a$ stretching. In the absence of $d$ orbitals, the gap increases exponentially and should approach the atomic-like splitting $\Delta = 3\xi_p \approx 8.5\,\mathrm{meV}$ of an isolated carbon atom. The $d$ orbital contribution is quadratically proportional to $V_{pd\pi}$ and thus should vanish for large $\tilde{a}/a$. The resulting decrease and further increase of the gap as the function of $\tilde{a}/a$ is due to the interplay between the contributions from both the $p$ and $d$ orbitals. The Bychov Rashba parameter $\lambda_{\mathrm{BR}}$ increases exponentially for realistic lattice constant stretching, which is controlled by the decay of the hopping parameter $V_{sp\sigma}$ with increasing inter-atomic distance.

The effective $8 \times 8$ Hamiltonian in Eq. (3.7) is easily diagonalized, yielding

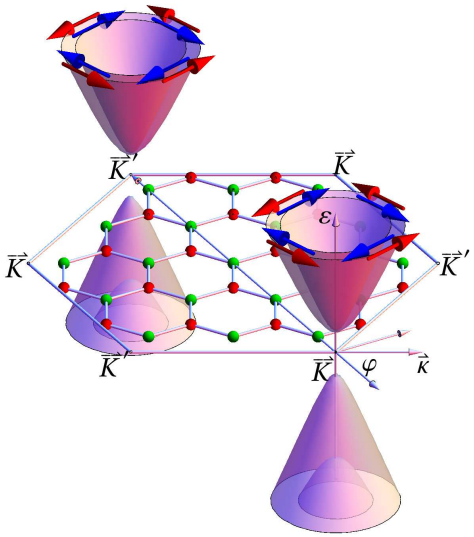


**Figure 3.9:** The split-off cones due to BRSOC. The spin alignment is shown by in-plane arrows for a fixed energy value.

the same eigenvalues at the K and K′ points,[5]

$$\varepsilon_{\zeta\vartheta} = \varepsilon_{\zeta\vartheta,\vec{\kappa}} = -\lambda_{\mathrm{I}} + \zeta\lambda_{\mathrm{BR}} + \vartheta\sqrt{(\lambda_{\mathrm{I}} - \zeta\lambda_{\mathrm{BR}})^2 + V_{pp\pi}^2|f|^2}, \tag{3.43}$$

where $f = f(\vec{\kappa}) \approx -\sqrt{3}/2\kappa a e^{-\mathrm{i}\varphi}$. The band index $\vartheta$ denotes the conduction ($\vartheta = +$) and valence bands ($\vartheta = -$), respectively. Both bands are split by BRSOC, where $\zeta = +$ denotes the band with higher energy and $\zeta = -$ with lower energy. The split bands are shown in Fig. 3.9 in the vicinity of the K and K′ points for an electric field of 1 V/nm. For this typical value of electric field the two conduction bands are degenerate and the valence bands are split by $2\lambda_{\mathrm{BR}}$. The band gap is reduced by BRSOC to $2(\lambda_{\mathrm{I}} - \lambda_{\mathrm{BR}})$, and disappear if both SOC parameters become equal by tuning the electric field. By further increasing the electric field, the band gap remains zero, but the spin-splitting of the conduction and valence bands increases. For $\kappa a > \lambda_{\mathrm{I}}/V_{pp\pi}$, in the case of linear energy dispersion,[6] the spin-splitting stays constant being $2\lambda_{\mathrm{BR}}$. In this region the spin states for a given wave-vector $\vec{\kappa}$ are well defined and align along to the vector $\vec{S}_{\zeta\vartheta}$, defined by the expectation value of the four dimensional spin

[5]The time inversion symmetry is conserved by SOC. The equivalent energy of the states in both valleys, K and K′, is a due to Kramer's degeneracy, $\varepsilon_{\vec{k},\uparrow} = \varepsilon_{-\vec{k},\downarrow}$, which is a consequence of the invariance of the system under time inversion.

[6]This condition usually fulfilled in gated or doped graphene.

operator vector $\vec{S}$, which is given by the tensor product $\hbar/2$ $(I \times \vec{s})$,

$$\vec{S}_{\zeta\vartheta} = \langle \tau, \zeta, \vartheta | \, \vec{S} \, | \tau, \zeta, \vartheta \rangle = \frac{2\zeta\varepsilon_{\zeta\vartheta} V_{pp\pi}}{N^2} \begin{pmatrix} \mathrm{i}(f^* - f) \\ f^* + f \\ 0 \end{pmatrix}, \tag{3.44}$$

with respect to the eigenstates of the effective Hamiltonian $H_{\mathrm{eff}}$,

$$\langle \sigma, s | +, \zeta, \vartheta \rangle = \frac{1}{N} \begin{pmatrix} -\mathrm{i}\zeta V_{pp\pi} f \\ \varepsilon_{\zeta\vartheta} \\ -\mathrm{i}\zeta\varepsilon_{\zeta\vartheta} \\ V_{pp\pi} f^* \end{pmatrix}, \quad \langle \sigma, s | -, \zeta, \vartheta \rangle = \frac{1}{N} \begin{pmatrix} i\zeta\varepsilon_{\zeta\vartheta} \\ -V_{pp\pi} f^* \\ -i\zeta V_{pp\pi} f \\ \varepsilon_{\zeta\vartheta} \end{pmatrix}. \tag{3.45}$$

The norm of the eigenvectors is given by $N = \sqrt{2}\sqrt{V_{pp\pi}^2 |f|^2 + \varepsilon_{\zeta\vartheta}^2}$. The eigenvectors are written in the basis $|\sigma, s\rangle = \{|A\uparrow\rangle, |A\downarrow\rangle, |B\uparrow\rangle, |B\downarrow\rangle\}$.

In the case of linear bands, the spin-alignment vector $\vec{S}_{\zeta\vartheta}$ lies in-plane and depends only on the polar angle $\varphi$ of the wave vector $\vec{\kappa}$, where

$$\vec{S}^{\zeta\vartheta} \approx \zeta\vartheta \begin{pmatrix} \sin\varphi \\ -\cos\varphi \\ 0 \end{pmatrix}, \tag{3.46}$$

such that the spin up and down states point always normal to the wave vector for both valleys, K and K′, as illustrated in Fig. 3.9. The spin-alignment vector is usually associated with an internal wave-vector magnetic field akin to the Bychkov-Rashba effect of the two-dimensional electron gas (2DEG) in semiconductor heterostructures, where the SOC term in the effective Hamiltonian has to be brought in the Zeeman form. The effective Hamiltonian of graphene, Eq. (3.7), can be transformed into an effective BR-type $2 \times 2$ Hamiltonian for both conduction and valence bands,

$$\tilde{H}_{\mathrm{eff}} = \vartheta(V_{pp\pi}|f| + \lambda_{\mathrm{I}}) + \vartheta\lambda_{\mathrm{BR}} \vec{S}^{\vartheta} \cdot \vec{s}, \tag{3.47}$$

by successive unitary rotation first into the basis of $H_0$ Eq. (2.30) and then into the spin basis with respect to the direction of the spin-alignment vector $\vec{S}^{\zeta\vartheta}$. Comparison with the original BR Hamiltonian in a 2DEG system of the form $H_{\vec{k}} = \hbar\omega(\vec{k}) \cdot \vec{s}/2$ shows that for SOC in graphene the effective in-plane magnetic field is of constant amplitude but dependent on the direction of the wave-vector $\vec{\kappa}$. In this effective field the spin precesses with a frequency of $\Omega = 2\lambda_{\mathrm{BR}}/\hbar$. As shown by D'yakonov and Perel [46] random scattering induces motional narrowing [47] of this spin precession causing spin relaxation. The

spin relaxation rates for the D'yakonov - Perel mechanism for the outer-plane and in-plane spin components,

$$\frac{1}{\tau_{s,z}} = \tau_p \left(\frac{2\lambda_{\mathrm{BR}}}{\hbar}\right)^2, \quad \frac{1}{\tau_{s,x}} = \frac{1}{\tau_{s,y}} = \frac{\tau_p}{2} \left(\frac{2\lambda_{\mathrm{BR}}}{\hbar}\right)^2, \tag{3.48}$$

are asymmetric due to the in-plane magnetic field and depend on the momentum relaxation rate $1/\tau_p$, which coincides in graphene with the correlation time of the randomized effective magnetic field by scattering events [47]. Applying different electron-scattering mechanisms, we obtained the spin relaxation times in graphene, being of the order of micro-seconds [19] at room temperature and for realistic values of $\lambda_{\mathrm{BR}}$ and densities of charged impurities, which are always present in graphene substrates. The surprisingly small experimental value of the spin relaxation times (100-200 ps) was only reproduced assuming untypical large values for the impurity density. In Ref. [19] we pointed out that origin for such small relaxation times in the experiment could be ad-atoms with relative large atomic SOC. Placed on graphene the ad-atoms could induce a large extrinsic SOC of the order of meV locally and consequently large spin relaxation rates.

## 3.5 Conclusion of the chapter

An effective Hamiltonian for the SOC effects in graphene was derived from a multi-orbital TB model considering $s$, $p$, and $d$ orbitals. Since $d$ orbitals contribute to the $\pi$ band without SOC, their (atomic) spin-orbit splitting determines the value of the band gap at the K(K′) points. The constant spin-splitting of the conduction and valence bands is due to the coupling of $s$ and $p$ orbitals by the Stark effect and the atomic spin-orbit interaction. This facts have been independently confirmed by performing FP calculations of the dependence of the gap and band spin-splitting on the lattice constant. We have also derived an effective single-orbital hopping Hamiltonian that captures all the essential spin-orbit physics of itinerant electrons in graphene. With the parameters derived from the multi-orbital theory and the insight given by showing the relevant effective hopping paths, such a model should be useful for spin-polarized transport investigations, within the limitations restricting its use close to the K(K′) points. We have pointed out, that the spin-splitting of the bands can be interpreted as a Zeeman-like splitting in the internal wave-vector dependent magnetic field. The scattering of the electrons randomizes the internal field leading to spin relaxation. However, the experimental values of hundreds of picoseconds would require SO constants orders of magnitude higher than the ones obtained by FP calculations [19].

# 4 Tight binding description of few-layer graphenes

## 4.1 Introduction to the chapter

In this chapter we address the open questions considering SOC in bilayer and trilayer graphenes: How does the SOC change the band structure? How big are the corresponding effects? What mechanism stands behind? In chapter 2 we have shown that in the single-layer coupling of the $d$-orbital character of the Bloch state by the $\mathbf{L} \cdot \mathbf{S}$ term gives rise to the leading term of in the SOC induced band gap being $24\,\mu$eV. We found that in such few layer graphenes (FLGs) the $\pi$ bands at the Fermi energy involve intrinsic SOC effects of the same order ($24\,\mu$eV) and became significantly suppressed below the numerical tolerance if the $d$ orbitals are excluded from the calculations. This coincidence with the SOC induced band gap in single-layer graphene implies that the SOC effects in FLGs have the same physical origin. More precisely, the intrinsic SOC effect of the single layer determinates the SOC effects in the bilayer, trilayer or even more-layer graphenes and graphite.

The correspondence between single and FLG vanishes when considering the extrinsic SOC effects. The spin-splitting of the $\pi$-bands in the vicinity of the K point is due to transitions between spin-up and spin-down states. These additional effects appear due to breaking of the spatial inversion symmetry. In bilayer graphene and as well as ABC stacked trilayer the spatial inversion symmetry is broken by applying an external electric field perpendicular to the layers. The structure of the ABA stacked trilayer graphene is not inversion symmetric by itself. The spin-splittings at the K points in all structures are only due to the intra-layer intrinsic SOC effect. For a finite wave vectors k with respect to the K point there is a competition of the intra-layer intrinsic SOC, intra-layer extrinsic, BRSOC, and inter-layer extrinsic SOC effect. The extrinsic SOC effects have a minor influence on the electronic structure in the very vicinity of the K points and become insubstantial in comparison to the intrinsic SOC effect, which leads to the extrinsic spin splittings due to an interplay of the inter-layer hopping and the electrostatic potential arising between the layers. With increasing values of k the effect of intrinsic SOC decreases, and the intra-layer, BRSOC, dominates the spin splittings of the $\pi$ bands. The inter-layer extrinsic

SOC effects give a small contribution to the spin splitting by inducing small asymmetry in the values of splitting of the conduction and valence bands.

Here we present an orthogonal TB model for bilayer and trilayer graphene taking into account $s$, $p$, and $d$ orbitals. The SOC effects are modeled by effective Hamiltonians, which include only the intra-layer effects. The hopping parameters have been obtained by fitting relevant band structure obtained by FP calculation to the TB model. The electronic structures of bilayer graphene and graphite are obtained with the Wien2k code citeBlaha:Wien2k and trilayer with FLEUR code within the film mode [48] by Dr. Martin Gmitra. In the FP calculations we consider 0.142 nm for intra-layer atomic distance and inter-layer distance was set to 0.335 nm, In the Wien2k we use vacuum of 2 nm for bilayer graphene.

This chapter is organized as follows. We present first a TB model for a general $N$-layer graphene including SOC effectively. This model is discussed in detail for bilayer and trilayer graphene, and graphite. Further, we show. that the band structures obtained in the vicinity of the K point from the TB model agree well with the results of the FP calculations. The TB Hamiltonians are presented explicitly, where the Bychkov-Rashba SOC in bilayer graphene is discussed using an effective two-band model for the low-energy bands.

## 4.2 Tight-binding model of few-layers graphenes

The band structure of graphite and FLG is well described by a TBA or by so-called Slonczewski-Weiss-McClure (SWMcC) model[28, 49, 50, 51, 52, 53, 3, 54, 4, 55]. In the TB approach one considers the inter- and intra-layer hopping between the $p_z$-orbitals of the neighboring atoms. The hopping parameters are given by a set of parameters $\{\gamma_0, \ldots, \gamma_6\}$ shown in Fig. 4.1, where $\gamma_0$ and $\gamma_1$ are the nearest neighbor intra-layer and inter-layer hopping, $\gamma_3$ and $\gamma_4$ are indirect hopping between neighboring layers and finally $\gamma_2$, $\gamma_5$, and $\gamma_6$ correspond to the direct second-nearest-neighbor inter-layer hopping. In addition, there are $\Delta$, $\delta$ parameters, which handle the asymmetries in the energy shifts of the corresponding bonding and anti-bonding states in the energy spectrum. The role of these parameters to the band structure and the correspondence between TB and SWMcC Hamiltonian matrices is given in Ref. [4]. The relation of the TB and SWMcC parameters and the corresponding values are tabulated in Tab. 4.1 for the FLGs and graphite. In the FLGs the individual graphene layers can be ordered in different ways concerning the relative positions of the sublattices $\mathrm{A}_i$ and $\mathrm{B}_i$ of the $i$-th layer. The resulting energy spectra and physical properties strongly depend on the ordering. In the so-called Bernal or graphite structure, the even numbered layers (let say B) are shifted along a chosen nearest neighbor direction by the lattice constant. Even number layered FLG has spatial inversion

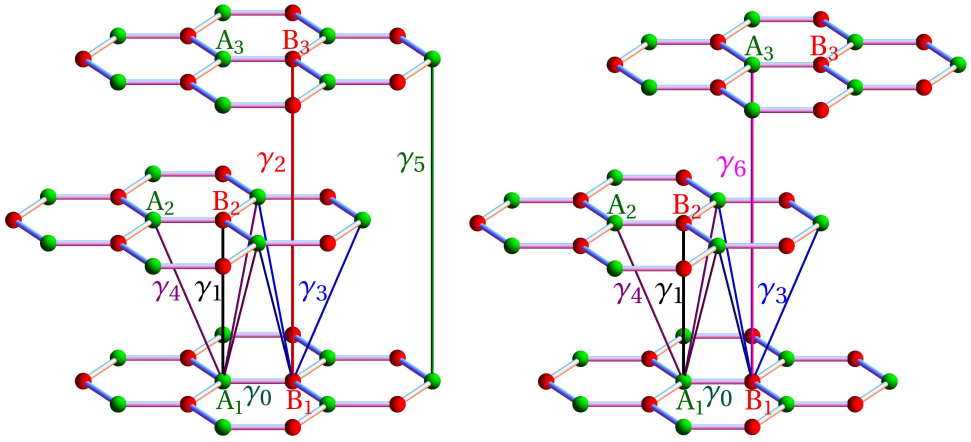


**Figure 4.1:** Sketch of the trilayer graphene in (a) ABA stacking and (b) ABC stacking. The bilayer graphene structure is obtained by removing the top layer. The filled circles represent the carbon atoms of the sublattice A (green) and B (red). The hopping parameters ($\gamma_0, \gamma_1, \gamma_2, \gamma_3, \gamma_4, \gamma_5$ and $\gamma_6$) are denoted by the short-dashed, dashed, long-dashed, dashed-dotted, dotted, long-dashed-dotted and finally by the small-dotted lines, respectively.

symmetry, while odd number layered FLG has no spatial inversion symmetry. When one takes ABA trilayer graphene, shown in Fig. 4.1(a), and shifts one of the A layer in the same direction as the B layer with respect to second A layer, one obtains ABC trilayer structure possessing the spatial inversion symmetry, see Fig. 4.1(b). These two ways of stacking correspond to the most dense sphere packing in the hexagonal structure, minimize total energy, and are of interest in this thesis.

Within a TB model the different ways of stacking are reflected in the second-nearest-neighbor inter-layer hopping. For the ABC stacking we introduce the parameter $\gamma_6$, which describes the inter-layer hopping between two atoms in different triangular sublattices A and B on layers A and C. In general, $\gamma_6$ has a different value from the parameter $\gamma_2$, which describes the hopping between atoms of the sublattice B in the ABA stacking structure. The values for $\gamma_1$, $\gamma_2$, $\gamma_5$, $\gamma_6$, and the asymmetry parameters $\Delta$, $\delta$(ABA), and $\delta$(ABC) are obtained by comparing the eigenvalues of the effective Hamiltonians, shown in the following section, to the FP spectra at the K point. The hopping parameters $\gamma_0$, $\gamma_3$, $\gamma_4$ are chosen to reproduce the band-structure obtained from FP calculations close to the K point. The corresponding values are listed in Tab. 4.1.

The spinless band structure of the $N$-layer FLGs is described by the $2N$-

| TB [eV] | $\Delta$ | $\delta$ | $\gamma_0$ | $\gamma_1$ | $\gamma_2$; $\gamma_6$ | $\gamma_3$ | $\gamma_4$ | $\gamma_5$ |
|---|---|---|---|---|---|---|---|---|
| SWMcC [eV] | $\Delta - \gamma_2 + \gamma_5$ | - | $\gamma_0$ | $\gamma_1$ | $\gamma_2/2$ | $\gamma_3$ | $-\gamma_4/2$ | $\gamma_5/2$ |
| bilayer | 0.0096 | - | 2.60 | 0.339 | - | 0.290 | -0.143 | - |
| trilayer ABA | 0.0153 | 0.008 | 2.60 | 0.337 | -0.0210 | 0.280 | -0.140 | 0.0080 |
| trilayer ABC | 0.0077 | -0.001 | 2.58 | 0.335 | 0.0073 | 0.251 | -0.152 | - |
| graphite | 0.0198 | - | 2.60 | 0.336 | -0.0082 | 0.275 | -0.140 | 0.0114 |

**Table 4.1:** Tight-binding parameters obtained by fitting the band structure to the FP calculations. The signs of the parameters are chosen to be consistent with the SWMcC parameterization presented in Ref. [2]. The translation table of the parameters in the TB and SWMcC models is obtained from band-structure fitting of graphite. The presented values of the TB parameters are of the same order as in the literature [3, 4, 5, 6] and are consistent with values of Ref. [7] obtained from bilayer band-structure calculation using WIEN2k code.

dimensional TB Hamilton matrix, whose short notation with $\{i,j\} = \{1,\ldots,N\}$,

$$H^0_{i,j}\delta_{i,j} + H^1_{i,j}\delta_{i,j+1} + H^2_{i,j}\delta_{i,j+2} + \text{h.c.}\,,$$

contains the intra-layer $H^0_{i,j}$, first-nearest-neighbor inter-layer $H^1_{i,j}$ and the second-nearest-neighbor inter-layer $H^2_{i,j}$ hopping matrices, which are given in the basis of the sublattice pseudospin. Here the 'up' state corresponds to electron density localized at sublattice A and the 'down' state at sublattice B. With the spin degree of freedom the dimension of the TB Hamiltonian increases to $4N$. The $\pi$ bands wave functions of FLGs built by $p_z$ orbitals are not affected by the spin-orbit $\mathbf{L}\cdot\mathbf{S}$ term. Therefore coupling the $\pi$ bands to the other states is needed by introducing a multi-orbital model that increases the dimension of the TB Hamiltonian. Since SOC contributions are rather small due to the light atomic mass of carbon, the effects of SOC can be studied in form of an effective TB Hamiltonian. The effective TB Hamiltonian can be obtained using the Löwdin transformation (see Sec. 3.2) of the multi-orbital TB Hamiltonian, which includes the $s$, $p$, and $d$ orbitals. The most simple model neglects inter-layer hopping except between the $p_z$ orbitals, while all other intra-layer hopping between $s$, $p$ and $d$ orbitals are taken into account. The $\pi$ bands are then expressed in a basis reflecting contributions from other orbitals. It means, that there are new terms in the matrix elements of $H^0_{i,j}$, which correspond to the single-layer intrinsic and extrinsic SOC effects in Eqs. (3.10) and (3.11), respectively. The technical details of the TB Hamiltonians are given below. In the following sections we describe the electronic states in bilayer and ABC trilayer graphene in the presence of SOC and normal electric field, and ABA trilayer graphene and graphite including SOC only. The FP results are presented and explained using the TB concepts.

## 4.3 Hamiltonians

### 4.3.1 Bilayer graphene Hamiltonian

The effective TB Hamiltonian of a bilayer graphene shown below includes the single-layer intrinsic and *extrinsic*, BRSOC, effects given by the parameters $\lambda_{\mathrm{I}}$ and $\lambda_{\mathrm{BR}}$, respectively. We write the TB Hamilton matrices in the basis of the on-site Bloch functions $\Psi_{\mathrm{A}_1,s}, \Psi_{\mathrm{B}_1,s}, \Psi_{\mathrm{A}_2,s}, \Psi_{\mathrm{B}_2,s}$, where $s$ denotes the spin eigenstates along the electric field, and obtain the effective Hamiltonian

$$\begin{pmatrix} \Delta + \tau\lambda_{\mathrm{I}}s_z + V/2 & \gamma_0 f + i\lambda_{\mathrm{BR}}s^\tau_- & \gamma_4 f^* & \gamma_1 \\ \gamma_0 f^* - i\lambda_{\mathrm{BR}}s^\tau_+ & -\tau\lambda_{\mathrm{I}}s_z + V/2 & \gamma_3 f & \gamma_4 f^* \\ \gamma_4 f & \gamma_3 f^* & \tau\lambda_{\mathrm{I}}s_z - V/2 & \gamma_0 f + i\lambda_{\mathrm{BR}}s^\tau_- \\ \gamma_1 & \gamma_4 f & \gamma_0 f^* - i\lambda_{\mathrm{BR}}s^\tau_+ & \Delta - \tau\lambda_{\mathrm{I}}s_z - V/2 \end{pmatrix} \quad (4.1)$$

The matrices $s_{\pm}^{\tau} = s_x \pm i\tau s_y$ are given by the Pauli-matrices, where the eigenstates of $s_z$ represent the spin eigenstates and $\tau = \pm 1$ counts the K and K′ points, respectively. The intra-layer $\gamma_0$ and indirect inter-layer hopping $\gamma_3$ and $\gamma_4$ imply the wave-vector dependence of the Hamiltonian, which is hidden in the variable $f \approx -\tau\sqrt{3}|\vec{k}|ae^{-i\tau\varphi}/2$ defined in Eq. (2.26), where $\vec{k} \to \vec{k} - \vec{K}(\vec{K}')$, $\varphi = \angle(\vec{k}, \vec{K})$, $\vec{K}(\vec{K}') = (\pm 4\pi/(3a), 0)$, and $a = 0.246\,\mathrm{nm}$ is the graphene lattice constant.

To fold down the effective TB Hamiltonian into the basis of the low-energy states, we transform the Hamilton matrix in the basis $\Psi_{\mathrm{B}_1,s}, \Psi_{\mathrm{A}_2,s}, \Psi_{\mathrm{A}_1,s}, \Psi_{\mathrm{B}_2,s}$ to gather the low-energy and high-energy states,

$$\begin{pmatrix} -\tau\lambda_{\mathrm{I}}s_z + V/2 & \gamma_3 f & \gamma_0 f^* - i\lambda_{\mathrm{BR}}s_+^{\tau} & \gamma_4 f^* \\ \gamma_3 f^* & \tau\lambda_{\mathrm{I}}s_z - V/2 & \gamma_4 f & \gamma_0 f + i\lambda_{\mathrm{BR}}s_-^{\tau} \\ \gamma_0 f + i\lambda_{\mathrm{BR}}s_-^{\tau} & \gamma_4 f^* & \Delta + \tau\lambda_{\mathrm{I}}s_z + V/2 & \gamma_1 \\ \gamma_4 f & \gamma_0 f^* - i\lambda_{\mathrm{BR}}s_+^{\tau} & \gamma_1 & \Delta - \tau\lambda_{\mathrm{I}}s_z - V/2 \end{pmatrix} \quad (4.2)$$

For small enough $f$ and $\lambda_{\mathrm{BR}}$ the requirements of the Löwdin transformation is satisfied and the folding down results in the effective two-band Hamiltonian given in the basis of low-energy on-site spin-resolved wave functions,

$$\begin{aligned} \langle B,1|\,\hat{H}\,|B,1\rangle &= \begin{pmatrix} (2\Delta - V)\zeta|f|^2 - \tau\lambda_{\mathrm{I}} + V/2 & -2i\lambda_{\mathrm{BR}} f\zeta(2\Delta - V)/\gamma_0 \\ i\lambda_{\mathrm{BR}} f^*\zeta(2\Delta - V)/\gamma_0 & (2\Delta - V)\zeta|f|^2 + \tau\lambda_{\mathrm{I}} + V/2 \end{pmatrix}, \\ \langle A,2|\,\hat{H}\,|A,2\rangle &= \begin{pmatrix} (2\Delta + V)\zeta|f|^2 + \tau\lambda_{\mathrm{I}} - V/2 & -2i\lambda_{\mathrm{BR}} f\zeta(2\Delta + V)/\gamma_0 \\ 2\mathrm{i}\lambda_{\mathrm{BR}} f^*\zeta(2\Delta + V)/\gamma_0 & (2\Delta + V)\zeta|f|^2 - \tau\lambda_{\mathrm{I}} - V/2 \end{pmatrix}, \\ \langle B,1|\,\hat{H}\,|A,2\rangle &= \begin{pmatrix} \gamma_3 f - 4\gamma_1 (f^*)^2\zeta & 8i\lambda_{\mathrm{BR}} f^*\zeta\,\gamma_1/\gamma_0 \\ 0 & \gamma_3 f - 4\gamma_1 (f^*)^2\zeta \end{pmatrix}, \end{aligned} \quad (4.3)$$

where $\zeta = \gamma_0^2/(V^2 + 4(\gamma_1^2 - \Delta^2))$ and the high-energy bands give a small pertubative contribution to the shape of the low-energy bands. For reasonable values of $V$ holds $|V \pm 2\Delta| \ll \gamma_0$, therefore the corresponding matrix elements can be set to zero.

### 4.3.2 Trilayer graphenes Hamiltonians

The effective TB Hamiltonians of ABA and ABC trilayer graphenes shown below including the intra-layer SOC effects,

$$H_{\text{eff}} = \begin{pmatrix} \Delta + \tau\lambda_{\text{I}} s_z & \gamma_0 f & \gamma_4 f^* & \gamma_1 & \gamma_5 & 0 \\ \gamma_0 f^* & \delta - \tau\lambda_{\text{I}} s_z & \gamma_3 f & \gamma_4 f^* & 0 & \gamma_2 \\ \gamma_4 f & \gamma_3 f^* & \tau\lambda_{\text{I}} s_z & \gamma_0 f & \gamma_4 f & \gamma_3 f^* \\ \gamma_1 & \gamma_4 f & \gamma_0 f^* & \Delta - \tau\lambda_{\text{I}} s_z & \gamma_1 & \gamma_4 f \\ \gamma_5 & 0 & \gamma_4 f^* & \gamma_1 & \Delta + \tau\lambda_{\text{I}} s_z & \gamma_0 f \\ 0 & \gamma_2 & \gamma_3 f & \gamma_4 f^* & \gamma_0 f^* & \delta - \tau\lambda_{\text{I}} s_z \end{pmatrix}, \tag{4.4}$$

$$\begin{aligned} H_{\text{eff}} = & \begin{pmatrix} \Delta + V & \gamma_0 f & \gamma_4 f^* & \gamma_1 & 0 & 0 \\ \gamma_0 f^* & \delta + V & \gamma_3 f & \gamma_4 f^* & \gamma_6 & 0 \\ \gamma_4 f & \gamma_3 f^* & \Delta + V_m & \gamma_0 f & \gamma_4 f^* & \gamma_1 \\ \gamma_1 & \gamma_4 f & \gamma_0 f^* & \Delta + V_m & \gamma_3 f & \gamma_4 f^* \\ 0 & \gamma_6 & \gamma_4 f & \gamma_3 f^* & \delta - V & \gamma_0 f \\ 0 & 0 & \gamma_1 & \gamma_4 f & \gamma_0 f^* & \Delta - V \end{pmatrix} + \\ & + \begin{pmatrix} \tau\lambda_{\text{I}} s_z & i\lambda_{\text{BR}} s_-^\tau & 0 & 0 & 0 & 0 \\ -i\lambda_{\text{BR}} s_+^\tau & -\tau\lambda_{\text{I}} s_z + V & 0 & 0 & 0 & 0 \\ 0 & 0 & \tau\lambda_{\text{I}} s_z & +i\lambda_{\text{BR}} s_-^\tau & 0 & 0 \\ 0 & 0 & -i\lambda_{\text{BR}} s_+^\tau & -\tau\lambda_{\text{I}} s_z + V_m & 0 & 0 \\ 0 & 0 & 0 & 0 & \tau\lambda_{\text{I}} s_z & i\lambda_{\text{BR}} s_-^\tau \\ 0 & 0 & 0 & 0 & -i\lambda_{\text{BR}} s_+^\tau & -\tau\lambda_{\text{I}} s_z \end{pmatrix}, \end{aligned} \tag{4.5}$$

respectively. The Hamilton matrices are written in the basis of the on-site wave functions $\Psi_{\text{A}_1,s}, \Psi_{\text{B}_1,s}, \Psi_{\text{A}_2,s}, \Psi_{\text{B}_2,s}, \Psi_{\text{A}_3,s}, \Psi_{\text{B}_3,s}$. In the ABC trilayer graphene the middle layer has in general a non-zero potential $V_m$ due to screening effects. Here we can use the same arguments as in the case of the bilayer graphene to neglect the Bychkov-Rashba effect in the very vicinity of the K points.

## 4.4 Bilayer graphene

The electronic structure of bilayer graphene around the K point, unlike the single layer graphene, does not exhibit massless particles. The bands are parabolic, but the possibility of a widely tunable band gap using electric field perpendicular to the layers shows fascinating behavior that opens promising prospects in applications [56, 57, 7]. In conventional materials, the band gap is fixed by the crystalline structure, preventing the band gap control, which does not

allow further control of transport and optical properties. Spintronics applications, however, require spin manipulation in which SOC plays a significant role [58, 22]. It has been recently proposed that the effects of SOC in bilayer and trilayer graphene structures are at the order of hundreds of micro eV caused by effective spin-dependent inter-layer hopping between $p$ orbitals [35, 36]. Our study presented here does not support such results.

Figure 4.2 shows the calculated band structure of bilayer graphene around the K point along the ΓKM high-symmetry lines; the SOC is taken into account. The excellent agreement between the TB model and the FP calculations (lines and points), respectively, persists to the lowest energy scales. Each of the shown scales uncovers different physics. The largest scale in Fig. 4.2(a) shows parabolic dispersions of four spin-degenerate $\pi$ bands due to spatial inversion symmetry. The high-energy bands (corresponding to orbitals at atoms $A_1$ and $B_2$ at the K point, see Fig. 4.1) are shifted in energy about 340 meV by the direct inter-layer hopping $\gamma_1$ away from the low-energy bands (atoms $A_2$ and $B_1$) lying close to the Fermi level. The difference in the energy shifts between the conduction and valence bands is taken into account by the parameter $\Delta$. The fine structure of the low-energy bands in Fig. 4.2(b) shows two overlaying parabolas crossing at the K point as well as at the point of accidental crossing along the ΓK line. These crossings are governed by the indirect inter-layer hopping $\gamma_3$ and $\gamma_4$ which push the bands towards each other. The presence of the SOC separates the states at the crossing points by the value of 24 $\mu$eV, see Fig. 4.2(c), which collapses below 1 $\mu$eV if $d$ orbitals are not considered in the calculations.

Applying a transverse external electric field $E$ to the bilayer places the layers to a different electrostatic potential. In terms of the TB model one introduces parameter $V$ which includes all possible screening effects and corresponds to the splitting of the low-energy bands at the K point [7]. Figure 4.3(a) shows $V$ as a function of the electric field by fitting to the electronic structure obtained from the FP calculations. The dependence is nearly linear with the slope of about 0.1 eV/ (V/nm). The electric field bears also a slight variation of $\Delta$ and direct inter-layer hopping $\gamma_1$. Their dependences are shown in Figs 4.3(b) and 4.3(d). For tiny electric fields smaller then 6 mV/nm, bilayer graphene keeps its semi-metallic property, which is given by a finite Fermi surface in the triangular-warping structure of the low-energy bands even though the electric field induces small energy gaps at the crossing points of the overlapping parabolas. Further increase in electric field opens indirect band gap between the maximum of the valence band present at the KΓ line and the minimum of the conduction band at the K point; see band structure for the field of 25 mV/nm shown in Fig. 4.4(b). For electric fields larger then 0.45 V/nm the states at the K point get significantly repelled; minima and maxima of the valence and conduction bands are then present along ΓK and KM lines [59, 7]. Consequently, there is a direct band gap, shown in Figs 4.5(b) and 4.6(b). Due to the shift of the conduction band

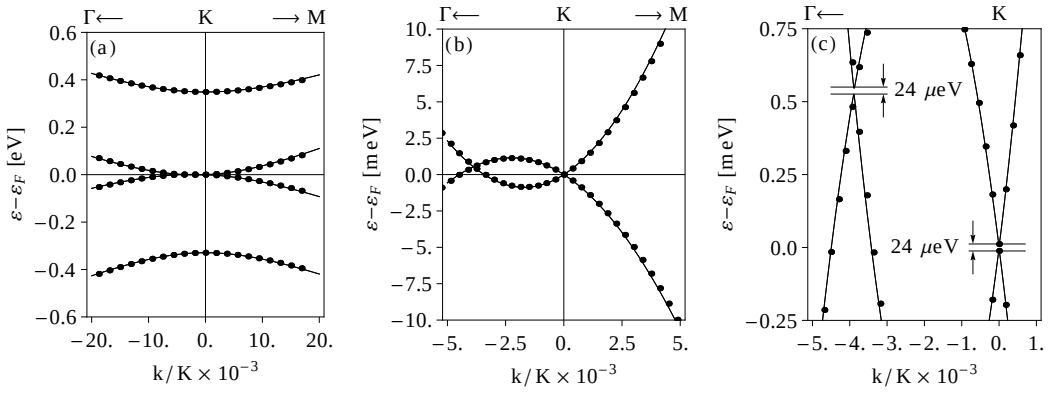


**Figure 4.2:** The calculated band structure of the $\pi$ bands along the ΓKM lines, where $\mathrm{K} = |\Gamma\mathrm{K}| = 4\pi/(3a)$ with $a = 0.246\,\mathrm{nm}$. First-principles results are shown by circles while TB calculations as solid lines. (a) Low and high-energy bands. (b) Fine structure of the low-energy bands. (c) Detail view at the low-energy bands shows anti-crossings at the K point and at $k = -0.063\,\mathrm{nm}^{-1}$.

minimum away from the K point, the bandgap is no longer proportional to the potential $V$ and saturates to a value of about 265 meV, similar to the values found in previous works [60, 61, 57], as it is shown in Fig. 4.3(c). The electric field breaks spatial inversion symmetry and lifts spin degeneracy. Closer look at the band structure along the KΓM lines for $E = 25\,\mathrm{mV/nm}$, $E = 1\,\mathrm{V/nm}$, and $E = 10\,\mathrm{V/nm}$ shown in Figs 4.4(c), 4.5(c), and 4.6(c), respectively, illustrates the low-energy conduction-band spin splitting, which is exclusively governed by the $d$ orbitals, and is of the order of $24\,\mu$eV at the K point. The values of the corresponding TB parameters are presented in Tab. 4.2 .

The SOC effects at the K point can be understood in terms of the interplay between the electrostatic potential $V$, direct inter-layer hopping $\gamma_1$, and intrinsic intra-layer SOC controlled by the parameter $\lambda_\mathrm{I}$, which has been found for graphene $2\lambda_\mathrm{I} = 24.4\,\mu$eV [26, 62]. The energy spectrum at the K point reads

$$\begin{aligned}
\varepsilon_1^{\uparrow} &= \Delta + \sqrt{\gamma_1^2 + (V/2 + \lambda_\mathrm{I})^2}, \quad \varepsilon_2^{\uparrow} = V/2 - \lambda_\mathrm{I}, \\
\varepsilon_1^{\downarrow} &= \Delta + \sqrt{\gamma_1^2 + (V/2 - \lambda_\mathrm{I})^2}, \quad \varepsilon_2^{\downarrow} = V/2 + \lambda_\mathrm{I}, \\
\varepsilon_4^{\uparrow} &= \Delta - \sqrt{\gamma_1^2 + (V/2 + \lambda_\mathrm{I})^2}, \quad \varepsilon_3^{\uparrow} = -V/2 + \lambda_\mathrm{I}, \\
\varepsilon_4^{\downarrow} &= \Delta - \sqrt{\gamma_1^2 + (V/2 - \lambda_\mathrm{I})^2}, \quad \varepsilon_3^{\downarrow} = -V/2 - \lambda_\mathrm{I}.
\end{aligned} \tag{4.6}$$

The sketch of the spectrum is shown in the Fig. 4.7. The eigenstates are constructed by the on-site (Bloch) wave-functions. Their form at the K point was

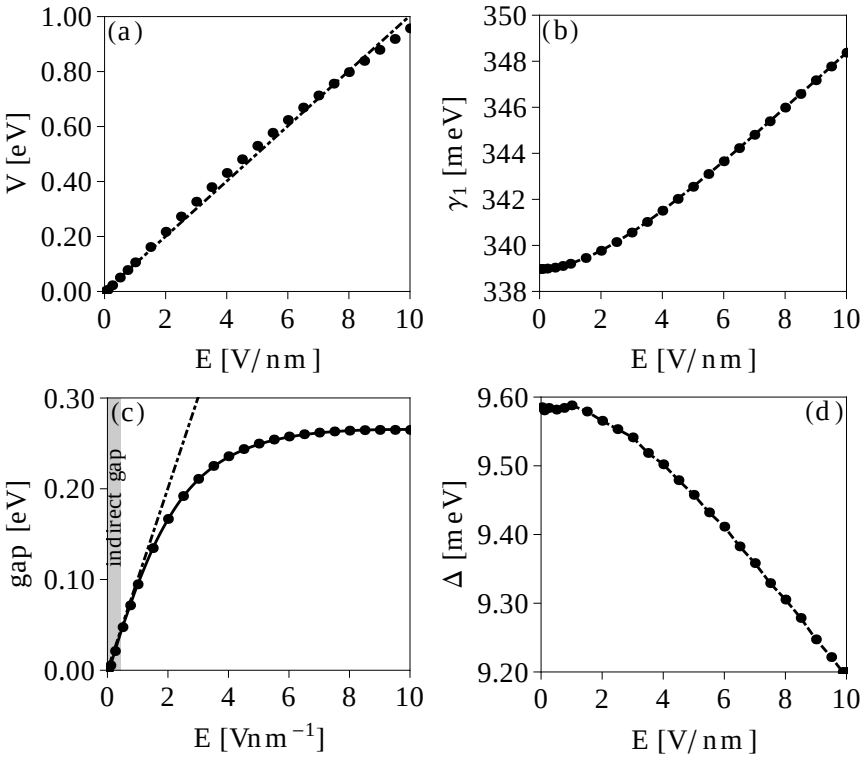


**Figure 4.3:** Bilayer graphene essentials in external electric field obtained from FP calculations (circles) and TB model (solid line). (a) Electrostatic potential $V$ as a function of the applied electric field. The slope is described by the effective inter-layer distance of $d_{\text{eff}} = 0.1$ nm, which is defined by $V = eEd_{\text{eff}}$; and (b) corresponding dependence of the hopping parameter $\gamma_1$. (c) Energy gap in biased bilayer graphene in comparison to $V$ (dashed-dotted line) as a function of the electric field. (d) Decrease of the parameter $\Delta$ due to the electric field. We note that $E$ is the actual external electric field and not the screened one as presented in Ref. [7].

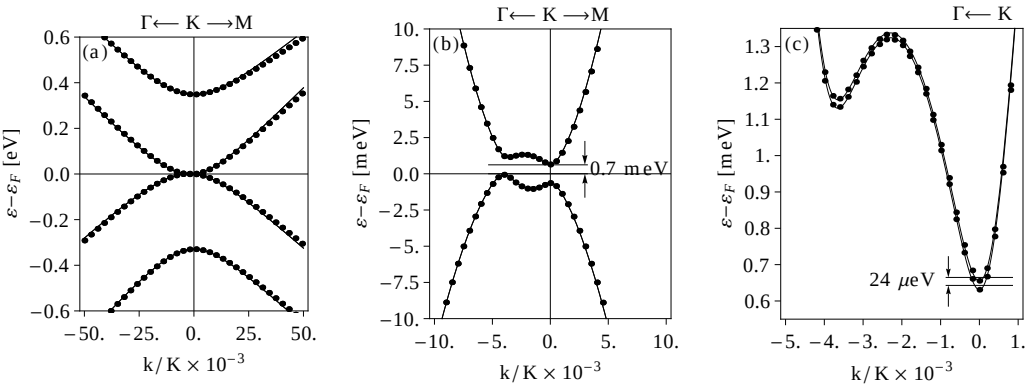


**Figure 4.4:** The calculated band structure of the $\pi$ bands of the bilayer graphene with the applied electric field of 25 mV/nm along the ΓKM line with the K point and Fermi energy at origin, where $\mathrm{K} = |\Gamma\mathrm{K}| = 4\pi/(3a)$ with $a = 0.246\,\mathrm{nm}$. Circles show the results of FP and lines are the TB calculations. (a) Low and high-energy bands. (b) The fine structure of the low-energy bands with the corresponding indirect band gap of 0.7 meV between $k = -0.068\ \mathrm{nm}^{-1}$ and the K point. (c) Detail view at the low-energy conduction band shows its splitting due to SOC with the maximum value of $2\lambda_\mathrm{I} = 24\,\mu\mathrm{eV}$ at the K point and at $k = -0.063\ \mathrm{nm}^{-1}$.

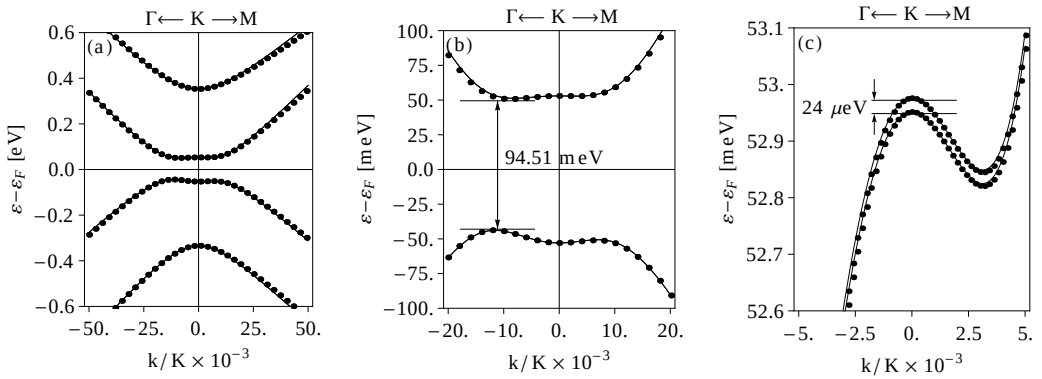


**Figure 4.5:** The calculated band structure of the $\pi$ bands with the applied electric field of 1 V/nm. Circles show the results of FP and lines are the TB calculations. (a) All bands: envolving band gap. (b) Detail view at the low-energy bands shows the mostly direct bandgap of 94.5 meV between the valence $k = -0.2$ nm$^{-1}$ and the conduction $k = -0.15$ nm$^{-1}$ bands. (c) More detail view at the low-energy-conduction band shows its splitting due to SOC with the maximum value of $2\lambda_{\mathrm{I}} = 24\,\mu$eV at the K point and in its vicinity, for the k points, whose values are the interval $[-0.17, 0.1]$ nm$^{-1}$.

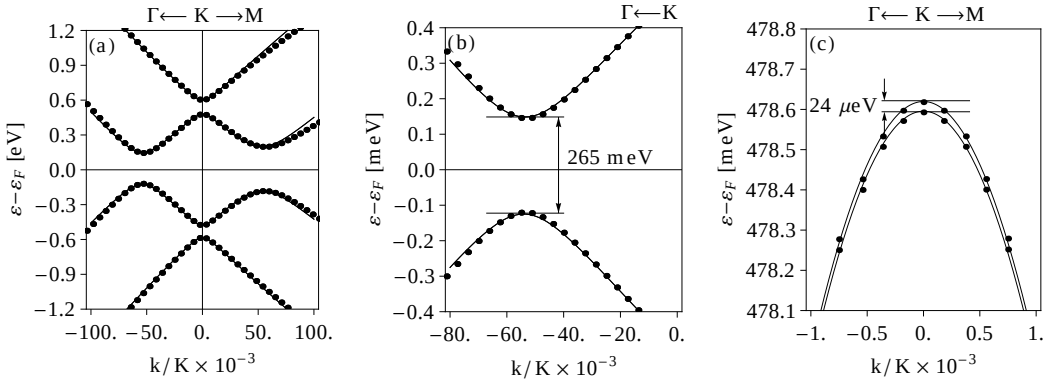


**Figure 4.6:** The calculated band structure of the $\pi$ bands with the applied electric field 10 V/nm. (a) Hyperbolic high-energy bands and Maxican-hat structure of the low-energy bands. (b) The fine structure of the low-energy bands in the bandgap region with mostly direct bandgap of 265 meV the valence $k = -0.910$ nm$^{-1}$ and the conduction $k = -0.904$ nm$^{-1}$ bands. (c) Detail view at the low-energy conduction band shows its splitting due to SOC with the value of $2\lambda_{\mathrm{I}} = 24\,\mu$eV at the K point.

proposed based on symmetry arguments decades ago by Slonczewski [27] and derived considering TB model and introduced in Eq. (2.49).

Let us take a detail look at this on-site wave functions to use their properties to explain the spin-splitting we observe in bilayer graphene. The on-site Bloch wave functions for the $\pi$ bands on the $i$-th layer is identified as

$$\begin{aligned} \Psi_{\vec{K},\mathrm{A}_i,s} &= \Psi_{\vec{K},\mathrm{A}_i,p_z,s} + i\gamma\Psi_{\vec{K},\mathrm{B}_i,d_+,s}\,, \\ \Psi_{\vec{K},\mathrm{B}_i,s'} &= \Psi_{\vec{K},\mathrm{B}_i,p_z,s'} + i\gamma\Psi_{\vec{K},\mathrm{A}_i,d_-,s'}\,, \end{aligned} \tag{4.7}$$

where $\Psi_{\vec{K},\mathrm{A}_i,\mu,s}$ are the orbital resolved wave functions defined in Eq. (2.2), $s, s' = \{\uparrow,\downarrow\}$ denote the spin eigenstates pointing along the electric field, and the quantum numbers A, B correspond to the eigenstates of the sublattice pseudospin. The two states in Eq.(4.7) are given by a combination of $p$ and $d$ orbitals with opposite pseudospin. But these states can be still labeled as the eigenstates of the pseudospin because the contribution of the $d$-orbitals is very small with $\gamma \approx 0.09$ [62] (see Sec. 2.5.3). The degeneracy of the $d_+ = d_{xz} + id_{yz}$ and $d_- = d_{xz} - id_{yz}$ rotating orbitals is lifted due to the non-zero magnetic quantum number and is governed by the $\mathbf{L}\cdot\mathbf{S}$ term with the energy-splitting $\xi_d$. Each of the states $\Psi_{\mathrm{A}_i,s}$ and $\Psi_{\mathrm{B}_i,s'}$, therefore, become spin-split due to SOC with the energy gap of $2\lambda_\mathrm{I} = 4\gamma^2\xi_d$ by considering the SOC as a first order perturbation. The $d_+$ ($d_-$) orbital implies that the corresponding spin up (down) state is higher in energy. Due to a unique relation between the magnetic quantum number of the $d$ orbitals an the pseudospin in Eq.(4.7) the states $\Psi_{\mathrm{A}_i,s}$ and $\Psi_{\mathrm{B}_i,s'}$ with opposite spin $s \neq s'$ and pseudospin stay degenerate. (see left side of Fig. 4.7). This fact gives us an important argument for understanding the spin splitting in bilayer and also in other FLGs: namely, if there are two degenerate eigenstates built by two on-site states in Eq.(4.7) with opposite pseudospin, the eigenstates stay degenerate if SOC is applied, because the spin splittings of each of the on-site states cancel each other. In contrast, if the given eigenstate is built by on-site states with the same pseudospin, their splitting by the SOC implies the spin splitting of the eigenstate. This argument can explain the spin splittings at the K points to in FLGs band structures.

In the Bernal structure of bilayer graphene the inter-layer hopping $\gamma_1$ repels the states $\Psi_{\vec{K},\mathrm{A}_1,s}$ and $\Psi_{\vec{K},\mathrm{B}_2,s'}$ with opposite pseudospin in energy by building bonding and anti-bonding states $\Psi_{\vec{K},4,s}$ and $\Psi_{\vec{K},1,s}$. The hopping conserves spin and does not break the pseudospin degeneracy, such that the resulting bands stay spin-degenerate. Thus the spin-splitting of the remaining four low-energy eigenstates $\Psi_{\vec{K},3,s} = \Psi_{\vec{K},\mathrm{A}_2,s}$ and $\Psi_{\vec{K},2,s} = \Psi_{\vec{K},\mathrm{B}_1,s'}$ results in the anti-crossing of the corresponding spin-degenerate bands. When transverse electric field is applied the energy of the on-site states at different layers differs by the potential energy $V$. The pseudospin degeneracy of the high-energy states at $\mathrm{A}_1$, $\mathrm{B}_2$ and low-energy states at $\mathrm{A}_2$, $\mathrm{B}_1$ get lifted, see right side of Fig. 4.7. The spin-splitting

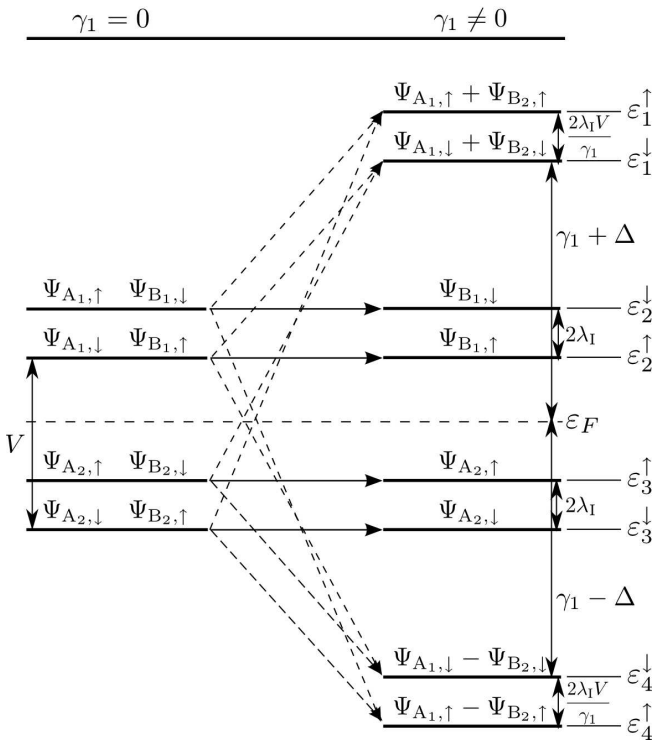


**Figure 4.7:** Energy spectrum diagram at the K point of bilayer AB stacked graphene without (left) and with (right) inter-layer hopping $\gamma_1$. The states on different layers are separated in energy by the electrostatic potential $V$. The states at the sites $A_2$ and $B_1$ are split due to SOC whereas the remaining states are shifted in energy due to inter-layer hopping $\gamma_1$ and spin split by $2\lambda_I V/\gamma_1$, with $\lambda_I \ll V \ll \gamma_1$. For large $V > \gamma_1$ there is charge transfer form $A_1$ to $B_2$ and thus the splitting saturates to $2\lambda_I$. The energies are $\varepsilon_i^s$ with $i = \{1, 2, 3, 4\}$ and $s = \{\uparrow, \downarrow\}$ from top to bottom, see Eq. (4.6).

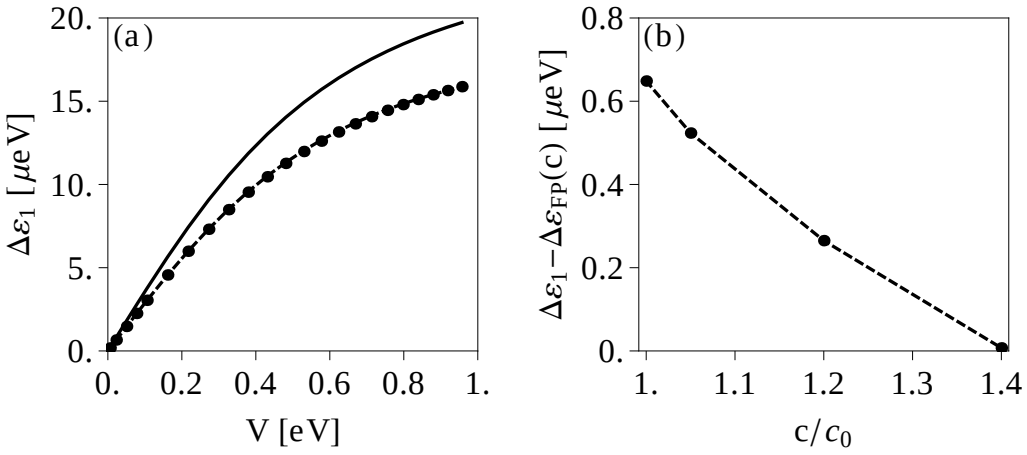


**Figure 4.8:** (a) Spin-splitting of the high-energy bands at the K point as a functions of electrostatic potential $V$: (solid line) TB result with $2\lambda_I = 24\,\mu$eV, (dashed line) TB result with $2\lambda_I = 20\,\mu$eV and (circles) FP results. (b) The absolute difference of TB with $2\lambda_I = 24\,\mu$eV and the FP results at $E = 1\,$V/nm as a function of relative inter-layer distance $c/c_0$.

of the each low-energy state $\Psi_{\vec{K},2,s}$ and $\Psi_{\vec{K},3,s'}$ is $|\varepsilon_2^{\uparrow} - \varepsilon_2^{\downarrow}| = |\varepsilon_3^{\uparrow} - \varepsilon_3^{\downarrow}| = 2\lambda_I$, which results in the spin-splitting of the corresponding low-energy bands. The spin-splitting of the high-energy states increases linearly with $V$ for $V \ll \gamma_1$ and saturates to $2\lambda_I$ for $V \gg \gamma_1$. This behavior is well described by the functions $\Delta\varepsilon_1 = \varepsilon_1^{\uparrow} - \varepsilon_1^{\downarrow}$ and $\Delta\varepsilon_4 = \varepsilon_4^{\downarrow} - \varepsilon_4^{\uparrow}$. But the results of our FP calculations are reproduced only if $2\lambda_I = 20\,\mu$eV. If we increase the inter-layer distance in the FP calculations any contribution of inter-layer effect vanishes. The absolute difference between $2\lambda_I(c)$ as function of the inter-layer distance $c$ and the value of SOC induced band gap in graphene, $2\lambda_I = 24\,\mu$eV, is shown in Fig. 4.8. Already by $c = 1.4c_0$ with $c_0 = 0.335\,$nm the spin-splitting of the high-energy bands is given for $2\lambda_I = 24\,\mu$eV. Consequently, the reduction of $2\lambda_I$ from the $24\,\mu$eV can be considered as an inter-layer effect.

The on-site coupling of the $s$ and $p_z$ orbitals due to the Stark effect leads together with the SOC of $p$-orbitals to the extrinsic intra-layer effect, the BRSOC [23, 26], whose strength is described by the parameter $\lambda_{BR}$ (see chapter 2). The resulting spin-splitting of the bands in single-layer graphene is constant in $k$, corresponds to $2\lambda_{BR}$ in the reasonable interval of k values around the K point and scales linearly with the electric field having the found value of $10\,\mu$eV for the electric field of $E = 1\,$V/nm [26].

In bilayer graphene the shape of spin-splitting as a function of $k$ is more complex due to an interplay of the Bychkov Rashba and intrinsic SOC effects.

| TB parameter [eV] | $\Delta$ | $\gamma_0$ | $\gamma_1$ | $\gamma_3$ | $\gamma_4$ |
|---|---|---|---|---|---|
| bilayer | 0.0096 | 2.6 | 0.339 | 0.29 | -0.143 |
| bilayer [$E = 25\,\mathrm{mV/nm}$] | 0.0096 | 2.6 | 0.339 | 0.28 | -0.145 |
| bilayer [$E = 1\,\mathrm{V/nm}$] | 0.0096 | 2.6 | 0.339 | 0.25 | -0.165 |
| bilayer [$E = 10\ \mathrm{V/nm}$] | 0.0092 | 2.6 | 0.348 | 0.26 | -0.100 |

**Table 4.2:** TB parameters obtained by fitting the band structure to the FP calculations. The signs of the parameters are chosen to be consistent with the SWMcC parameterization presented in Ref. [2]. The presented values of the TB parameters are of the same order as in the literature.[3, 4, 5, 6] and are consistent with values of Ref. [7] obtained from bilayer band-structure calculation using WIEN2k code.

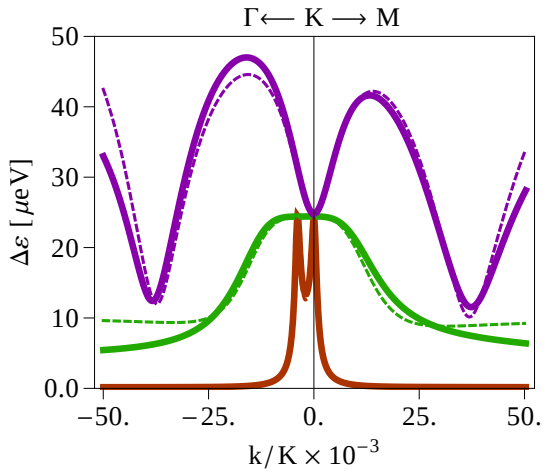


**Figure 4.9:** The spin-splittings of the low-energy-conduction band for the electric field of $E = 25\,\mathrm{mV/nm}$ (red), $E = 1\,\mathrm{V/nm}$ (green), $E = 6\,\mathrm{V/nm}$ (violet). The solid lines shows the FP and dashed lines the TB results.

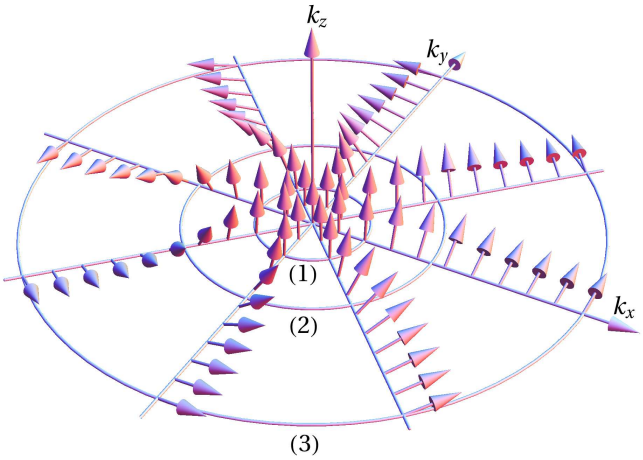


**Figure 4.10:** The spin alignment in the low-energy-conduction band as function of $\vec{k}$ for different directions. The $k_x$ axes corresponds to ΓKM line. The circles corresponds to (1) $k/K = 0.01$, with the corresponding energy $\varepsilon = 56\,\mathrm{meV}$ and angle between the spin pointing vector and the $k_z$ axes $\theta = 5.5°$ (2) $k/K = 0.0225$, $\varepsilon = 119\,\mathrm{meV}$, $\theta = 45.5°$ (3) $k/K = 0.05$, $\varepsilon = 355\,\mathrm{meV}$, $\theta = 80.5°$.

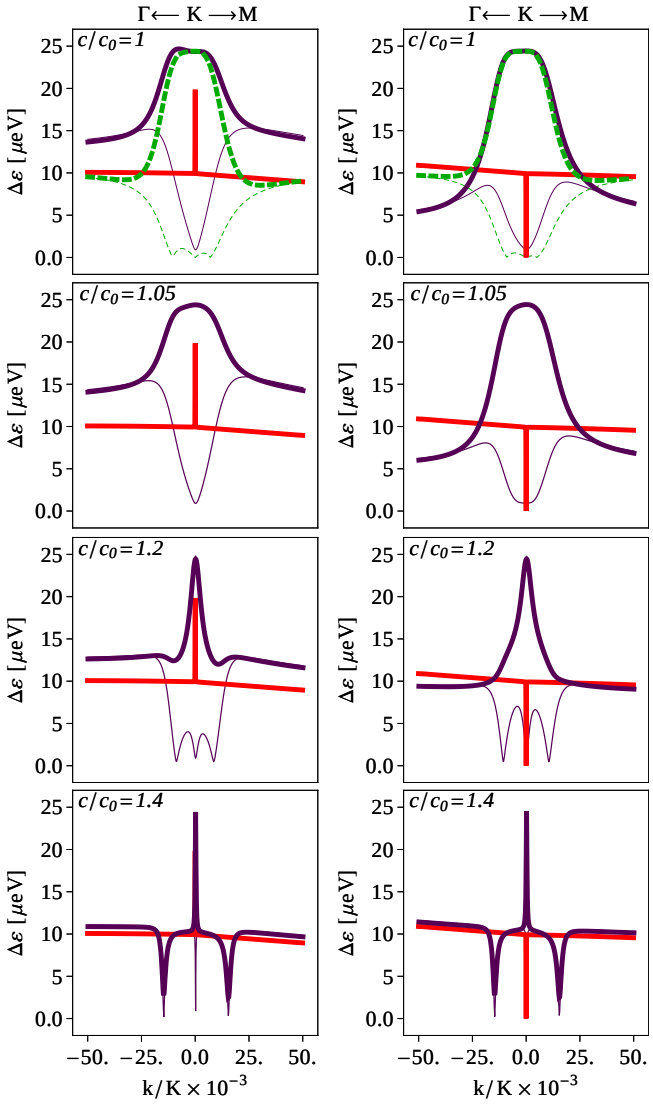


**Figure 4.11:** Solid lines shows the low-energy valence-band the spin splitting on the left side and the conduction-band on the right side of the bilayer graphene at $E = 1\,\mathrm{V/nm}$ (violet) with increasing inter-layer distance $c$ with $c_0 = 0.335\,\mathrm{nm}$ in relation to graphene (red). The thin solid lines shows the splitting if only $p$ orbitals are included. The dashed lines shows the results of the TB model, where the thin dashed line shows the spin-splitting given only by the BRSOC.

Such behavior can be understood by looking at the eigenstates of the spinless Hamiltonian given for the $n$-th band and finite wave vector $k$. Such eigenstate of $n$th band is expressed by the superposition of all on-site wave functions in the unit cell, say

$$\Psi_{\vec{k},n} = a^{(1)}_{\vec{k},n}\Psi_{\vec{k},\mathrm{A}_1} + b^{(1)}_{\vec{k},n}\Psi_{\vec{k},\mathrm{B}_1} + a^{(2)}_{\vec{k},n}\Psi_{\vec{k},\mathrm{A}_2} + b^{(2)}_{\vec{k},n}\Psi_{\vec{k},\mathrm{B}_2}. \tag{4.8}$$

The on-site wave function have in general the form given by Eq.(4.7), but in general, there is a contribution from the $s$ and in-plane $p$ orbitals, which is not presented explicitly here. In our discussion of the spin splittings the exact expression is not important, it is enough to have in mind that this part is responsible for the inter-layer coupling the spin-up and spin-down states of the neighboring on-site wave functions by BRSOC. Hence the resulting spin splitting of the eigenstates depends on the coefficients $a^{(i)}_{k,n}$, $b^{(i)}_{k,n}$ and correspond to $2\lambda_{\mathrm{BR}}\sum_i |a^{(i)}_{k,n}||b^{(i)}_{k,n}|$ by considering the SOC as a perturbation. At the K point either $a^{(i)}_{k,n}$ or $b^{(i)}_{k,n}$ are zero as shown in Fig. 4.7. Hence the BRSOC effect disappears and the spin splitting of the bands is entirely given only by the intrinsic SOC originating from the $d$ orbitals as discussed above. For a finite $k$ all on-site wave functions contribute to the eigenstates and their spin-splitting due to BRSOC depends on the relative values of $a^{(i)}_{k,n}$, $b^{(i)}_{k,n}$, reaching the maximum value if the coefficients became equal, like in the case of single layer graphene. In bilayer graphene this case is reached for large $k$ being roughly 5% of the ΓK line with respect to the K point. Consequently the spin splitting saturates to the value of single layer graphene $2\lambda_{\mathrm{BR}}$ shown for the low-energy bands by the dashed lines in the top part of Fig. 4.11.

The shape of the spin splittings as a function of $k$ due to intrinsic SOC can be handled in the same way, considering the coefficients in on-site wave-function expansion of the $n$th eigenstate. There is an opposite situation to the BRSOC effect: for equal coefficients $a^{(i)}_{k,n}$ and $b^{(i)}_{k,n}$ the spin splitting is zero and has it maximum value of $2\lambda_{\mathrm{I}}$ at the K point where either $a^{(i)}_{k,n}$ or $b^{(i)}_{k,n}$ is zero. This is due to the fact that the energies of the on-site states with the same spin but opposite pseudospin sum up to zero.

Consequently, for very small $k$ the eigenstates are similar to the ones at K and the intrinsic SOC effect dominates the spin-splitting, being at the order of $24\,\mu$eV for the low-energy states as shown in top picture of Fig. 4.7. In contrast, for large $k$, the neighboring on-site functions $\Psi_{\vec{k},\mathrm{A_i}}$ and $\Psi_{\vec{k},\mathrm{B_i}}$ contribute equally to the eigenstates and therefore the BRSOC determines the spin-splitting. This fact has crucial consequences for the spin alignment as a function of wave vector $\mathbf{k}$ shown in Fig. 4.10 for the spin-up state of the low-energy conduction band. The intrinsic SOC term is diagonal in the spin. Hence the spin vector is orthogonal to the graphene plane (by definition) at the K point. Then it is rotated into plane going with increasing $k$ due to increasing contribution of the

Bychkov-Rashba effect reaching the single graphene case, where the spin is in plane as shown in Fig. 3.9.

The above discussed saturation of the spin splittings of the bands by $2\lambda_{\mathrm{BR}}$ for large $k$ is observed in the FP results only for small electric fields ($< 0.1\,\mathrm{V/nm}$). We believe, that the reason for the deviation of the spin splittings for larger electric fields are inter-layer SOC effects, which couple the on-site spin-up and spin-down states sitting on different layers. This statement is proved by increasing the inter-layer distance. In Fig. 4.11 we show that the spin splitting of the low-energy bands by the electric field of $1\,\mathrm{eV/nm}$ (given by solid lines) approaches the graphene case (red solid line) as the inter-layer distance increases. The thin solid lines shows the case where the $d$ and higher orbitals are excluded from the FP calculations. Hence they represent the splitting given by intra-layer BRSOC and inter-layer SOC effects. The overlap of the thin and thick lines defines the region where the BRSOC effect dominates the spin splitting, where the contribution of the intrinsic SOC is nearly zero. In this region the energy difference between the spin splitting of the bilayer (violet line) and single layer (red line) graphenes gives the contribution of the inter-layer SOC.

The relative contribution of the inter-layer SOC effects reduces with the increasing electric field, since the layers became more separated in energy by the electrostatic potential $V$. Figure 4.9 shows the spin splitting of the low-energy conduction band for different electric fields. For the smallest field the spin-splitting is given only by the intrinsic SOC effect. For intermediate field ($1\,\mathrm{V/nm}$) there is a disagreement of the FP and TB results for large $k$ due to the inter-layer SOC effects as discussed above. At the same $k$ points the relative difference of the FP and TB results is hardly reduced for large electric fields. Here the the spin splitting of the shown band is mostly given by the intra-layer BRSOC effect, except the K point.

## 4.5 Trilayer graphene

In the previous section we have shown that the spin-splitting of the $\pi$ bands occurs in bilayer graphene when applying a transverse electric field. In trilayer graphene spatial inversion symmetry depends on the stacking itself. The ABC stacked trilayer graphene possesses structural inversion. Consequently, the bands are spin degenerate. As in the case of bilayer graphene, the spin degeneracy is removed by applying external electric field perpendicular to the layers. In ABA trilayer graphene, in contrast, the spatial symmetry is not present and thus spin degeneracy is lifted by the structure itself. In the following subsections we will discuss the band structures and their SOC effects for each stacking case in detail using the on-site wave functions of Eq. (4.7). The unique relation of spin and pseudospin degrees of freedom in the on-site wave functions allows

us to explain the appearance of spin splitting at the K points in the different structures.

### 4.5.1 ABA-stacked trilayer graphene

Figures 4.12 present the band structures of the ABA-stacked trilayer graphene for three different scales. The largest scale in Figs 4.12(a) shows the high-energy band separations from the low-energy bands driven mostly due to $\gamma_1$ hopping. The number of the high-energy bands depends on the number of states repelled by $\gamma_1$ hopping. ABA-stacked trilayer graphene contains eight low-energy bands associated with atoms $A_1$, $B_1$, $A_2$, and $B_3$. The two high-energy bands are combination of on-site states at atoms $A_1$, $A_3$ and due to $\gamma_5$ and $\gamma_1$ hopping, the states localized at atom $B_2$ are involved as well. At the K point the energy spectrum of the six bands reads

$$\begin{aligned}
\varepsilon_1^{\uparrow} &= \frac{1}{2}\left(\gamma_5 + 2\Delta + \sqrt{8\gamma_1^2 + (\gamma_5^2 + 2\lambda_{\mathrm{I}})^2}\right), \\
\varepsilon_1^{\downarrow} &= \frac{1}{2}\left(\gamma_5 + 2\Delta + \sqrt{8\gamma_1^2 + (\gamma_5^2 - 2\lambda_{\mathrm{I}})^2}\right), \\
\varepsilon_2^{\downarrow} &= \delta - \gamma_2 + \lambda_{\mathrm{I}}, \qquad \varepsilon_2^{\uparrow} = \delta - \gamma_2 - \lambda_{\mathrm{I}}, \\
\varepsilon_3^{\uparrow} &= \Delta - \gamma_5 + \lambda_{\mathrm{I}}, \quad \varepsilon_3^{\downarrow} = \Delta + \gamma_5 - \lambda_{\mathrm{I}}, \\
\varepsilon_4^{\uparrow} &= \lambda_{\mathrm{I}}, \qquad\qquad \varepsilon_4^{\downarrow} = -\lambda_{\mathrm{I}}, \\
\varepsilon_5^{\downarrow} &= \delta + \gamma_2 + \lambda_{\mathrm{I}}, \quad \varepsilon_5^{\uparrow} = \delta + \gamma_2 - \lambda_{\mathrm{I}}, \\
\varepsilon_6^{\uparrow} &= \frac{1}{2}\left(\gamma_5 + 2\Delta - \sqrt{8\gamma_1^2 + (\gamma_5^2 - 2\lambda_{\mathrm{I}})^2}\right), \\
\varepsilon_6^{\downarrow} &= \frac{1}{2}\left(\gamma_5 + 2\Delta - \sqrt{8\gamma_1^2 + (\gamma_5^2 + 2\lambda_{\mathrm{I}})^2}\right).
\end{aligned} \tag{4.9}$$

The sketch of the energy spectrum is shown in Fig. 4.13. The corresponding eigenstates are built by the on-site wave functions introduced in Eq.(4.7). The fine structure in Fig. 4.12(b) shows the low-energy bands. It resembles the bilayer and single-layer graphene low-energy spectra with a band gap when comparing the parabolic and linear bands around the K point, respectively. The 'gaps' are given by the direct next-nearest-neighbor inter-layer hopping $\gamma_2$ and $\gamma_5$ (see Fig. 4.13), where the graphene-like band gap is given by $\varepsilon_2 - \varepsilon_3$ and the K point splitting of the bilayer-like bands by $\varepsilon_4 - \varepsilon_5$ in Eq. (4.9). Due to crossing of the graphene-like valence band the bilayer like conduction bands there is no real band gap in ABA-stacked trilayer graphene. The on-site states $\Psi_{\vec{K},\mathrm{A}_2,\mathrm{s}}$ are not coupled to other atoms of the primitive unit cell. Therefore they form the low-energy band at the Fermi level. The on-site states $\Psi_{\vec{K},\mathrm{B}_1,\mathrm{s}}$ and

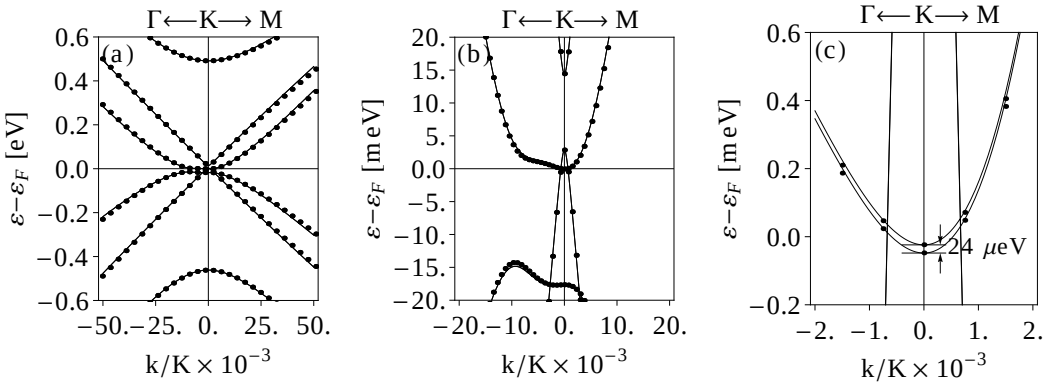


**Figure 4.12:** The calculated band structure of $\pi$ bands in ABA trilayer graphene along ΓKM lines. Circles show the results of the FP and lines the TB calculations. All six bands are shown in (a), where the two parabolic high-energy bands are repelled by $\gamma_1$ hopping at K. Two of the four low-energy bands have graphene-like linear dispersion, while the dispersion of the two remaining bands is parabolic similar to bilayer. The fine structure of the low-energy band is shown in (b) and discovers the bands gaps in the single structures. The detail view in (c) shows the spin splitting of 24 $\mu$eV in the lowest conduction band.

$\Psi_{\vec{K},\mathrm{B}_3,s}$ are separated by $2\gamma_2$ in energy and form the bonding and anti-bonding states close to the Fermi level. The $\gamma_5$ hopping pairs the on-site states $\Psi_{\vec{K},\mathrm{A}_1,s}$ and $\Psi_{\vec{K},\mathrm{A}_3,s}$ forming one low-energy band.

SOC splits each of the low-energy bands. The spin splitting depends on the wave vector and is of the order of tens of micro electron volts in the vicinity of the K point with the maximum value roughly of $24\,\mu$eV at the K point. Figure 4.12(c) shows spin splitting of one of the conduction bands. The splitting drops below $3\,\mu$eV if $d$ orbitals are not included in FP calculations. The correlation between the value of the intrinsic SOC effect in a single sheet graphene at the K point and the trilayer structure is conspicuous. Therefore, we perform further analysis to have deeper insight into the physics of SOC in the trilayer structure. As in the case of bilayer graphene, we explore the effects of SOC in terms of the on-site wave functions introduced in Eq.(4.7). Each on-site wave function spin splits by to SOC due to the $d$ orbital contribution, such that the states with opposite sublattice pseudospin and real spin have the same energy. Thus, there are six degenerate on-site states if any inter-layer hopping is set to zero. When turning the inter-layer hopping on, the six-fold degeneracy is lifted. The eigenstates at the K point in ABA are given by linear combinations of the on-site states Eq.(4.7) and are shown in the spectrum sketch in the left part of Fig. 4.13. The inter-layer hopping conserves the spin. Thus, the spin degeneracy of the resulting bands is only possible if the chosen band is at least twice degenerate and those eigenstates have different pseudospin. The eigenstates with the same pseudospin will be split by the SOC in the real spin up and spin down states. The hoppings $\gamma_2$ or $\gamma_5$ combine states with the same sublattice pseudospin, B or A, respectively. Thus the low-energy bands become split by the SOC due to spin-splitting of the on-site states $\Psi_{\vec{K},\mathrm{B}_1,s}$ and $\Psi_{\vec{K},\mathrm{B}_3,s}$ or $\Psi_{\vec{K},\mathrm{A}_i,s}$, respectively, as shown in Fig. 4.13. The first neighbor inter-layer hopping $\gamma_1$ repels the on-site states $\Psi_{\vec{K},\mathrm{A}_1,s}$ and $\Psi_{\vec{K},\mathrm{B}_2,s}$, and $\Psi_{\vec{K},\mathrm{B}_2,s}$ and $\Psi_{\vec{K},\mathrm{A}_3,s}$ by forming the high-energy bands, such that each of the corresponding eigenstates is built by all three on-site wave functions, states with opposite pseudospin. However, the eigenstates are spin split as seen by FP calculations. This fact seems to be a contradiction because the high-energy eigenstates should be degenerate due to the pseudospin degeneracy statement. However, as we pointed out in previous section, the spin-splitting depends on the coefficients in the expansion of the eigenstates in the basis of the on-site wave functions. Thus the spin-splitting of the high-energy states is given by $2\lambda_\mathrm{I}(2-\alpha_\pm^2)/(2+\alpha_\pm^2)$ with $\alpha_\pm = -\gamma_5/(2\gamma_1) \pm \sqrt{2+[\gamma_5/(2\gamma_1)]^2}$ by considering the SOC as perturbation in the first order, where $(+)$ denotes the conduction and $(-)$ the valence band. Here the second nearest inter-layer hopping $\gamma_5$ plays the crucial role, even if $\gamma_5 \ll \gamma_1$ (see Tab. 4.1). Setting $\gamma_5 = 0$ leads to the spin degeneracy of the high-energy bands, because $\alpha_\pm = \pm\sqrt{2}$ then. Up to the first order in $\gamma_5$ the estimate of the spin splitting corresponds to the energy differences $|\varepsilon_1^\uparrow - \varepsilon_1^\downarrow| = |\varepsilon_6^\uparrow - \varepsilon_6^\downarrow| \approx \lambda_\mathrm{I}\gamma_5/(2\sqrt{2}\gamma_1)$. This explains the small

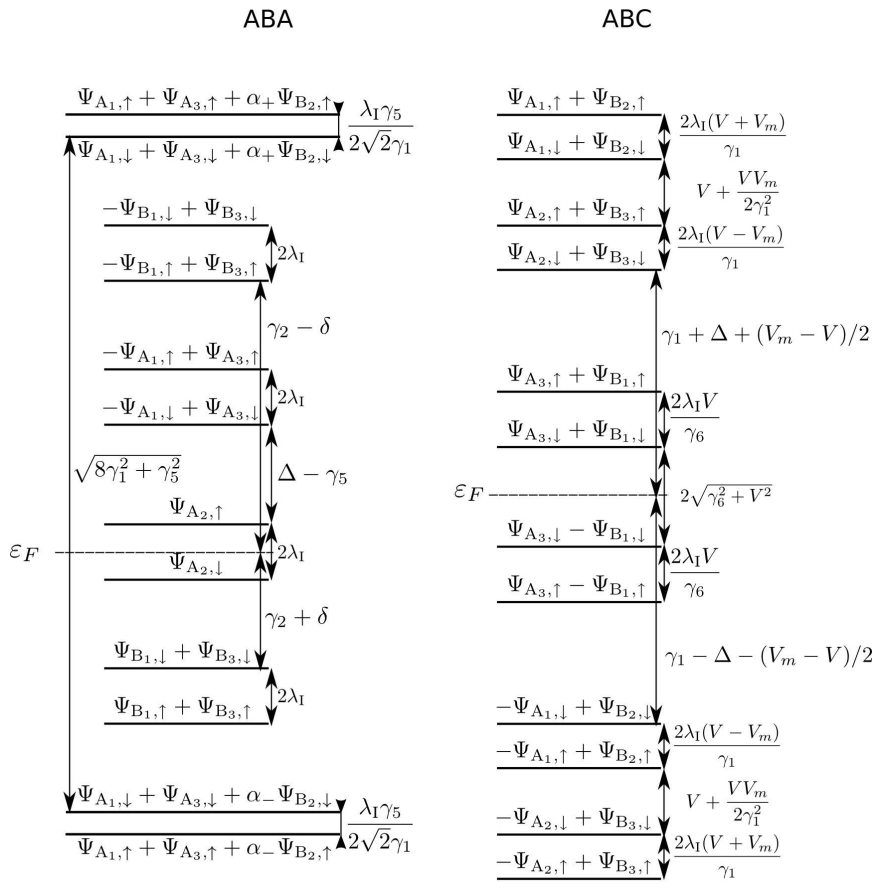


**Figure 4.13:** Energy spectrum diagram with the corresponding eigenstates at the K point of trilayer ABC stacked and ABA stacked graphenes. Solid lines are the energy levels. For the SOC-induced splittings we use $\lambda_I \ll V$, $V_m \ll \gamma_l$ with $l = \{1, 6\}$ and $\gamma_5$ $ll\gamma_1$ holds.

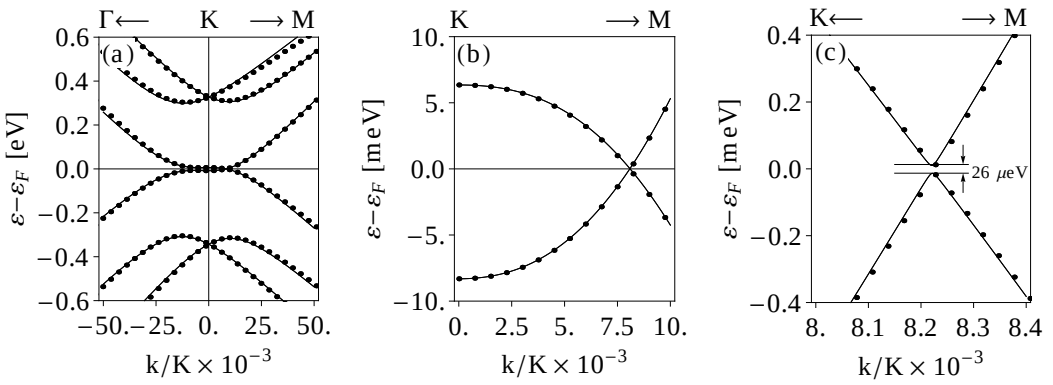


**Figure 4.14:** The calculated band structure of $\pi$ bands in ABC trilayer graphene. There are four repelled high-energy band shown in (a). The parabolic conduction (valence) bands cross at the K point. The low-energy bands are split at the K point by $2\gamma_6$ but cross accidentally at the KM line for $k = 0.1334\,\mathrm{nm}^{-1}$ as shown in (b). The detail view in (c) shows the band gap at the crossing point with the value of 26 $\mu$eV.

values 2.3 $\mu$eV and 4 $\mu$eV for the spin-splittings of the high-energy valence and conduction bands, respectively. However using the TB parameters in Tab. 4.1, one obtains a splitting value one order of magnitude smaller then the numerical results. Indeed, such small values are at the limit of numerical tolerance, such that the high-energy bands appears to be nearly spin-degenerate.

### 4.5.2 ABC-stacked trilayer graphene

The electronic structure of ABC trilayer graphene involve a cone-like structure, similar to the single layer graphene band structure at K, but the cones are shifted to a point on the KM high-symmetry line. This fact does makes it impossible to write down a simple Hamiltonian for the cones, as in the case of graphene. Nevertheless, we will show that ABC trilayer combines the features of single layer and bilayer graphenes: The crossing of the bands at the Fermi energy makes ABC trilayer a gapless semiconductor, but with a widely tunable band gap using transverse electric field as in the case of bilayer graphene.

In ABC-stacked trilayer graphene, there are four spin-degenerate high-energy states [see Fig. 4.14(a)] associated with atoms $A_1$, $B_2$, $A_2$ and $B_3$ at the K points. These states are repelled from the Fermi energy by the inter-layer $\gamma_1$ hopping. The two remaining low-energy states are associated with the atoms $A_3$ and $B_1$ and separated by the $\gamma_6$ hopping parameter in energy. The accidental crossing of the low-energy bands, shown in Fig. 4.14(b), determines the Fermi energy

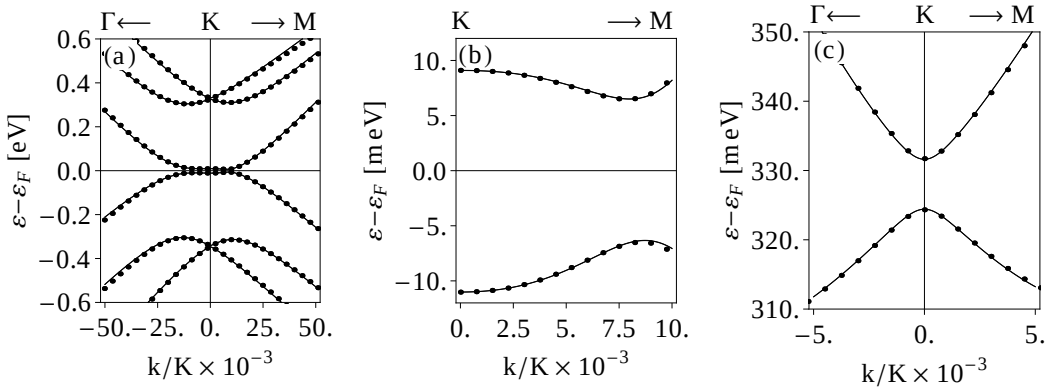


**Figure 4.15:** The calculated band structure of the $\pi$ bands in ABC trilayer graphene with applied electric field of 0.1 V/nm. (a) shows all six bands. The low-energy bands are split at the K point by $2\sqrt{V^2+\gamma_6^2}$, where the band gap of 13 meV at the KM line is shown in (b). The high-energy band splitting of 7.4 meV due to electric field is shown in (c).

level.

The applied electric field separates the outer layers in energy by the electrostatic potential $V$ and induces a tunable band gap, shown in Fig. 4.15(b) for an electric field of $E = 0.1\,\mathrm{V/nm}$. Figure 4.16(c) shows the band gap as a function of the electric field up to $E = 10\,\mathrm{V/nm}$. In comparison with the bilayer gap, the ABC gap is always direct and does not saturate. The external field enlarges the splitting of the low-energy bands at the K points, which is given by the difference of the eigenenergies

$$\begin{aligned} \varepsilon_3^{\uparrow,\downarrow} &= \delta + \sqrt{\gamma_6^2 + (V \pm \lambda_\mathrm{I})^2}\,, \\ \varepsilon_4^{\downarrow,\uparrow} &= \delta + \sqrt{\gamma_6^2 + (V \pm \lambda_\mathrm{I})^2}\,, \end{aligned} \tag{4.10}$$

and at the same time provides the value of the electrostatic potential $V$ by fitting the energies in Eq. (4.10) to the FP spectrum. The value of the parameter $\gamma_6$ is fixed by the K point splitting at $E = 0$. Figure 4.16(a) shows the shape of the K point splitting as a function of electric field (red line). In comparison with the low-energy splitting figure 4.16(a) also shows the splittings of the high-energy bands at the K point (green and blue lines). Here the corresponding on-site states are put to different potentials arising between neighboring layers (see the right picture of Fig. 4.13). There is a small difference in the splitting values of both high-energy and the low-energy bands. This difference is modeled by the non-zero potential $V_m$ acting on the middle layer. The shape of $V_m$ as a function of the electric field is shown in Fig. 4.16(e) and is obtained by comparing the

high-energy spectrum of the effective Hamiltonian in Eq. (4.5) at the K point,

$$\begin{aligned}
\varepsilon_1^{\uparrow,\downarrow} &= \frac{1}{2}\left(V_m + V + 2\Delta + \sqrt{(V - V_m \pm \lambda_\mathrm{I})^2 + 4\gamma_1^2}\right) , \\
\varepsilon_2^{\uparrow,\downarrow} &= \frac{1}{2}\left(V_m - V + 2\Delta + \sqrt{(V + V_m \pm \lambda_\mathrm{I})^2 + 4\gamma_1^2}\right) , \\
\varepsilon_5^{\downarrow,\uparrow} &= \frac{1}{2}\left(V_m + V + 2\Delta - \sqrt{(V - V_m \pm \lambda_\mathrm{I})^2 + 4\gamma_1^2}\right) , \\
\varepsilon_6^{\downarrow,\uparrow} &= \frac{1}{2}\left(V_m - V + 2\Delta - \sqrt{(V + V_m \pm \lambda_\mathrm{I})^2 + 4\gamma_1^2}\right) ,
\end{aligned} \tag{4.11}$$

with the results of our FP calculations. The values of the electrostatic potential $V$ are used as input to determine the values of $V_m$, $\gamma_1$, and $\Delta$ from the spectrum of the high-energy bands. The shapes of $\gamma_1$ and $\Delta$ as functions of the applied electric field are shown in Fig. 4.16 by (b) and (d), respectively. The dependence of the parameter $\delta$ on the electric field is shown Fig. 4.16(d). Both asymmetry parameters $\Delta$ and $\delta$ yield a minimum for an electric field of 6 V/nm. The reason for the appearing minimum is band inversion: The electric field pulls the low-energy bands and the lower high-energy bands towards each other, such that for a large enough value the bands touch each other. By further increasing of the electric field, the eigenstates in Eq. (4.10) exchange places with the eigenstates given by $\varepsilon_2$ and $\varepsilon_5$ in Eq. (4.11) in the spectrum of Fig. 4.13, such that the former lower high-energy bands become low-energy bands and vice versa.

As in the case of bilayer graphene, the SOC effects at the K point in ABC trilayer graphene can be understood in terms of the interplay between the electrostatic potential $V$, the direct inter-layer hopping $\gamma_1$ and $\gamma_6$, and the intrinsic intra-layer SOC controlled by the parameter $\lambda_\mathrm{I}$. A detailed view in Fig. 4.14(c) shows that there is a band gap opening due to SOC of about 26 $\mu$eV, which is again controlled by the $d$ orbitals. The difference between the gap value and the value of 24 $\mu$eV observed in graphene is due non-zero $k$ that enters the splitting. For a finite $k$ the on-site wave functions have different form as introduced in Eq. (2.49). However, we assume that they posses a contribution form the $d$ orbitals, which causes a band gap if SOC is present. The spatial inversion symmetry keeps the eigenstates spin degenerate, and the spin-splittings of the corresponding on-site states with opposite pseudospin cancel each other; see right picture in Fig 4.13. The spin degeneracy is lifted if an external electric field is applied. Here we can use the same arguments as in the case of high-energy bands in bilayer graphene. The splitting of the low-energy bands at the K point is also proportional to $V$ for $V \ll \gamma_6$ and saturates rather fast to the value of $2\lambda_\mathrm{I} = 24\,\mu$eV for $V \gg \gamma_6$. The spin splittings of the high-energy bands are proportional to $2\lambda_\mathrm{I} V/\gamma_1$ if $V \gg \gamma_1$ as shown in Fig. 4.17(a) and saturate at $2\lambda_\mathrm{I} = 20\,\mu$eV as in the case of bilayer graphene.

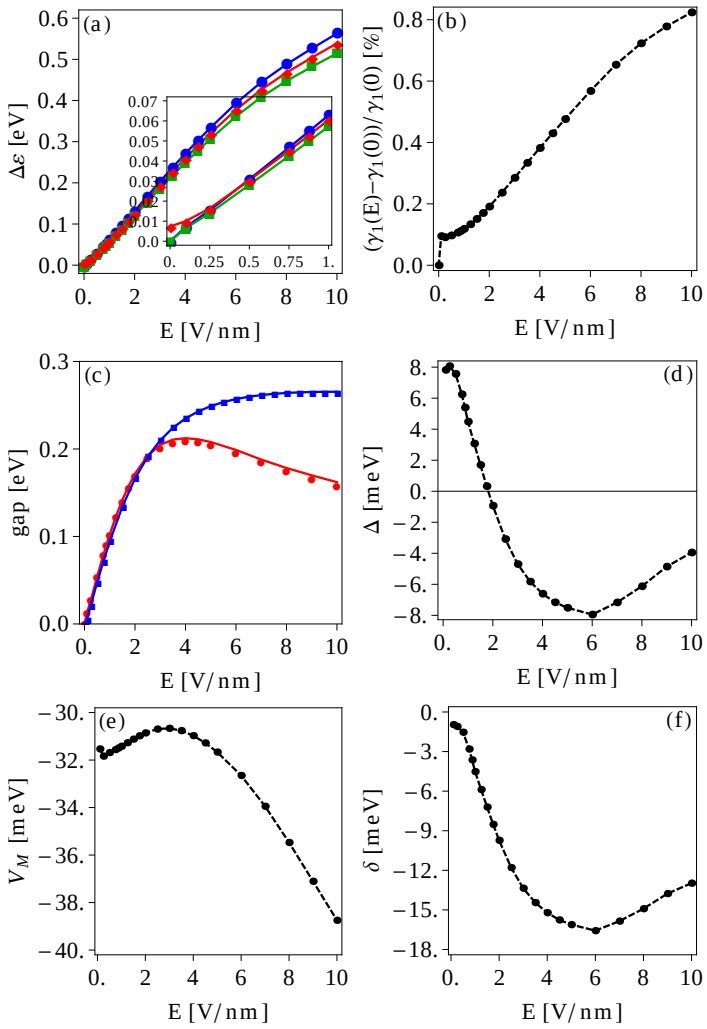


**Figure 4.16:** ABC trilayer graphene essentials in an external electric field obtained from FP calculations (symbols) and the TB model (solid lines). (a) Electric field induced splittings at the K point as functions of the electric field: (blue circles) and (green squares) shows the splittings of the high-energy conduction and valence band, respectively and (red diamonds) shows the splitting of the low-energy band. The inset of (a) shows the low-energy band splitting approaching the value of the hopping parameter $\gamma_6$ for zero electric field, where the high-energy band splittings drop to zero. (b) The relative dependence of the hopping parameter $\gamma_1$ in percent with respect the value in the case of zero electric field. (c) Band gap in biased trilayer graphene (red circles) in comparison to band gap of the bilayer graphene (blue squares) as a function of the applied electric field. (d), (e) and (f) The shape of parameters $\Delta$, $V_M$, and $\delta$ as functions of the electric field, respectively.

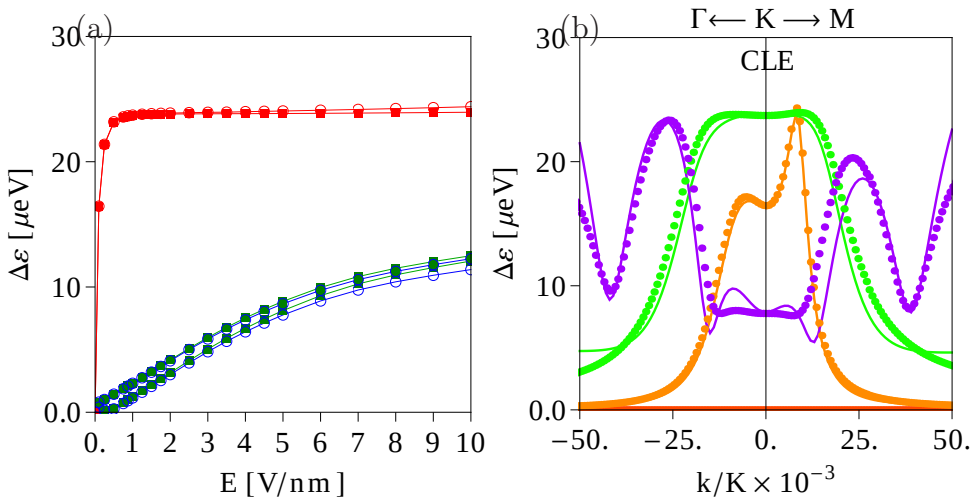


**Figure 4.17:** (a) Spin-orbit coupling induced splitting of the bands in ABC trilayer graphene as a function of electrostatic potential applied between the outermost layers. Solid line shows the TB result, symbols are the FP calculations, where circles shows the conduction bands and squares the valence bands, where (red) low-energy bands, and (blue) and (green) the high lower and higher high-energy bands, respectively. (b) Spin-orbit coupling induced splitting of the low-energy conduction band along ΓKM lines. Circles shows the results of the FP and lines the TB calculations. Color-coded are different values of the electric field: (orange) E=0.1 V/nm, (light green) E=1 V/nm, and (pink) E=5 V/nm with $\lambda_{\mathrm{BR}} = 0.25\,\mu$eV, $\lambda_{\mathrm{BR}} = 2.5\,\mu$eV, and $\lambda_{\mathrm{BR}} = 18\,\mu$eV, respectively.

The BRSOC effect dominates the spin splitting of high-energy bands for finite wave vectors and large electric fields except for the spin splitting at the K points. Here the splitting is due to the intrinsic SOC as shown above. In the case of the low-energy bands there is a competition between the intrinsic SOC and BRSOC similar to the situation of bilayer graphene, but here the additional inter-layer SOC effects play a significant role. Figure 4.17(b) shows the TB and FP results for the spin splitting of the low-energy conduction band for three values of the electric field, which differ in the order of magnitude. The effective Hamiltonian involving the intra-layer SOC effect only gives a good description of the spin splitting of all six bands for wave vectors in the interval of ±5% of ΓK line around the K point and for small values of the electric field (up to 1 V/nm).

To model the exact shape of the spin splittings as functions of $k$ for large

values of the electric field much more complicated models must be introduced. It is possible to obtain by group theoretical arguments a maximum number of SOC parameters in the SOC Hamiltonian at the K point. Doing so, one faces a very complex minimization problem, which could provide the values of the additional SOC parameters. However, there is no guarantee that the K-point approximation stays valid, since the SOC parameters are in general wave vector dependent. Moreover one must not forget in this discussion that we consider electric fields here, which are hardly accessible in the experiments. Finally we conclude that the presented simple model for the extrinsic SOC effects in ABC-stacked trilayer graphene remains an adequate approximation.

## 4.6 Graphite

The electronic structure of graphite has been known for decades [28]. The first investigation of the SOC effects by group theoretical analysis within a k.p model was done by Dresselhaus [63]. We present here a more realistic TB model to describe the SOC effects. The corresponding effective Hamiltonian of graphite can be obtained be expanding the ABA Hamiltonian in Eq. (4.4) to an infinite number of layers. The translation symmetric ordering of the layers in the transverse $z$-direction allows to interpret the single layer as atoms ordered in a linear chain with two atoms in the corresponding unit cell. The band structure of a linear chain is easily obtained by Fourier transformation, and the infinite effective Hamiltonian takes a form of a $4 \times 4$ matrix,

$$\begin{pmatrix} \Delta + \gamma_5\chi + \tau\lambda_{\mathrm{I}1}s_z & \gamma_0 f & \gamma_4 f^*\Gamma & \gamma_1\Gamma \\ \gamma_0 f^* & \gamma_2\chi - \tau\lambda_{\mathrm{I}2}s_z & \gamma_3 f\Gamma & \gamma_4 f^*\Gamma \\ \gamma_4 f\Gamma & \gamma_3 f^*\Gamma & \gamma_2\chi + \tau\lambda_{\mathrm{I}2}s_z & \gamma_0 f \\ \gamma_1\Gamma & \gamma_4 f\Gamma & \gamma_0 f^* & \Delta + \gamma_5\chi - \tau\lambda_{\mathrm{I}1}s_z \end{pmatrix}. \tag{4.12}$$

The consequence of the translation symmetry is that every inter-layer hopping becomes dependent on the out-of-plane wave vector $k_z$ by $\Gamma = 2\cos(k_z c)$ or $\chi = (\Gamma^2 - 2)$. The nearest neighbor inter-layer hoppings $\gamma_1$, $\gamma_3$, and $\gamma_4$ stay off-diagonal, while the second nearest neighbor inter-layer hoppings $\gamma_2$ and $\gamma_5$ appear in diagonal matrix elements. The additional translation symmetry is mirrored by the three dimensional BZ of graphite shown in Fig. 4.18. The band structure of graphite along the ΓKM-line in Fig. 4.19 is similar to the structure of bilayer graphene, where the nearest neighbor inter-layer hopping parameters are twice as large because $\Gamma = 2$ and $\chi = 0$ here. The band structure along the new symmetry line KH is shown in Fig. 4.20(a) where due to the $k_z$ dependence of the inter-layer hopping ($\gamma_1\Gamma$) the high-energy bands cross at the H points. The fine structure of the crossing is shown in Fig. 4.20(c), where the upper

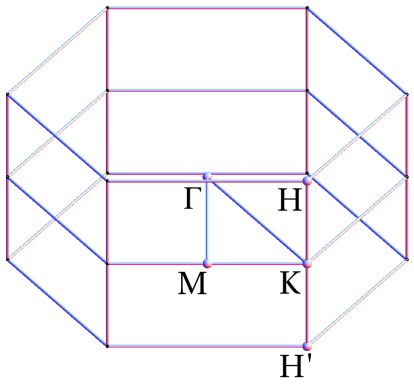


**Figure 4.18:** The 3-dimensional 1st BZ of graphite involving additional high-symmetry points H and H′ and corresponding high-symmetry lines.

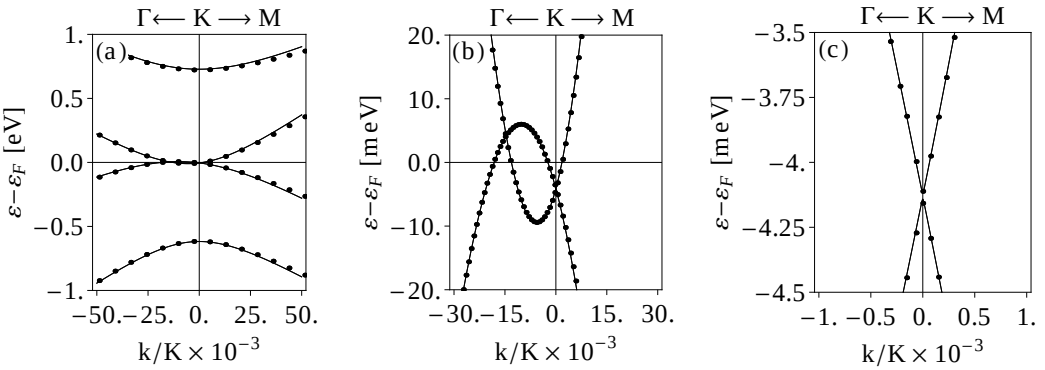


**Figure 4.19:** The calculated band structure of the $\pi$ bands in graphite along the ΓKM lines, where $\mathrm{K} = |\Gamma\mathrm{K}| = 4\pi/(3a)$ with $a = 0.246\,\mathrm{nm}$. First-principles results are indicated by circles and TB results by solid lines. (a) Low and high-energy bands. (b) Fine structure of the low-energy bands discover the crossing of the parabolic bands similar to the case of bilayer graphene. (c) Detailed view of the low-energy bands showing anti-crossings at the K point with a value of $\lambda_{\mathrm{I2}} = 24\,\mu\mathrm{eV}$.

high-energy band crosses the low-energy band. Figure 4.20(b) shows the fine structure of the low-energy band which changes its character from conduction to valence band when crossing the Fermi level.

The intrinsic SOC terms are diagonal in the infinite matrix and remain unaffected by the Fourier transformation. Therefore we expect that the splitting of the low-energy band remains constant at the value of 24 $\mu$eV (see Fig. 4.19(c)). This statement is proved by FP calculations within the WIEN2k code. The resulting spin splitting is shown in Fig. 4.20(d) and it remains constant along the whole KH line including the H point. The linear dispersion of the high-energy bands with arising band gap due to SOC is akin to the cone-like band structure of graphene. The gap is of the order of 12 $\mu$eV, half of the spin splitting of the low-energy band. We found by the group theory arguments that there are two different intrinsic SOC parameters $\lambda_{\mathrm{I}1}$ and $\lambda_{\mathrm{I}2}$ related to the high-energy bands and low-energy bands at K, respectively. Consequently, the non-equivalent values of the SOC parameters lead to different values of splittings at the K and H points. This work is in progress.

## 4.7 Conclusion of the chapter

In this chapter we have shown that the SOC effects in FLGs and graphite are predominately given by the physics manifesting in single-layer graphene. The wave functions of the $\pi$-bands, built by $p_z$ and $d_{xz}$, $d_{yz}$ orbitals, describe sufficiently intrinsic SOC in FLGs. We expect the same SOC effects in all multilayer graphenes up to graphite. The results are supported by the FP calculations providing a basis for the determination of the hopping parameters in the TB model.

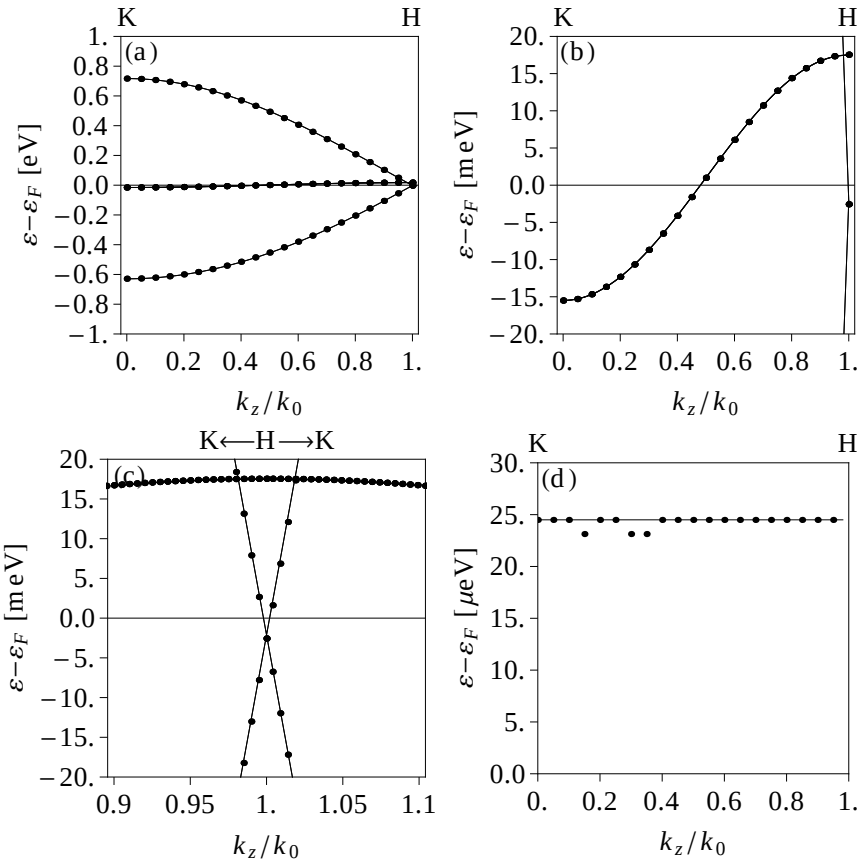


**Figure 4.20:** (a) Electronic structure of graphite along the KH high-symmetry line with a length of $k_0 = \pi/(2c)$. (b) The transmutation of the low-energy band from a the conduction to a valence bands. The Fermi energy ($\varepsilon_F = 0$) crosses the band halfway along the KH line. (c) The band structure in the vicinity of the H point shows the linear dispersion of the high-energy in the vicinity of the H point, where the conduction and valence high-energy bands (anti-)cross at H and $\varepsilon = \Delta - 2\gamma_5$. (d) The spin-splitting of the low-energy band is constant along the KH line and corresponds to $2\lambda_\mathrm{I} = 24.9\,\mu\mathrm{eV}$.

# 5 Conclusion

In this thesis a tight-binding model has been developed to explain realistic electronic properties of single layer graphene, graphene bilayer and ABA and ABC trilayers, as well as graphite. In the tight-binding approximation the Bloch functions have been expressed by a linear combination of the on-site wave functions, which are described by several quantum numbers, namely angular momentum, magnetic, spin, and pseudospin quantum numbers. The on-site wave functions are constructed from the atomic orbitals, localized at the position of the atoms in the crystals. In the basis of the on-site wave functions we have developed multi-orbital tight-binding Hamiltonians, which consider also spin-orbit coupling in terms of additional tight-binding parameters. For the experiments (for example the works in Ref. [18, 64, 12, 17] on spin transport and spin relaxation) only specific regions of the band structure are relevant. In these regions, at the vicinity of the K high-symmetry points, the relativistic effects of spin-orbit coupling can be modeled by a spectrum of effective Hamiltonians. In this work we have derived such effective Hamiltonians for all the considered structures from the multi-orbital Hamiltonian. The effective Hamiltonians are given in the reduced basis of the antisymmetric orbitals with respect to the graphene sheets and involve the intra-layer, intrinsic and extrinsic, spin-orbit effects. The corresponding parameters in the effective Hamiltonians have been expressed by the tight-binding parameters of the multi-orbital tight-binding Hamiltonian. We have presented the realistic values for the spin-orbit coupling parameters obtained by fitting the energy spectra obtained by first-principles calculations. The spin-orbit coupling effects in the first-principles band structure of graphene, few layer graphenes, and graphite are well reproduced be the energy dispersion of the effective Hamiltonians.

The derived effective Hamiltonians represent a simple model for graphene and graphene structures, which can be used for investigating spin-dependent phenomena such as spin injection, spin relaxation, and spin transport. Further, our derived model of the effective hopping can be used to study spin effects also for finite single or multi-layer graphene and/or in structures like nanoribbons or graphene flakes. The spin polarization seems to be strong by localized along the edges of graphene nanoribbons due to Bychkov Rashba effect as shown in the work [65]. Our work gives realistic values for the parameters used in such model calculations.

Our main achievements have been the quantitative understanding of the spin

orbit coupling effects on the electronic band structure, the symmetries of these band structure effects. We have uncovered the long forgotten prediction of Slonczewski that one needs $d$ (and some higher, which are however less important, as the first principles calculations show) orbitals. In modern investigations workers have mainly focused on $s$ and $p$ orbitals, obtaining erroneous results, greatly underestimating (by more than an order of magnitude) the actual values of the spin-orbit coupling. On the other hand, we have also manifested that some other modern predictions, predicting an order of magnitude larger spin-orbit couplings in bilayer and trilayer structures, are unfounded. We have demonstrated, in a unique combination of tight-binding modeling, independent first-principles calculations, and group symmetry analyses, that all the major spin-orbit coupling effects indeed come from the intra-layer single sheet graphene. The interlayer coupling is purely orbital, contributing to spin-orbit phenomena indirectly, by coupling already spin split orbitals. The number of $24\,\mu$eV which is the spin-orbit gap in single layer graphene, appears in all the multilayer structures.

In addition, our understanding of spin-orbit coupling in graphene structures in applied transverse electric field leads to the conclusion that realistic fields are insufficient in producing spin-orbit splittings beyond tens of micro eVs. If an experiment sees a larger value (say, meV), it must come not from the electric field (Stark effect), but from direct $sp^3$ hybridization, pulling up the in-plane $p$ orbitals into the $\pi$ band. Such a hybridization is capable of giving locally up to perhaps 10 meV of spin-orbit splitting, about three orders of magnitude higher than the Bychkov-Rashba electric field effect. We have given the Bychkov-Rashba spin-orbit coupling magnitude as a function of the electric field.

Finally, our calculations are also putting bounds on mode simplified symmetry argument derived Hamiltonians, which are in general valid very close to high symmetry points. For example, for graphene itself such a Hamiltonian at the K points is adequate within 5% up to 200 meV. In bilayer systems the simple Hamiltonians are more complicated, involving up to 10 parameters, and the assessment of them is difficult, and it is also questionable if such models are then useful. It seems, but this is still work in progress, that the electronic band structure with spin-orbit coupling of a graphene bilayer can be well described by the intra-layer couplings faithfully.

As an outlook to our work, we have laid foundations for future realistic investigations of the tight-binding electronic structure of graphene with spin-orbit coupling. We can envision several extensions of our efforts. One would be looking and confined systems, such as the aforementioned graphene ribbons and flakes, looking at the edge effects with spin-orbit fields. One can also apply magnetic fields to these systems, modeled by a Peierls phase, and directly obtain the quasi one-dimensional Landau level spectra of the nanoribbons and flakes, to see the effects of the spin-orbit coupling on $g$-factors and cyclotron orbits, for example. Furthermore, graphene ribbons are predicted to be magnetic at the

edges (opposite magnetization at the opposite edges). The spin-orbit coupling gives the mechanism for the magnetic anisotropy. Coupling the ferro-magnetism and spin-orbit coupling in a tight-binding model could be one way of studying these anisotropies. Further possibilities are provided by investigating ad-atoms. For example, it is predicted that a H atom on top of a C atom in graphene hybridizes in $sp^3$, giving large spin-orbit fields in the local (few nm) environment. This could give the large spin relaxation seen in the experiment. Tight-binding investigations of this effect appear within reach. Similarly, one could study defects such as vacancies and ripples using modified spin-orbit tight-binding models similar to ours.

# Bibliography


[1] Riichiro Saito, Gene Dresselhaus, and Mildred S Dresselhaus. *Physical Properties of Carbon Nanotubes*. Imperial College Press, London, 1998.

[2] M. S. Dresselhaus snd G. Dresselhaus. Intercalation compounds of graphite. *Advances In Physics*, 51:1–186, July 1980.

[3] B. Partoens and F. M. Peeters. From graphene to graphite: Electronic structure around the $k$ point. *Phys. Rev. B*, 74(7):075404, Aug 2006.

[4] A. Grüneis, C. Attaccalite, L. Wirtz, H. Shiozawa, R. Saito, T. Pichler, and A. Rubio. Tight-binding description of the quasiparticle dispersion of graphite and few-layer graphene. *Phys. Rev. B*, 78(20):205425, Nov 2008.

[5] L. M. Zhang, Z. Q. Li, D. N. Basov, M. M. Fogler, Z. Hao, and M. C. Martin. Determination of the electronic structure of bilayer graphene from infrared spectroscopy. *Phys. Rev. B*, 78(23):235408, Dec 2008.

[6] Fan Zhang, Bhagawan Sahu, Hongki Min, and A. H. MacDonald. Band structure of abc -stacked graphene trilayers. *Phys. Rev. B*, 82(3):035409, Jul 2010.

[7] Hongki Min, Bhagawan Sahu, Sanjay K. Banerjee, and A. H. MacDonald. Ab initio theory of gate induced gaps in graphene bilayers. *Phys. Rev. B*, 75(15):155115, Apr 2007.

[8] K. S. Novoselov, A. K. Geim, S. V. Morozov, D. Jiang, M. I. Katsnelson, I. V. Grigorieva, S. V. Dubonos, and A. A. Firsov. Two-dimensional gas of massless dirac fermions in graphene. *Nature*, 438:197–200, 2005.

[9] C. L. Kane and E. J. Mele. Quantum spin hall effect in graphene. *Phys. Rev. Lett.*, 95:226801, 2005.

[10] Megumi Ohishi, Masashi Shiraishi, Ryo Nouchi, Takayuki Nozaki, Teruya Shinjo, and Yoshishige Suzuki. Spin injection into a graphene thin film at room temperature. *Japanese Journal of Applied Physics*, 46(25):L605–L607, 2007.

[11] C. Józsa, M. Popinciuc, N. Tombros, H. T. Jonkman, and B. J. van Wees. Controlling the efficiency of spin injection into graphene by carrier drift. *Phys. Rev. B*, 79(8):081402, Feb 2009.

[12] M. Popinciuc, C. Józsa, P. J. Zomer, N. Tombros, A. Veligura, H. T. Jonkman, and B. J. van Wees. Electronic spin transport in graphene field-effect transistors. *Phys. Rev. B*, 80(21):214427, Dec 2009.

[13] Fasil Kidane Dejene. *Spin Transport in Few Layer Graphene Field Effect Transistors*. PhD thesis, Rijksuniversiteit, July 2010.

[14] Wei Han, K. Pi, W. H. Wang, K. M. McCreary, Yan Li, W. Bao, P. Wei, J. Shi, C. N. Lau, and R. K. Kawakami. Spin transport in graphite and graphene spin valves. volume 7398, page 739819. SPIE, 2009.

[15] Masaya Nishioka and A. M. Goldman. Spin transport through multilayer graphene. *Applied Physics Letters*, 90(25):252505, 2007.

[16] H. Goto, A. Kanda, T. Sato, S. Tanaka, Y. Ootuka, S. Odaka, H. Miyazaki, K. Tsukagoshi, and Y. Aoyagi. Gate control of spin transport in multilayer graphene. *Applied Physics Letters*, 92(21):212110, 2008.

[17] T. Maassen, F. K. Dejene, M. H. D. Guimarães, C. Józsa, and B. J. van Wees. Comparison between charge and spin transport in few-layer graphene. *Phys. Rev. B*, 83(11):115410, Mar 2011.

[18] N. Tombros, C. Jozsa, M. Popinciuc, H. T. Jonkman, and B. J. van Wees. Electronic spin transport and spin precession in single graphene layers at room temperature. *Nature*, 448:571–574, 2007.

[19] Christian Ertler, Sergej Konschuh, Martin Gmitra, and Jaroslav Fabian. Electron spin relaxation in graphene: The role of the substrate. *Phys. Rev. B*, 80(4):041405, Jul 2009.

[20] D. Huertas-Hernando, F. Guinea, and Arne Brataas. Spin-orbit-mediated spin relaxation in graphene. *Phys. Rev. Lett.*, 103(14):146801, Sep 2009.

[21] Y. A. Bychkov and E. I. Rashba. Properties of a 2d electron gas with lifted spectral degeneracy. *JETP Lett.*, 39:78–81, 1984.

[22] J. Fabian, A. Matos-Abiague, C. Ertler, P. Stano, and I. Žutić. Semiconductor spintronics. *Acta Phys. Slov.*, 57:565–907, 2007.

[23] H. Min, J. E. Hill, N. A. Sinitsyn, B. R. Sahu, L. Kleinman, and A. H. MacDonald. Intrinsic and rashba spin-orbit interaction in graphene sheets. *Phys. Rev. B*, 74:165310, 2006.

[24] Y. Yao, F. Ye, X.-L. Qi, S.-C. Zhang, and Z. Fang. Spin-orbit gap of graphene: First-principles calculations. *Phys. Rev. B*, 75:041401, 2007.

[25] J. C. Boettger and S. B. Trickey. First-principles calculation of the spin-orbit splitting in graphene. *Phys. Rev. B*, 75:121402, 2007.

[26] M. Gmitra, S. Konschuh, C. Ertler, C. Ambrosch-Draxl, and J. Fabian. Band-structure topologies of graphene: Spin-orbit coupling effects from first principles. *Phys. Rev. B*, 80(23):235431, Dec 2009.

[27] J. C. Slonczewski. *Band Theory of Graphite*. PhD thesis, Rutgers University of New Jersey, 1955.

[28] J. C. Slonczewski and P. R. Weiss. Band structure of graphite. *Phys. Rev.*, 109(2):272–279, Jan 1958.

[29] J. W. McClure and Y. Yafet. Theory of the g-factor of the current carriers in graphite single crystals. In *Proceedings of the Fifth Conference on Carbon*, volume 1, pages 22–28. Pergamon, New York, 1962.

[30] Emmanuel I. Rashba. Graphene with structure-induced spin-orbit coupling: Spin-polarized states, spin zero modes, and quantum hall effect. *Phys. Rev. B*, 79(16):161409, Apr 2009.

[31] I. Gierz, J. H. Dil, F. Meier, B. Slomski, J. Osterwalder, J. Henk, R. Winkler, C. R. Ast, and K. Kern. Giant anisotropic spin splitting in epitaxial graphene. *arxiv:1004.1573*, April unpublished.

[32] Yu. S. Dedkov, M. Fonin, U. Rüdiger, and C. Laubschat. Rashba effect in the graphene/ni(111) system. *Phys. Rev. Lett.*, 100(10):107602, Mar 2008.

[33] A. Varykhalov, J. Sánchez-Barriga, A. M. Shikin, C. Biswas, E. Vescovo, A. Rybkin, D. Marchenko, and O. Rader. Electronic and magnetic properties of quasifreestanding graphene on ni. *Phys. Rev. Lett.*, 101(15):157601, Oct 2008.

[34] A. H. Castro Neto and F. Guinea. Impurity-induced spin-orbit coupling in graphene. *Phys. Rev. Lett.*, 103(2):026804, Jul 2009.

[35] F. Guinea. Spin-orbit coupling in a graphene bilayer and in graphite. *arxiv:cond-mat/1003.1618*, aug unpublished.

[36] H.-W. Liu, X. C. Xie, and Q.-f. Sun. Giant Intrinsic Spin-Orbit Coupling in Bilayer Graphene. *arxiv:cond-mat/1004.0881*, apr unpublished.

[37] Edward McCann and Mikito Koshino. Spin-orbit coupling and broken spin degeneracy in multilayer graphene. *Phys. Rev. B*, 81(24):241409, Jun 2010.

[38] J. P. Perdew, K. Burke, and M. Ernzerhof. Generalized gradient approximation made simple. *Phys. Rev. Lett.*, 77:3865–3868, 1996.

[39] J.C. Slater and G.F. Koster. Simplifed lcao method for periodic potential problem. *Phys. Rev.*, 94(1498), 1954.

[40] J. J. Sakurai and J. Napolitano. *Modern Quantum Mechanics*. Jim Smith, San Francisco, 2011.

[41] P. Harrison. *Quantum Wells, Wires and Dots. theoretical and computational physics of semiconductor nanostructures.* Springer-Verlag Berlin Heidelberg New York, 2006.

[42] R. J. Elliott. Theory of the effect of spin-orbit coupling on magnetic resonance in some semiconductors. *Phys. Rev.*, 96(2):266–279, Oct 1954.

[43] Ralph van Gelderen and C. Morais Smith. Rashba and intrinsic spin-orbit interactions in biased bilayer graphene. *Phys. Rev. B*, 81(12):125435, Mar 2010.

[44] R.Winkler. *Spin-Orbit Coupling Effects in Two-Dimensional Electron and Hole Systems*. Springer-Verlag Berlin Heidelberg, 2003.

[45] D. Huertas-Hernando, F. Guinea, and A. Brataas. Spin-orbit coupling in curved graphene, fullerenes, nanotubes, and nanotube caps. *Phys. Rev. B*, 74:155426, 2006.

[46] M. I. D'yakonov and V. I. Perel'. Theory of optical spin orientation of electrons and nuclei in semiconductors. In F. Meier and B. P. Zakharchenya, editors, *Optical Orientation, Modern Problems in Condensed Matter Science, Vol. 8*, pages 11–71. North-Holland, Amsterdam, 1984.

[47] J.Fabian, A.Matos-Abiague, C.Ertler, P.Stano, and I.Žutić. *Acta physica slovaca*, volume 57. Slovak Academy of Science, Bratislava, 2007.

[48] F. Freimuth, Y. Mokrousov, D. Wortmann, S. Heinze, and S. Blügel. Maximally localized wannier functions within the flapw formalism. *Phys. Rev. B*, 78(3):035120, Jul 2008.

[49] L. G. Johnson and G. Dresselhaus. Optical properies of graphite. *Phys. Rev. B*, 7(6):2275–2285, Mar 1973.

[50] J.-C. Charlier, J.-P. Michenaud, X. Gonze, and J.-P. Vigneron. Tight-binding model for the electronic properties of simple hexagonal graphite. *Phys. Rev. B*, 44(24):13237–13249, Dec 1991.

[51] J.-C. Charlier, J.-P. Michenaud, and X. Gonze. First-principles study of the electronic properties of simple hexagonal graphite. *Phys. Rev. B*, 46(8):4531–4539, Aug 1992.

[52] Adam H. R. Palser. Interlayer interactions in graphite and carbon nanotubes. *Phys. Chem. Chem. Phys.*, 1(18):4459–4464, July 1999.

[53] Sylvain Latil and Luc Henrard. Charge carriers in few-layer graphene films. *Phys. Rev. Lett.*, 97(3):036803, Jul 2006.

[54] Johan Nilsson, A. H. Castro Neto, F. Guinea, and N. M. R. Peres. Electronic properties of bilayer and multilayer graphene. *Phys. Rev. B*, 78(4):045405, Jul 2008.

[55] Mikito Koshino and Edward McCann. Gate-induced interlayer asymmetry in aba-stacked trilayer graphene. *Phys. Rev. B*, 79(12):125443, Mar 2009.

[56] J. B. OOstinga, H. B. Heersche, X. Liu, A. F. Morpurgo, and L. M. K. Vandersypen. *Nature Mat.*, 7:151–157, 2008.

[57] Yuanbo Zhang, Tsung-Ta Tang, Caglar Girit, Zhao Hao, Michael C. Martin, Alex Zettl, Michael F. Crommie, Y. Ron Shen, and Feng Wang. Direct observation of a widely tunable bandgap in bilayer graphene. *Nature*, 459:820–823, June 2009.

[58] Igor Zutic, Jaroslav Fabian, and S. Das Sarma. Spintronics: fundamentals and applications. *Rev. Mod. Phys.*, 76:323, Apr 2004.

[59] Ralph van Gelderen and C. Morais Smith. Rashba and intrinsic spin-orbit interactions in biased bilayer graphene. *Phys. Rev. B*, 81(12):125435, Mar 2010.

[60] Taisuke Ohta, Aaron Bostwick, Thomas Seyller, Karsten Horn, and Eli Rotenberg. Controlling the Electronic Structure of Bilayer Graphene. *Science*, 313(5789):951–954, 2006.

[61] Eduardo V. Castro, K. S. Novoselov, S. V. Morozov, N. M. R. Peres, J. M. B. Lopes dos Santos, Johan Nilsson, F. Guinea, A. K. Geim, and A. H. Castro Neto. Biased bilayer graphene: Semiconductor with a gap tunable by the electric field effect. *Phys. Rev. Lett.*, 99(21):216802, Nov 2007.

[62] Sergej Konschuh, Martin Gmitra, and Jaroslav Fabian. Tight-binding theory of the spin-orbit coupling in graphene. *Phys. Rev. B*, 82(24):245412, Dec 2010.

[63] G. Dresselhaus and M. S. Dresselhaus. Spin-orbit interaction in graphite. *Phys. Rev.*, 140(1A):A401–A412, Oct 1965.

[64] N. Tombros, S. Tanabe, A. Veligura, C. Jozsa, M. Popinciuc, H. T. Jonkman, and B. J. van Wees. Anisotropic spin relaxation in graphene. *Phys. Rev. Lett.*, 101(4):046601, Jul 2008.

[65] Mahdi Zarea and Nancy Sandler. Rashba spin-orbit interaction in graphene and zigzag nanoribbons. *Phys. Rev. B*, 79(16):165442, Apr 2009.

# Acknowledgment

I would like take this opportunity my gratitude first and foremost to Prof. Jaroslav Fabian for successfully guiding me through graduate studies and excellent advise and great support through the ups and downs during my work at the University of Regensburg. I would also to thank Prof. Fabian for opening me a possibility to be a member of a harmonious group of very talented physicists and making me really enjoy the time spending in Regensburg.

My gratitude also goes to the group member Dr. Martin, Gmitra, Dr. Dennis Kochan, Dr. Alex Matos-Abiague, Benedikt Scharf, Martin Raith, and Sebastian Putz, and also former member Dr. Christian Ertler for the great help and assistance in the years of preparing this thesis.

Especially I would like thank Dr. Martin Gmitra for unparalleled team work and giving me his generous assistance. I would like to emphasize that without his excellent numerical studies this thesis would not be possible.

My spacial thanks go also to my office roommates Benedikt Scharf, Martin Raith, and Sebastian Putz helping me by the workday life of graduate studies: in discussions and of physical and technical problems, and conscientious corrections of this thesis.

Finally, I wish to thank my family and my beloved girlfriend for the unconditional love and also her family for unwavering support that they have offered me during my time in Regensburg. They have always stood by my side in the hard times during my studies especially while writing the thesis.

Sergej Konschuh
The University of Regensburg
July 2011

# Curriculum vitæ

| | |
|---|---|
| **Personal Data** | Sergej Konschuh |
| | born 06. 09. 1980 in Karaganda / Kasachstan |
| | citizenship German |

**Education**

| | |
|---|---|
| 1986–1993 | comprehensive school nr. 52 Karaganda |
| 1993–1994 | technical elite school Karaganda |
| 1994–1995 | Insel-Hauptschule Pforzheim |
| 1995–1996 | Konrad Adenauer Realschule Pforzheim |
| 1996–2001 | Hebel-Gymnasium Pforzheim |
| June, 2001 | graduation: Abitur |

**Military Duty**

| | |
|---|---|
| 2001–2002 | Air-force base in Ummendorf, Germany |

**Study**

| | |
|---|---|
| 2002–2007 | physics at the technical University of Karlsruhe (KIT) |
| July, 2007 | graduation: Diploma in theoretical solid state physics. |
| 2007–2011 | conferral of a doctorate in theoretical solid state physic |
| | at the University of Regensburg |